THE PHOTOCHEMISTRY OF DINITROGEN PENTOXIDE

Peter Steele Connell
(Ph.D. thesis)

May 1979

Prepared for the U. S. Department of Energy
under Contract W-7405-ENG-48

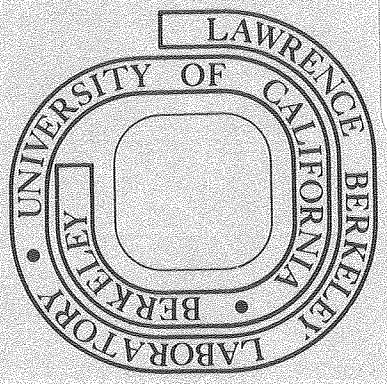

DISCLAIMER

LBL-9034

THE PHOTOCHEMISTRY OF DINITROGEN PENTOXIDE

by

Peter Steele Connell

Materials and Molecular Research Division
Lawrence Berkeley Laboratory and Department of Chemistry
University of California, Berkeley, California 94720

THE PHOTOCHEMISTRY OF DINITROGEN PENTOXIDE

Peter Steele Connell

Table of Contents

ABSTRACT vii

I. INTRODUCTION 1

A. THERMAL DECOMPOSITION 2

B. PHOTOCHEMISTRY OF N_2O_5 6

C. THE STRUCTURE AND THERMOCHEMISTRY OF N_2O_5 7

II. EXPERIMENTAL METHODS AND APPARATUS 9

A. METHODS 9

1. Thermal Decomposition 9

2. Photochemistry 11

B. APPARATUS 21

1. Reaction Cell and Temperature Control 21

2. Optical System 22

3. Detector 24

4. Signal Processing 25

5. Photolytic Source 32

C. GASES AND FLOW SYSTEM 35

III. EXPERIMENTAL PROCEDURES AND DATA 38

A. INFRARED ABSORPTION CROSS SECTIONS 38

B. THERMAL DECOMPOSITION EXPERIMENTS 46

C. CLOSED CELL PHOTOLYSES 61

D. CONSTANT INTENSITY PHOTOLYSIS OF FLOWING SYSTEMS 62

E. MODULATION EXPERIMENTS 65

F. ACTINOMETRY 68

IV. RESULTS AND DISCUSSION 73

A. THERMAL DECOMPOSITION 73

B. PHOTOCHEMISTRY 105

1. UV Spectrum of N_2O_5 105

2. Closed Cell Photolyses 106

3. Constant Illumination in Flowing Systems 116

4. Intermittent Photolysis in Flowing Systems 116

5. Summary of Photolysis Results 121

V. STRATOSPHERIC IMPLICATIONS 124

A. EXTRAPOLATION OF THE THERMAL DISSOCIATION RATE CONSTANT 124

B. NIGHTTIME STRATOSPHERE MODEL. 129

C. N_2O_5 PHOTOCHEMISTRY IN THE STRATOSPHERE 136

APPENDIX A: MULTIPARAMETER NON-LINEAR LEAST SQUARES FITTING PROGRAM 141

APPENDIX B: COMPLETE REACTION SET FOR PHOTOCHEMICAL MODELING 149

ACKNOWLEDGMENTS 150

BIBLIOGRAPHY 151

THE PHOTOCHEMISTRY OF DINITROGEN PENTOXIDE

Peter Steele Connell

Materials and Molecular Research Division,
Lawrence Berkeley Laboratory and Department of Chemistry,
University of California, Berkeley, California 94720

ABSTRACT

This study examined the gas phase photochemistry and thermal decomposition kinetics of dinitrogen pentoxide, N_2O_5. The products of photodecomposition and the quantum yield as a function of pressure have been determined at a wavelength of 254 nm. The rate of thermal decomposition of N_2O_5 in the presence of excess NO has been observed between 4×10^{14} to 2.8×10^{19} molecules cm^{-3} and 262 to 307 K.

The investigation was conducted by monitoring the infrared absorptions of N_2O_5, NO_2 and HNO_3. Absorption cross sections for these species were experimentally determined. The techniques used included closed cell decay profiles, with and without photolyzing light, constant illumination of flow systems and modulation of species in a flow system with intermittent photolytic illumination.

The thermal decomposition of N_2O_5 in the presence of NO proceeds by the mechanism

$$N_2O_5 \xrightarrow{A(M)} NO_2 + NO_3$$
$$\underline{NO + NO_3 \xrightarrow{fast} 2NO_2}$$
$$\text{net:}\quad N_2O_5 + NO \longrightarrow 3NO_2$$

for which the rate is controlled by the rate of the first step, the unimolecular decomposition of N_2O_5. At low pressure the reaction becomes second-order with respect to the total pressure. Measurements made in nitrogen, for which $[N_2] < 2 \times 10^{16}$ molecule cm^{-3}, give an expression for the second-order low pressure limit

$$268 \text{ to } 307\,K \quad k_o' = 8.05 \times 10^{-6} \exp(-9630 \pm 200/T) \text{ cm}^3\text{molec}^{-1}\text{sec}^{-1}.$$

At sufficiently high pressure, the reaction is strictly first-order. The experimental indication obtained for the high pressure limit of the rate constant is

$$262 \text{ to } 272 \text{ K} \quad k_\infty = 1.78 \times 10^{17} \exp(-12540 \pm 200/T) \text{ sec}^{-1}.$$

The behavior of the rate constant for thermal decomposition in the fall-off region between the high and low pressure limits is adequately described over the temperature range 262 to 307 K by the expression

$$k = \frac{-(k_o'[M]+k_\infty) + ((k_o'[M]+k_\infty)^2 + 22\,k_\infty k_o'[M])^{1/2}}{11}.$$

These expressions can be combined with the equilibrium constant, measured by Graham,[27] to give the third and second-order limits of the reverse reaction

$$NO_2 + NO_3 \xrightarrow{B(M)} N_2O_5.$$

The values are

$$k_r(\text{low p}) = 9.58\times10^{-33} \exp(+1550/T) \text{ cm}^6\text{molec}^{-2}\text{sec}^{-1}$$

and

$$k_r(\text{high p}) = 2.12\times10^{-10} \exp(-1360/T) \text{ cm}^3\text{molec}^{-1}\text{sec}^{-1}.$$

The low pressure limit obtained is in good agreement with the earlier work of Johnston and Perrine[7] and Johnston.[8] The activation energy in the high pressure limit is larger than the estimate of Mills and Johnston[6] of 10570 K and implies a small positive activation energy for the recombination reaction of NO_2 AND NO_3 at high pressure. The predicted high pressure limit of the dissociation rate constant at 300 K is about one half the value reported by Mills and Johnston.

Experiments in which N_2O_5 was photolyzed by 254 nm radiation in the presence of nitrogen or oxygen buffer showed the primary photolytic step to be

$$N_2O_5 + h\nu \longrightarrow 2NO_2 + O.$$

The quantum yield is a function of both N_2O_5 and buffer gas pressure and of the rates of secondary reactions. The suggested mechanism in the absence of secondary reactions is

$$N_2O_5 + h\nu \longrightarrow N_2O_5^*$$

$$N_2O_5^* \longrightarrow 2NO_2 + O$$

$$N_2O_5^* + N_2O_5 \longrightarrow 2N_2O_5$$

$$\longrightarrow 2NO_2 + O$$

$$N_2O_5^* + M \longrightarrow N_2O_5 + M.$$

The ratio of self-quenching to collisionally activated decomposition is 2.2. If the sum of these two processes is considered collisional, the collision-free lifetime of the excited $N_2O_5^*$ is 6×10^{-6} sec. Quenching by nitrogen and oxygen is about 10^4 less efficient than quenching by N_2O_5.

From experimental upper limits to N_2O_5 concentrations in the stratosphere and standard air density values, the quantum yield for N_2O_5 photolysis in the stratosphere is calculated to be greater than 0.9 above 20 km and essentially unity throughout the region of maximum N_2O_5 concentration.

I. INTRODUCTION

Recent interest in nitrogen oxides as tropospheric[1] and stratospheric[2] pollutants has created a need for laboratory measurements of kinetic and photolytic parameters associated with the reactions of these species (NO, NO_2, NO_3, N_2O_5, ...). The thermal decomposition of dinitrogen pentoxide

$$N_2O_5 \xrightarrow{A(M)} NO_2 + NO_3 \qquad (1)$$

has historically been studied as an example of a true unimolecular reaction with which to test various kinetic theories.[3] These measured decomposition rate constants can also be used in an atmospheric model to predict distributions of N_2O_5 and NO_3 in the stratosphere. The atmospheric role of N_2O_5 is to provide a temporary sink for the more active forms of NO_x, which participate in controlling ozone concentrations.

In addition to thermal decomposition, N_2O_5 exhibits a continuous absorption in the ultraviolet spectral region, which begins at around 380 nm and increases smoothly with decreasing wavelength, showing no maximum above 210 nm. The photochemistry of this absorption may contribute to limiting the lifetime of N_2O_5 in the stratosphere and to possible reduction of ozone by the mechanism

$$\begin{aligned} NO_2 + O_3 &\longrightarrow NO_3 + O_2 \\ NO_2 + NO_3 &\xrightarrow{M} N_2O_5 \\ N_2O_5 + h\nu &\longrightarrow NO + NO_2 + O_2 \\ NO + O_3 &\longrightarrow NO_2 + O_2 \\ \hline \text{net: } 2O_3 &\longrightarrow 3O_2 \end{aligned} \qquad (2)$$

A. THERMAL DECOMPOSITION

The technique used to study this process originated in the observation of a fast reaction between nitric oxide and dinitrogen pentoxide to yield nitrogen dioxide.[4] Smith and Daniels[5] proposed the mechanism.

$$\begin{aligned} N_2O_5 &\underset{\text{fast}}{\overset{\text{slow}}{\rightleftharpoons}} NO_2 + NO_3 \\ NO + NO_3 &\xrightarrow{\text{fast}} NO_2 + NO_2, \end{aligned} \qquad (3)$$

in which the NO acts as a fast scavenger for the NO_3 produced in the decomposition of N_2O_5, preventing its recombination with NO_2. Thus, at least initially, the observed rate of N_2O_5 disappearance in the presence of NO is that of the slow unimolecular decomposition of N_2O_5. Mills and Johnston[6] employed this scheme, monitoring the appearance of the product, NO_2, optically to study the reaction over a range of pressures from 0.011 to 933 kPa at 300 K, and at a few pressures at 273, 277 and 313 K.

Their work was refined at low pressures by Johnston and Perrine,[7] by Johnston[8] and Wilson and Johnston,[9] again by optical detection of NO_2. Johnston and Perrine extended the study of the rate of decomposition down to a total pressure of 6.7 Pa at 300, 323 and 344 K, obtaining a low pressure activation energy. Further work by Wilson and Johnston at 324 K in the presence of a variety of buffer gases clarified the relative activational efficiencies of N_2O_5, NO, Ar, N_2, CO_2 and SF_6. Hisatsune, Crawford and Ogg[10] followed the decomposition at 7.6 and 53.3 kPa total pressure in nitrogen. Using a fast scanning infra-red spectrometer, they were able to monitor both the disappearance of N_2O_5 and the appearance of NO_2 at a few temperatures between 293 and 303 K.

Recently Viggiano, et al.[11] have applied their technique of chemical ionization mass spectrometry to observe the decomposition of N_2O_5 in the presence of NO and N_2 in a flowing system. They have extended the temperature range of observations from 268 to 379 K, for pressures between 1.87 and 46.7 kPa. These are the first data for which experimental conditions approach those characteristic of the stratosphere.

Representative data of the various workers are presented in Fig. 1 as log k_{uni} plotted against log [M], the total effective number density. If necessary for the sake of comparison, data have been adjusted to common temperatures using reported activation energies. The total effective number density is calculated as the effective N_2 concentration, using the measured relative efficiencies of Johnston.[8] The associated activation energies and preexponential factors are listed in Table 1, calculated from assumption of the Arrhenius form

$$k_{uni} = A \exp(-E_a/T), \; E_a \text{ in K.} \qquad (4)$$

While there is general agreement among the results with respect to activation energies, evident disagreement exists between Viggiano, et al. and the earlier work over the magnitude of k_{uni} at 300 K. This difference of a factor of two or three persists in the extrapolation to the lower temperatures of the stratosphere. This uncertainty is reflected in widely differing predicted behavior of N_2O_5 and NO_3 atmospheric distributions.[12]

The goal of this portion of the present work is to attempt to resolve this difference and to provide decomposition rate constants measured at pressures and temperatures more closely matching actual stratospheric conditions.

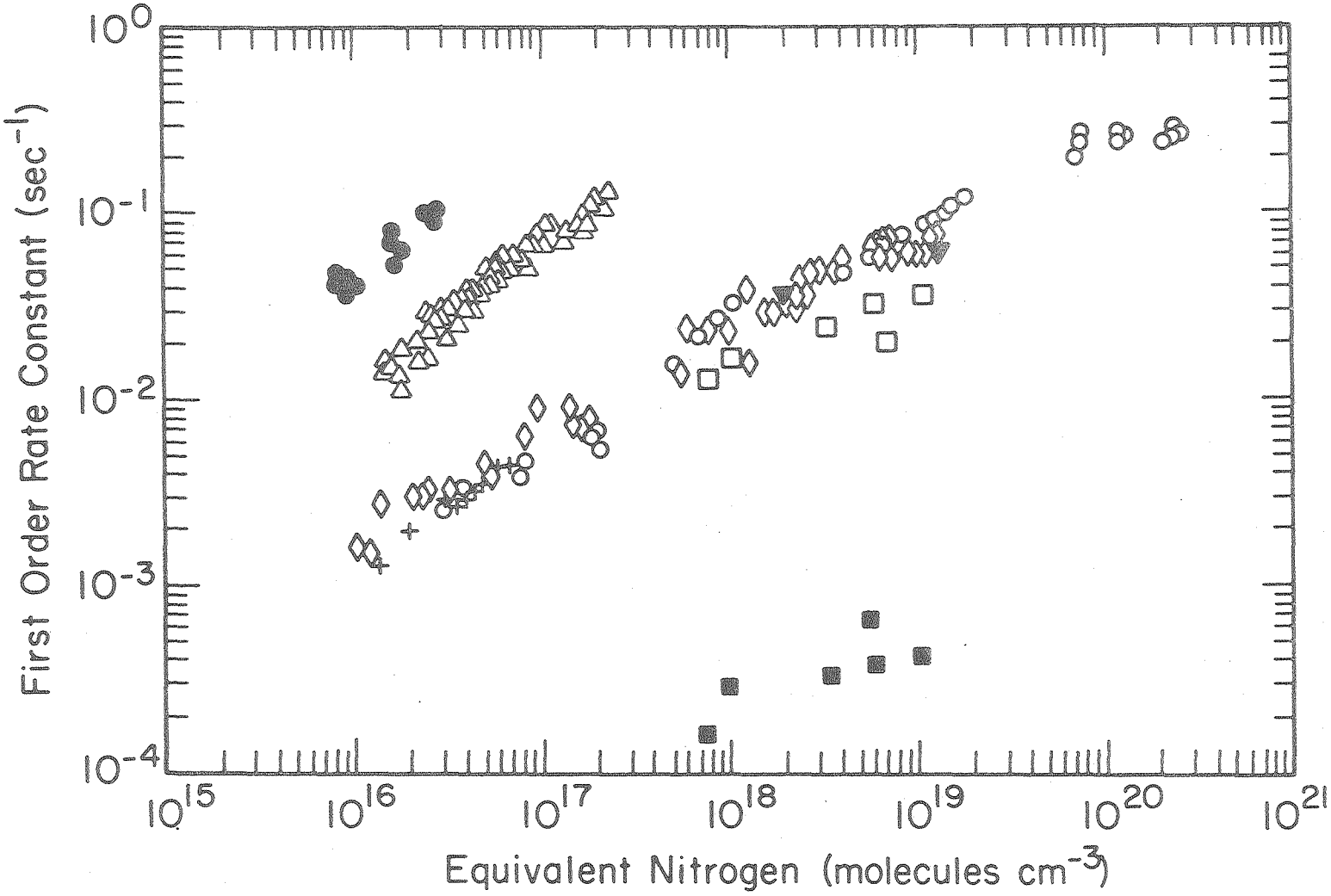

XBL 794-9333

Figure 1. Unimolecular decomposition rate constants at various temperatures. (● Johnston and Perrine, pure reactants, 344 K; Δ Johnston, N_2, 324 K; + Johnston, N_2, 300 K; ◇ Mills and Johnston, pure reactants, 300 K; ○ Mills and Johnston, N_2, 300 K; ▼ Hisatsune, et al. N_2, 300 K; □ Viggiano, et al, N_2, 300 K, and ■, 268 K).

TABLE ONE

[M] molecules cm^{-3}	T K	A	E_a K	Reference
$0.018\text{-}3.5 \times 10^{17}$	300-344	4.9×10^{-5}	9698±300	7[a]
$0.07\text{-}2.5 \times 10^{20}$	273-300	5.8×10^{14}	10570±1000	6[b]
$0.01\text{-}3.5 \times 10^{16}$	300-323	3.7×10^{-5}	9191	13[a]
Estimate of high pressure limit	300	1.77×10^{17}	12290	13[b]
2×10^{18}	293-303	1.26×10^{13}	10070	10[c]
1.4×10^{19}	293-3-3	1.26×10^{14}	10570	10[c]
$0.05\text{-}1.2 \times 10^{19}$	268-370		10520	11
Estimate of low pressure limit	268-370	3.51×10^{-6}	9570	11[a]
Estimate of high pressure limit	268-370	3.17×10^{14}	11000	11[b]

[a] 2nd order limit. A in units of cm^3 $molecule^{-1}$ sec^{-1}.

[b] 1st order limit. A in units of sec^{-1}.

[c] 2nd order intermediate pressure value. A in units of cm^3 $molecule^{-1}$ sec^{-1}.

B. PHOTOCHEMISTRY OF N_2O_5

The photochemistry of N_2O_5 in the ultraviolet spectral region has been studied by Holmes and Daniels[14] and Murphy.[15] Both experiments involved timed photolysis in a sealed bulb. Following the illumination period, progress of the photolysis was monitored by pressure change and by visible absorption of the nitrogen dioxide produced, respectively. Assuming that the overall photochemical process can be represented as

$$N_2O_5 + h\nu \longrightarrow 2NO_2 + \frac{1}{2}O_2, \qquad (5)$$

Holmes and Daniels measured a quantum yield of 0.6 at both 273 and 283 K under illumination of wavelengths 265 and 280 nm. In these experiments N_2O_5 was present at its respective equilibrium vapor pressure (6.87 kPa at 273 K).

Murphy obtained pressure dependent quantum yields varying from 0.28 to 0.68 at 273 K and 280 nm. The partial pressure of N_2O_5 was varied from 1.87 to 6.67 kPa in the presence of up to 80 kPa of buffer gas. In agreement with the earlier suggestion of Holmes and Daniels, Murphy proposes a mechanism involving the production of an oxygen atom as a primary photodecomposition product,

$$\begin{aligned} N_2O_5 + h\nu\ (280\ nm) &\longrightarrow N_2O_5^* \\ N_2O_5^* &\longrightarrow 2NO_2 + O. \end{aligned} \qquad (6)$$

The second portion of the present work will attempt to clarify the photochemistry of N_2O_5. Direct evidence for the primary products of photolysis and an understanding of the source of apparently pressure dependent quantum yields are the experimental goals. These results can

then be used to study the stratospheric importance of photodecomposition.

C. THE STRUCTURE AND THERMOCHEMISTRY OF N_2O_5

The well-known thermal dissociation of N_2O_5 into NO_2 and NO_3 in addition to the similarity of its IR spectrum to that of N_2O_4, which consists of two fairly unperturbed NO_2 fragments, indicate that N_2O_5 should have a C_{2v} structure about a central N-O-N bond. Early electron diffraction studies[16] suggested a central bond angle of 180°, but the large measured dipole of the molecule[17] is irreconcilable with the linear symmetric structure. A CNDO/2 theoretical study[18] calculated an equilibrium bond angle of 148° which can be reconciled with the dipole moment. More recent electron diffraction work[19] shows that N_2O_5 exists in the gas phase with a nonplanar C_{2v} symmetry. The central angle is 95 ± 3°, the end group O-N-O angle is 134 ± 9° and the central and terminal N-O bonds distances are 1.46 and 1.21 Å, resptectively.

Hisatsune reports a gas phase entropy for N_2O_5[20] which is consistent with a low barrier to internal rotation of the end nitro groups. His analysis of the IR spectrum[21] supports this conclusion and also indicates a very low frequency for the central bond deformation. Assigning this deformation with a frequency of about 85 cm^{-1}, to match observed overtone spacings, he calculates about a 1.9 kcal/mole barrier to internal rotation, to match the entropy.

The heats of formation of N_2O_5 and its possible photodecomposition products can be used to calculate wavelength cutoffs for the possible channels. The values used were

	ΔH^{o}_{298}	
N_2O_5	3.1 kcal/mole	
NO_2	8.1	
NO_3	17.6	(7)
NO	21.6	
O	59.4 .	

The calculated maximum wavelengths for photolysis are

Products	Cutoff	
$NO_2 + NO_3$	1300 nm	
$NO_2 + NO_2 + O$	401 nm	(8)
$NO + NO_2 + O_2$	1125 nm .	

The ultraviolet absorption spectrum commences around 380 nm so that all three possibilities are energetically allowed.

II. EXPERIMENTAL METHODS AND APPARATUS

A. METHODS

Most of the experimental work to be described is based on the monitoring in situ of the 1250 cm^{-1} IR absorption of N_2O_5. The chief advantages of this choice are first that the band is only slightly overlapped by the associated nitric acid absorption (an ever present contaminant), as opposed to the 1750 cm^{-1} band observed by Hisatsune, et al.[10] Secondly it exhibits Beer's Law behavior over a wide range of total pressures, unlike, for example, the 1600 cm^{-1} band of NO_2.

1. Thermal Decomposition

For the study of the thermal decomposition of N_2O_5 the standard mechanism was employed, involving the addition of excess NO to the mixture of N_2O_5 and the buffer gas, N_2. The complete mechanism involves the four elementary reactions,

$$\begin{aligned} N_2O_5 &\xrightarrow{A(M)} NO_2 + NO_3 \\ NO_2 + NO_3 &\xrightarrow{B(M)} N_2O_5 \\ NO_2 + NO_3 &\xrightarrow{e} NO + NO_2 + O_2 \\ NO + NO_3 &\xrightarrow{f} NO_2 + NO_2 \ . \end{aligned} \tag{9}$$

While the NO concentration is larger than that of NO_2, reaction f, the scavenging of NO_3 by NO, is much faster than the recombination reaction, B. In addition, the steady state concentration of NO_3 is depressed so that reaction e, the rate determining step in the medium to high pressure decomposition of pure N_2O_5[22] is also negligible. The complete rate

expression for N_2O_5,

$$-\frac{d[N_2O_5]}{dt} = A\,[N_2O_5]\left(\frac{e[NO_2] + f[NO]}{(B+e)[NO_2] + f[NO]}\right), \qquad (10)$$

reduces, for $[NO_2] < f[NO]/(B[M] + e)$, to the rate of reaction A.

The choice of monitoring the first order decay of the absorbance of N_2O_5 rather than the appearance of NO_2, as in earlier studies, offers several advantages. The necessity of knowing either the absolute initial N_2O_5 concentration or the NO_2 absorbance after the reaction has proceeded to completion is eliminated. Measurements can be extended to the stratospheric pressure and temperature regime for which reaction half times become large. Additionally, a convenient solution to the problem of heterogeneous contributions to the reaction rate is made possible.

Two recongnized heterogeneous reactions must be considered. The rate constants of

$$N_2O_5 + H_2O \longrightarrow 2HNO_3 \qquad (11)$$

and

$$HNO_3 + NO \longrightarrow NO_2 + HNO_2 \qquad (12)$$

are negligibly small in the gas phase[23,24] but are known to occur via heterogeneous pathways.[25] If the appearance of NO_2 is used as a measure of the extent of reaction, the complication of reaction 11 will either cause positive curvature in the semilog plot of N_2O_5 concentration vs. time, if the initial N_2O_5 concentration is measured independently, or result in an empirical rate constant which is the sum of the homogeneous and heterogeneous pathways. The effect of reaction 12 would depend on

the stoichiometry of the process and on the concentrations of NO and HNO_3, but it would in general serve to increase the apparent decomposition rate constant.

When the decomposition reaction is monitored by the direct observation of the loss of the reactant, N_2O_5, processes which produce NO_2 without loss of N_2O_5 are not observed. The heterogeneous loss of N_2O_5 to form nitric acid can be minimized through drying of the gases and conditioning of the cell. The remaining heterogeneous loss rate can be measured by observing the decay of N_2O_5 in the absence of NO. The homogeneous rate constant for thermal decomposition of pure N_2O_5 is small[26] and can be corrected for. The value obtained is then subtracted from the measured N_2O_5-NO rate constant to find the homogeneous component.

2. Photochemistry

The study of the photochemistry of dinitrogen pentoxide was conducted using several static and dynamic methods. These include reactant loss profiles in a closed cell under conditions of constant illumination and monitoring of the approach to a photochemical steady state in a flowing system. A molecular modulation study of the infrared absorptions of N_2O_5 and NO_2 in a flowing system subjected to intermittent illumination probed their respective roles in the photochemical mechanism.

The study of reactions in chemical systems involving NO_x compounds is usually obstructed by fast secondary reactions which obscure the kinetics of interest. The various experiments performed were intended to illuminate selected aspects of the photochemistry by minimizing areas of interference and enhancing the desired reactions. Consider one

(of the more simple) possibilities for a reaction set:

$$
\begin{aligned}
&N_2O_5 + h\nu \xrightarrow{j_1} NO_2 + NO_3 \\
&N_2O_5 \xrightarrow{A[M]} NO_2 + NO_3 \\
&NO_2 + NO_3 \xrightarrow{B[M]} N_2O_5 \\
&NO_2 + h\nu \xrightarrow{j_2} NO + O \\
&NO + NO_3 \xrightarrow{f} NO_2 + NO_2 \\
&NO_2 + O \xrightarrow{m} NO + O_2 \\
&NO_3 + O \xrightarrow{n} NO_2 + O_2 \\
&NO_2 + NO_3 \xrightarrow{e} NO + NO_2 + O_2 .
\end{aligned}
\qquad (13)
$$

The reaction of N_2O_5 with oxygen atoms is very slow[15,27,28] and can be ignored. The photolysis of NO_2 is unavoidable since it absorbs light with decomposition over the same region of the ultraviolet spectrum as N_2O_5. However, at a sufficiently low temperature and pressure, the thermal decomposition and recombination reactions can be made slower than photolysis. The observed rate of N_2O_5 decay will then be primarily the rate of photodecomposition. Knowledge of the incident light intensity and absorption cross section allows calculation of the primary quantum yield,

$$\Phi = j_1/\sigma I_{h\nu}. \qquad (14)$$

A series of experiments at total pressures around 0.13 kPa at 252 K in a closed cell under constant illumination gave this information. Because the secondary reactions have been suppressed, the quantum yield of the reactant decay is independent of the photolytic products.

The mechanism outlined above is the first of three possibilities, based on three sets of primary photodecomposition products. The second scheme follows production of atomic oxygen, $O(^3P)$:

$$\begin{aligned}
&N_2O_5 + h\nu \xrightarrow{j_1} NO_2 + NO_2 + O \\
&N_2O_5 + \xrightarrow{A[M]} NO_2 + NO_3 \\
&NO_2 + NO_3 \xrightarrow{B[M]} N_2O_5 \\
&NO_2 + O \xrightarrow{m} NO + O_2 \\
&NO + NO_3 \xrightarrow{f} NO_2 + NO_2 \\
&NO_2 + h\nu \xrightarrow{j_2} NO + O \\
&NO_3 + O \xrightarrow{n} NO_2 + O_2 \\
&NO_2 + NO_3 \xrightarrow{e} NO + NO_2 + O_2.
\end{aligned} \tag{15}$$

The third possible mechanism is:

$$\begin{aligned}
&N_2O_5 + \xrightarrow{j_1} NO + NO_2 + O_2 \\
&N_2O_5 \xrightarrow{A[M]} NO_2 + NO_3 \\
&NO_2 + NO_3 \xrightarrow{B[M]} N_2O_5 \\
&NO_2 + h\nu \xrightarrow{j_2} NO + O \\
&NO_2 + O \xrightarrow{m} NO + O_2 \\
&NO_3 + O \xrightarrow{n} NO_2 + O_2 \\
&NO_2 + NO_3 \xrightarrow{e} NO + NO_2 + O_2.
\end{aligned} \tag{16}$$

These two cases produce the same net reaction,

$$2N_2O_5 + h\nu \longrightarrow 4NO_2 + O_2, \tag{17}$$

for which the overall quantum yield is twice that of the primary step. The first mechanism mentioned results in no net decomposition of N_2O_5,

an apparent quantum yield of zero.

In order to differentiate between the mechanism based on the production of oxygen atoms and the mechanism based on the production of NO in the photolysis, the reaction of O with NO_2 to yield NO must be averted. This is accomplished through use of oxygen rather than nitrogen as the buffer gas. Adding the reaction

$$O + O_2 + M \xrightarrow{P} O_3 + M \qquad (18)$$

to mechanism (15) reduces its initial quantum yield from two in the case of nitrogen buffer gas to one when oxygen is used. Mechanism (16) will not be affected by the use of oxygen. After a period of illumination, considering mechanism (15) in oxygen, ozone will build up and the reaction,

$$NO_2 + O_3 \xrightarrow{h} NO_3 + O_2, \qquad (19)$$

will become important. This reoxidation of NO_2 to NO_3 will eventually suppress the empiric quantum yield below one, in the limit reducing it to zero.

These effects will be observable only if the thermal decomposition rate is competitive with the photolytic rate, so that the intermediate, NO, can find an NO_3 with which to react. Static cell runs in N_2 and O_2 at 101 kPa (1 atm) and 295 K were performed in a manner similar to the 252 K experiments described above, in order to test the proposed differentiation in the use of the two buffer gases. Additional experiments at an intermediate temperature (273 K) with a closed cell and at 267 K with reactant in a carrier gas flowing through the cell under

constant illumination were accumulated. Interpretation of these results requires consideration of several secondary reactions and rate constants. These experiments are meant to provide an additional validation of the hypothesized mechanism.

The final set of photolysis experiments involve a system of regulated flow of N_2O_5 in a carrier gas through the cell under intermittent illumination. The chemical system's response to the low frequency square wave (on/off) illumination by the germicidal photolysis lamps is monitored in the frequency domain. The averaged result of many cycles is equivalent to the signal-averaged transient response of the system to perturbations from a steady state condition maintained by flow and photolysis. The observable quantities obtained from electronic processing of the signal are the magnitudes of the in-phase and quadrature components of the first harmonic of the modulated absorption. These are expressed as a modulation amplitude and phase angle with respect to the photolysis light for the species of interest.

In simple systems, approximate analytic expressions can be derived for phase angle and modulation amplitude in terms of rate constants, concentrations and flashing frequency.[29] The square wave photolysis function is expressed as a Fourier expansion,

$$I(t) = (I_0/2) + (2I_0/\pi) \sum_{n\ \mathrm{odd}}^{\infty} (1/n) \sin(2\pi nft) \qquad (20)$$

where t is time, f is the flashing frequency in Hz and I_0 is the intensity of the light. This is an odd function with phase angles equal to zero by definition

$$\delta_n = 0.$$

From a proposed mechanism, for example,

$$
\begin{aligned}
&N_2O_5 + h\nu \xrightarrow{j} NO + NO_2 + O_2 \\
&N_2O_5 \xrightarrow{A} NO_2 + NO_3 \\
&NO_2 + NO_3 \xrightarrow{B} N_2O_5 \\
&NO + NO_3 \xrightarrow{f} NO_2 + NO_2 \\
&N_2O_5 \xrightarrow{F/V} (\text{flow out}) \\
&NO_2 \xrightarrow{F/V} (\text{flow out}) \\
&(\text{flow in}) \xrightarrow{F} N_2O_5,
\end{aligned}
\tag{21}
$$

the rate expression for $[N_2O_5]$ can be derived. This expression,

$$
\begin{aligned}
-\frac{d[N_2O_5]}{dt} = A[N_2O_5] - B[NO_2][NO_3] + \frac{F}{V}([N_2O_5]_{out} - [N_2O_5]_{in}) \\
+ [N_2O_5]\left(\frac{j}{2} + \frac{2j}{\pi}\sum_{n\ odd}^{\infty}\frac{1}{n}\sin(2\pi nft)\right),
\end{aligned}
\tag{22}
$$

consists of chemical, flow and modulated photolytic terms. In this system NO and NO_3 are both low concentration intermediates, for which quasi-steady state solutions,

$$
[NO]_{ss} = ([N_2O_5]/f\ [NO_3])\left(\frac{j}{2} + \frac{2j}{\pi}\sum_{n\ odd}^{\infty}\frac{1}{n}\sin(2\pi nft)\right) \tag{23}
$$

and

$$
[NO_3]_{ss} = \left(A[N_2O_5] - [N_2O_5]\left(\frac{j}{2} + \frac{2j}{\pi}\sum_{n\ odd}^{\infty}\frac{1}{n}\sin(2\pi nft)\right)\right)/B[NO_2], \tag{24}
$$

are reasonable approximations. (This is not really true for [NO]). Substituting $[NO_3]_{ss}$ into the rate expression for $[N_2O_5]$ gives

$$
\begin{aligned}
-\frac{d[N_2O_5]}{dt} = 2[N_2O_5]\left(\frac{j}{2} + \frac{2j}{\pi}\sum_{n\ odd}^{\infty}\frac{1}{n}\sin(2\pi nft)\right) + \\
\text{Flow term.}
\end{aligned}
\tag{25}
$$

The flow term cancels the steady state illumination term, j/2, leaving only the modulated term. The equation can be integrated analytically if $[N_2O_5]$ is considered to be independent of time to the first order. Since modulation amplitudes are typically smaller than 10^{-3} this is a sufficiently good approximation. The modulated component of the N_2O_5 concentration is

$$[N_2O_5]_{mod} = \frac{2j}{\pi^2 f} [N_2O_5]_{ss} \left(\sum_{n\ odd}^{\infty} \frac{1}{n^2} \cos(2\pi nft) \right)$$

$$= \frac{2j}{\pi^2 f} [N_2O_5]_{ss} \left(\sum_{n\ odd}^{\infty} \frac{1}{n^2} \sin(2\pi nft + \pi/2) \right). \qquad (26)$$

A similar treatment for $[NO_2]$ results in the expression

$$[NO_2]_{mod} = \frac{3j}{\pi^2 f} [N_2O_5]_{ss} \sum_{n\ odd}^{\infty} \frac{1}{n^2} \sin\left(2\pi nft - \frac{\pi}{2}\right). \qquad (27)$$

The concentration of both of these species is modulated in a triangular fashion, the N_2O_5 leading the light by 90° and the NO_2 lagging it by 90°. The factor of two in the expression for $[N_2O_5]_{mod}$ and of three in that for $[NO_2]_{mod}$ arise from the approximation that reactions B and f occur rapidly after production of an NO in the photolysis. This is the meaning of the steady state assumptions for NO and NO_3. In this simplified treatment the modulation amplitudes are directly proportional to the light intensity, quantum yield and steady state N_2O_5 concentration and inversely proportional to the flashing frequency.

The phase angle of a species is related to its role in the chemical mechanism. Intermediates that are produced and destroyed by

processes that are fast compared to the flashing frequency, such as NO in the example above, exhibit a rapid buildup to a steady state concentration when the light is switched on and a rapid decay to zero when it is turned off. The phase angle is then near zero, since the concentration of this fast intermediate closely follows the photolyzing light. The concentration of a primary reactant which is destroyed by photolysis and replenished by flow will decay slowly while the light is on and increase slowly while it is off, oscillating about a steady state level controlled by the photolytic and flow processes. The first harmonic of this concentration modulation will therefore appear to lead the lamps by a phase angle of 90° ($\delta = +\ 90°$). A stable product of a primary photolytic step behaves oppositely, lagging the light by 90° ($\delta_n = -\ 90°$). The complete interpretation of phase angle in terms of participation in the mechanism is represented diagrammatically in Fig. 2.

The concentration modulation of a particular species is monitored in the present work by absorption spectroscopy in the infrared region. If the spectral feature observed obeys the Beer-Lambert law for absorption of light, the transmitted intensity of the spectroscopic beam passing through the reaction cell is a function of the incident intensity, the pathlength traversed, the number density of the absorber and its absorption cross section,

$$I = I_o \exp(-\sigma c l). \tag{28}$$

Small concentration fluctuations initiated by intermittent photolysis cause intensity fluctuations of the spectroscopic beam.

$$I + \Delta I = I_o \exp(-\sigma l(c + \Delta c)). \tag{29}$$

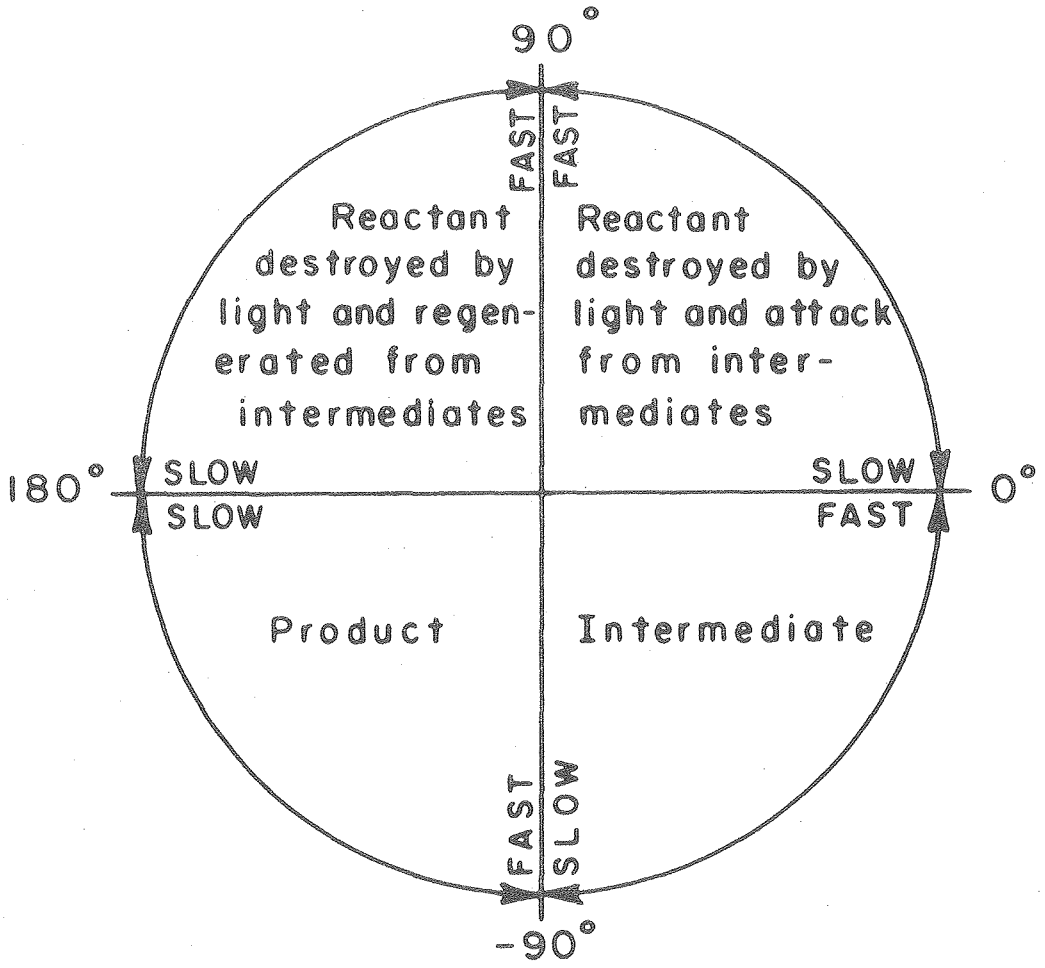

XBL6812-7446

Figure 2. Phase shifts of modulated reaction species.

So

$$I + \Delta I/I = \exp(-\sigma \Delta cl), \tag{30}$$

and if $\sigma \Delta cl$ is small compared to one, a truncated series expansion can be substituted for the exponential term,

$$I + \Delta I/I \cong 1 - \sigma \Delta cl. \tag{31}$$

Finally,

$$\Delta I/I \cong \sigma \Delta cl. \tag{32}$$

Lock-in amplification of the transmitted signal, I, yields the experimental observables, $\bar{I}$, a and b, the in-phase and quadrature amplitudes. Then, properly normalized,

$$\bar{I} = (a^2 + b^2)^{1/2}, \tag{33}$$

and

$$\delta = \tan^{-1}(b/a). \tag{34}$$

If σ and 1 are known, Δc can be calculated from ΔI. For a reactant or product species, for which the modulation amplitude is small compared to the steady state concdntration ($\Delta c/c \approx 10^{-3}$),the maximum modulation signal is obtained when the steady state optical density, ocl, is one.

Exact analytical expressions for the complete chemical mechanism can not in general be derived. Instead, highly accurate numerical solutions are generated by the CHEMK package.[30] This application of the Gear method of numerically integrating a set of stiff differential equations uses the complete set of differential rate expressions describing the complete chemical system to generate the concentration as a function of time for each species. The Fourier coefficients of the expansion of

dc/dt are calculated from the Taylor series coefficients provided by the Gear package and compared to the experimental results.

B. APPARATUS

1. Reaction Cell and Temperature Control

The reaction cell used in this work consists of a quartz cylinder, 28.0 cm in inside diameter, encased in nickel-plated stainless steel endcaps. The tube is sealed into the endcaps with silicone o-rings, to allow operation at 250 K and below. The base pathlength of the cell is maintained at 1 meter with Kovar struts connecting the endcaps. Three internally positioned gold-surfaced mirrors are mounted in the endcaps in a White cell arrangement. A fine external adjustment screw selects pathlengths from four to thirty-two meters. The volume of the cell is 63.0 l with a surface to volume ratio of 0.175 cm^{-1}.

The cell and bracket structure rests on nylon pads, intended to reduce thermal conductivity from the Newport Research vibration isolating table on which the cell and all optics are mounted. The cell is surrounded on the top and sides by 8" of rigid polyurethane foam sealed by 2" of aluminum-backed fiberglass. It is separated from the table by 2" of high density closed cell neoprene foam. Temperature control is achieved with a finned radiator coil mounted above the cell through which cooling fluid circulates. The coil is wrapped with resistive heating wire for fine control. The current passing through the wire is varied in a closed loop operated by a proportional temperature controller employing a precision thermistor as the sensing element. An internally mounted muffin fan circulates the air around the cell.

Methanol is used as the coolant for temperatures below 278 K. The coolant is chilled in a Neslab LT9 low temperature circulator and pumped to an insulated elevated 22 l surge tank. The flow is maintained both by gravity and siphoning action. For higher temperatures chilled water is utilized as the coolant. The temperature is monitored by a precision low temperature thermometer as well as four iron-constantan thermocouples. Three thermocouples are radially disposed about the quartz cell wall, while the fourth is located in a stainless stell thermowell extending about 30 cm into the cell from one endcap. The temperature gradient about the cell, from top to bottom, was less than 0.5 K at all experimental temperatures.

The schematic diagram of the experiment is shown in Fig. 3. The cell is pumped with an oil diffusion pump protected by a liquid nitrogen cooled trap. It can be evacuated to pressures less than 0.13 Pa.

2. Optical System

All external optics are enclosed in a plexiglass box purged with a stable trickle of nitrogen, to minimize spectral interference from water and CO_2. The light from an Infrared Industries regulated 2×12 mm Nernst glower passes through an American Time Products 400 Hz chopper and is focused by a collector mirror through a 6 mm KBr window. This window is mounted on the end of an evacuated Pyrex tube through which the source light passes to reach the KBr window mounted in the cell endcap. This window and the Pyrex protecting tube are mounted with silicone o-rings to permit evacuation, in order to protect the highly hygroscopic windows from damage due to condensation during low temperature experiments.

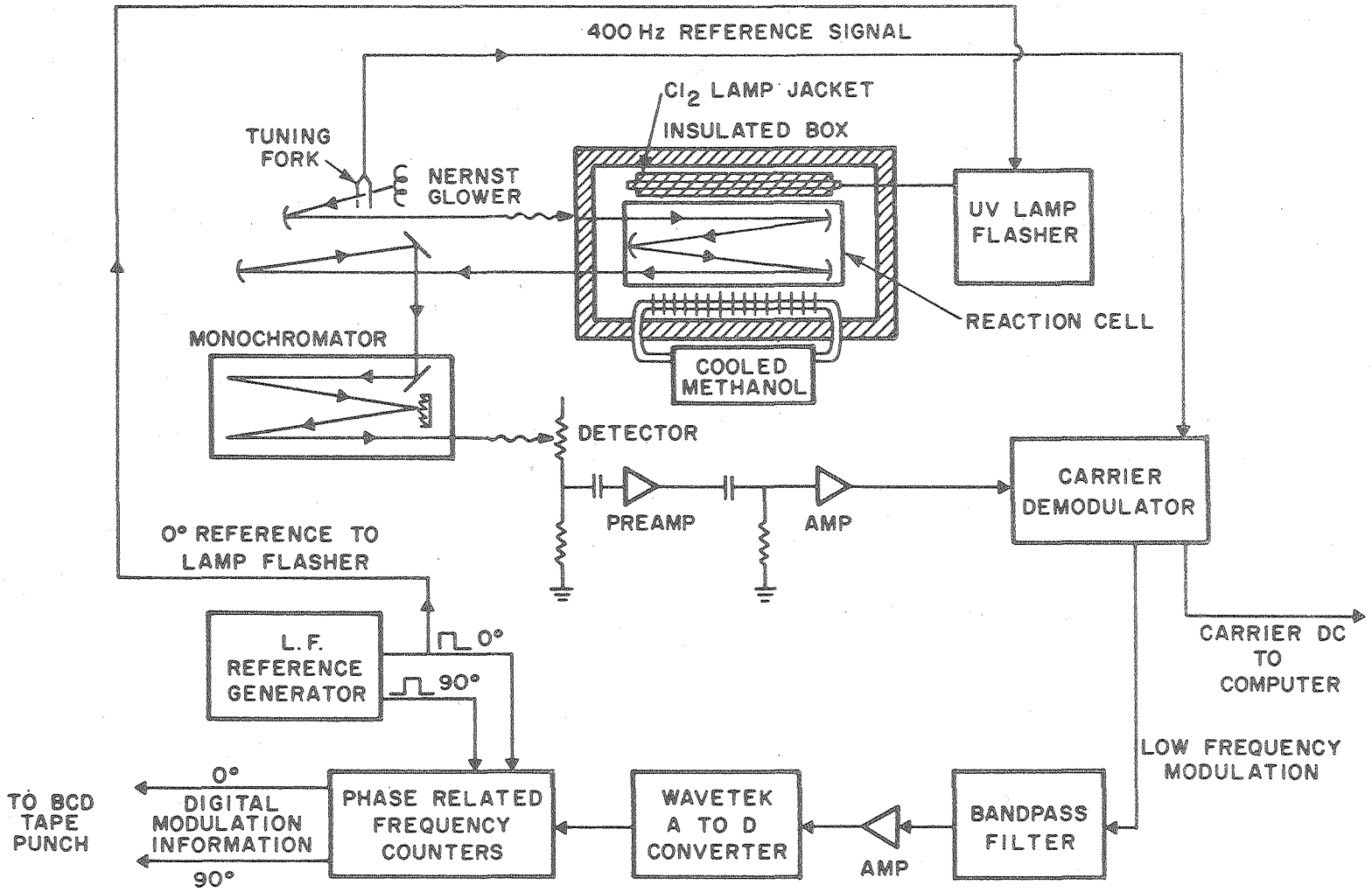

Figure 3. Schematic diagram of experimental apparatus.

In addition the evacuated tube reduces thermal conduction into the cooled box. After passing through the cell the light exits through an identical double window arrangement to another gold surface collector mirror which focuses the Nernst glower image onto the entrance slit of the McPherson Model 2051 one meter monochromator. The optical arrangement is such that the internal mirrors and the external collector mirror are slightly underfilled, while the monochromator entrance slit is overfilled, in order to minimize signal fluctuations due to vibration. The monochromator is equipped with order sorting filters and a 150 line/mm grating, blazed at 8 microns.

3. Detector

The infrared detector is a Santa Barbara Research Center copper-doped germanium photoconductor operated at liquid helium temperature (4 K). The field of view of the detector is reduced to about 40° by a liquid nitrogen cooled shield, to reduce background room temperature radiation. The cooled detector acts as a 2 MΩ resistance and the associated Johnson noise, as well as shot noise and background radiation, comprise the largest unavoidable noise sources in the system. This noise is unavoidable because of the wide bandwidth necessary to pass the low frequency modulation information carried as sidebands on the 400 Hz carrier modulation. The peak-to-peak noise level is about 20 μV against a total signal of about 50 mV. The modulation information is present as a low frequency ripple of amplitude as small as 2 μV, necessitating long term signal averaging.

The photoconductive detector is balanced by a metal film resistor of approximately equal value, with the circuit biased at 135 V such that the detector current provides the maximum signal to noise ratio. The detector output, modulated at 400 Hz by the tuning fork chopper, is capacitively coupled to an ultra-low noise operational amplifier. The preamplifier circuit is shown in Fig. 4. It is mounted as closely as possible physically to the detector to reduce pickup.

4. Signal Processing

The preamplifier has an overall bandpass of 320-520 Hz at the 3dB level and is operated at a gain of about 600 at 400 Hz. The shorted input noise level of 5.8 mV rms referred to the output is small compared to the 100 mV rms detector current noise at the output. The signal output is on the order of 0 to 12 V AC.

The signal is modulated at the 400 Hz tuning fork frequency to remove the chemical modulation information from the low frequency region of 1/f electronic noise. The modulation information, when present, is carried as 400 ± f Hz sidebands, where f is the frequency of the photolysis lamps. The low frequency f Hz signal modulation as well as the higher harmonics of the 400 Hz carrier are removed by bandpass filtering.

The 400 Hz carrier is rectified by one of two lock-in amplifiers operating from the 400 Hz reference supplied by the tuning fork driver. In the absence of chemical modulation of the signal, the rectified output is passed through integrating filters of variable time constant, producing a DC voltage proportional to the intensity of infrared radiation striking the detector. The molecular modulation signal is amplified and rectified

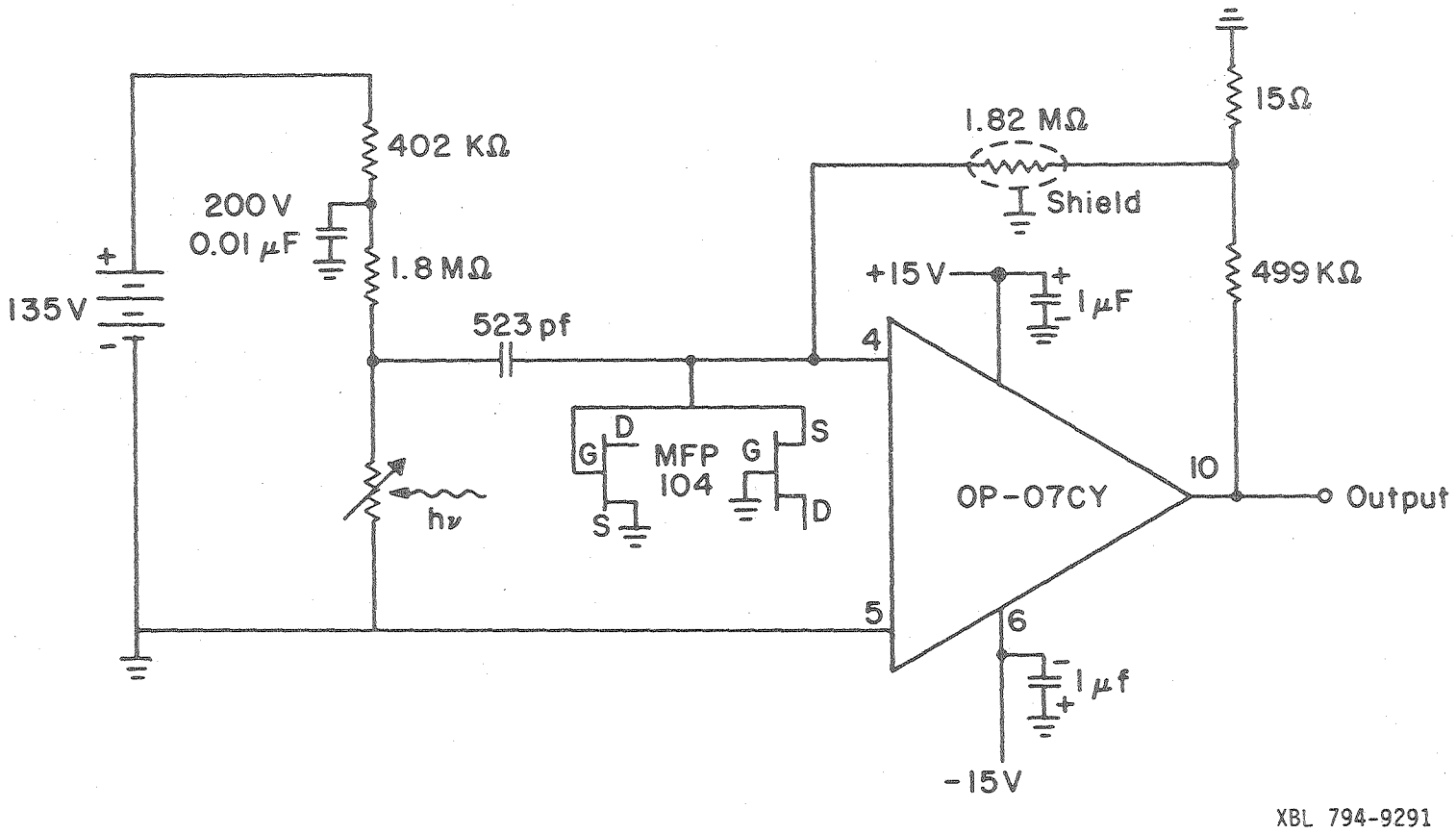

Figure 4. Preamplifier circuit.

by the carrier demodulator and then split into two parts. The first is a DC level with a low frequency AC ripple carrying the modulation information. The second is smoothed with filters and measured as a DC level with a digital voltmeter. This signal is also recorded on the Fabritek 1074 instrument computer.

The modulated signal is processed by selected low frequency band-pass filters, which pass the prescribed flashing frequency, e.g. $\frac{1}{4}$ Hz. The resulting signal is amplified and used to drive a Wavetek Model 11 operated as a voltage controlled oscillator. The 5 kHz center frequency corresponds to no signal at the inputs of the dual phase demodulator. The f Hz AC signal modulates the Wavetek square wave output frequency up or down in a fashion directly proportional to the amplitude of the AC input. It thereby operates as an analog to digital converter.

Two up/down frequency counters serve as signal averagers. The counters are gated by two references generated by the lamp flashing driver, one shifted 90° with respect to the other. The in-phase counter counts the Wavetek output as an odd function, that is adding counts for the first half of the cycle (light on) and subtracting for the second half (light off). The out of phase, or quadrature, counter counts as an even function, subtracting for the first and fourth quadrants, and adding the second and third. Since both counters operate up and down for equal periods during a cycle, random noise, being uncorrelated with the photolysis lamps, averages to zero. Any signal with frequency components at the flashing frequency will produce a net signal.

The gating references to the counters must be exact to avoid biasing the signal. The reference pulses are generated by dividing down

the output of a crystal oscillator to give a square wave signal at frequencies which are multiples of 0.306 Hz. Most of the molecular modulation work was carried out at a nominal flashing frequency of 0.25 HZ. For this case the divided oscillator output at 1.22 Hz is divided by two twice to produce a square wave signal at 0.306 Hz, used to gate the in phase counter and connected optoelectronically to the lamp power supply to flash the lamps. The optoelectronic coupling is necessary to prevent the power supply switching from appearing as signal in the dual phase demodulator. The 0.306 Hz and the 0.612 Hz frequencies from the oscillator are fed to an exclusive OR gate to produce the quadrature reference.

After a selected number of cycles, the contents of the counters are punched on a paper tape in BCD code for later interpretation, the counters are zeroed and the experiment repeated. The value in the in-phase counter is proportional to the amplitude of the sine (odd) component of the modulation signal. Similarly the out-of-phase counter total is proportional to the cosine component. The modulation amplitude is

$$\Delta I/\ I \propto (a^2 + b^2)^{1/2} \text{ / DC output of the carrier demodulator.} \tag{35}$$

The phase angle is

$$\phi = \tan^{-1}(b/a). \tag{36}$$

The proportionality factor for the amplitude expression is determined by measuring the number of counts obtained for an input signal of known modulation amplitude.

The coefficients for the full Fourier expansion of a concentration profile all contain kinetic information, but are usually reduced in

magnitude compared to the first harmonic. For example the next higher harmonic, the third, in the triangular waveform expected for N_2O_5 has a coefficient $1/3^2$ or a factor of nine smaller than the first. Since the noise is usually large in these experiments the higher harmonics are lost. Consequently the signals are filtered to remove the higher harmonics and simplify the interpretation of the results. The low frequency bandpass filters, centered on the frequency of the fundamental, also reduce the random noise. The carrier lock-in cancels the even harmonics, while the filters reduce the third harmonic by a factor of six. The square wave nature of the demodulation switching reduces it by a further factor of three, so that overall the third harmonic for N_2O_5 would be diminished by 1/162. All higher harmonics are also negligible.

The filtering, however, produces phase shifts in the modulation signal which are a function of frequency. In addition a proportionality factor is needed to relate the rms counts per volt of DC signal to the amplitude of intensity modulation. A modulation standard is used to provide these values.

The circuit shown in Fig. 5 produces as square wave modulation amplitude of 2×10^{-3} with a phase shift of 0° on the 400 Hz carrier provided by the tuning fork reference. The output of this circuit is subjected to all signal processing. The relative amplitude of the first harmonic of the square wave is $4/\pi \times 10^{-3}$. At each flashing frequency to be used the number of counts per volt for an amplitude of $4/\pi \times 10^{-3}$ is measured. The measured phase angle provides a subtractive correction at that frequency to account for electronic phase shifting of the input signal.

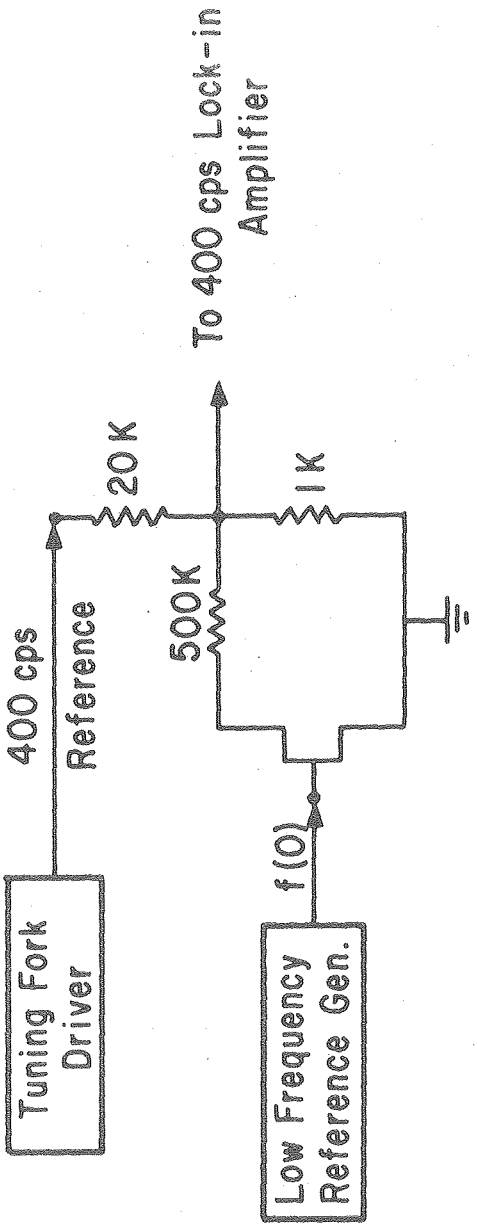

XBL 759-7268

Figure 5. Modulation standard.

The lockin output in a DC experiment is monitored on a digital voltmeter and recorded with a Fabritek 1074 hardwired signal averager. The analog signal is smoothed with a variable time constant integrating filter and digitized and stored at preset intervals by a 12 bit A-D. All or part of the 4K of 18 bit words in memory can be filled. Long term storage of spectra is possible by transferring the data through a PDP 8/L computer interfaced to the Fabritek, via an interprocessor buffer to a PDP 8/E computer and thence to magnetic tape.

The BCD coded paper tape produced in a modulation experiment is read into the 8/L on a high speed paper tape reader and repunched by a high speed punch in ASCII code. This tape is reread by the computer, which calculates modulation amplitudes, phase angles and standard deviations.

The modulation simulation program is run on the CDC 7600 computer located at the Lawrence Berkeley Laboratory. A version[31] of this program, which lacks the Fourier coefficient calculations, was implemented on a PDP 11/10 with 24K of 16 bit memory. For systems of up to 20 chemical species and 30 reactions it is competitive with the entire process of running a program on the LBL system.

5. Photolytic Source

The photolysis lamps employed in these experiments are 30 watt GE G30T8 low pressure mercury germicidal lamps. The four lamps are deployed symmetrically about the cell at a distance of 8 cm from the cell wall. The output of these lamps in general includes most of the mercury emission lines starting with the 254 nm ultraviolet line and extending

into the visible. The visual color of the lamps is blue indicating the predominant presence of the 405 and 436 nm lines in the visible. Several unwanted phtochemical side reactions may occur as a result of the presence of various emission lines. The chief problems are the photolysis of NO_2, which absorbs over the entire region of the mid and near ultraviolet and visible, and of NO_3, which absorbs strongly in the yellow-red portion of the visible.

The thermodynamic cutoff for production of ground state products, $NO(X\ ^2\pi) + O(^3P)$, from the photolysis of NO_2 occurs at about 398 nm, but there is a residual pressure dependent quantum yield for production of O atoms up to 440 nm.[32] The 254 nm line is used to photolyze N_2O_5 since NO_2 has a fortuitous dip in its absorption cross section in this region. The other lines which can interfere by photolyzing NO_2, the 313, 366 and to a certain extent the 405 nm lines, are suppressed by inserting the germicidal lamps into double-walled concentric quartz jackets, filled with an atmosphere of chlorine. The strong chlorine absorption band between 300 and 400 nm diminishes the intensity of these lines while passing the desired 254 nm radiation. The effect of the chlorine filters is shown in Fig. 6. The emission of the lamps with and without the filters was observed with a McPherson Model 218 0.3 meter monochromator equipped with a PAR 1205D optical multichannel analyzer as detector. The spectra shown are uncorrected for the spectral response of the OMA, but the relative peak heights with and without the filters show substantial reduction of the unwanted lines. An additional phototube and monochromator were used to observe the unfiltered lamp output and showed the intensity of the 313 and 366 nm lines to be about 2% of the 254 nm line. The

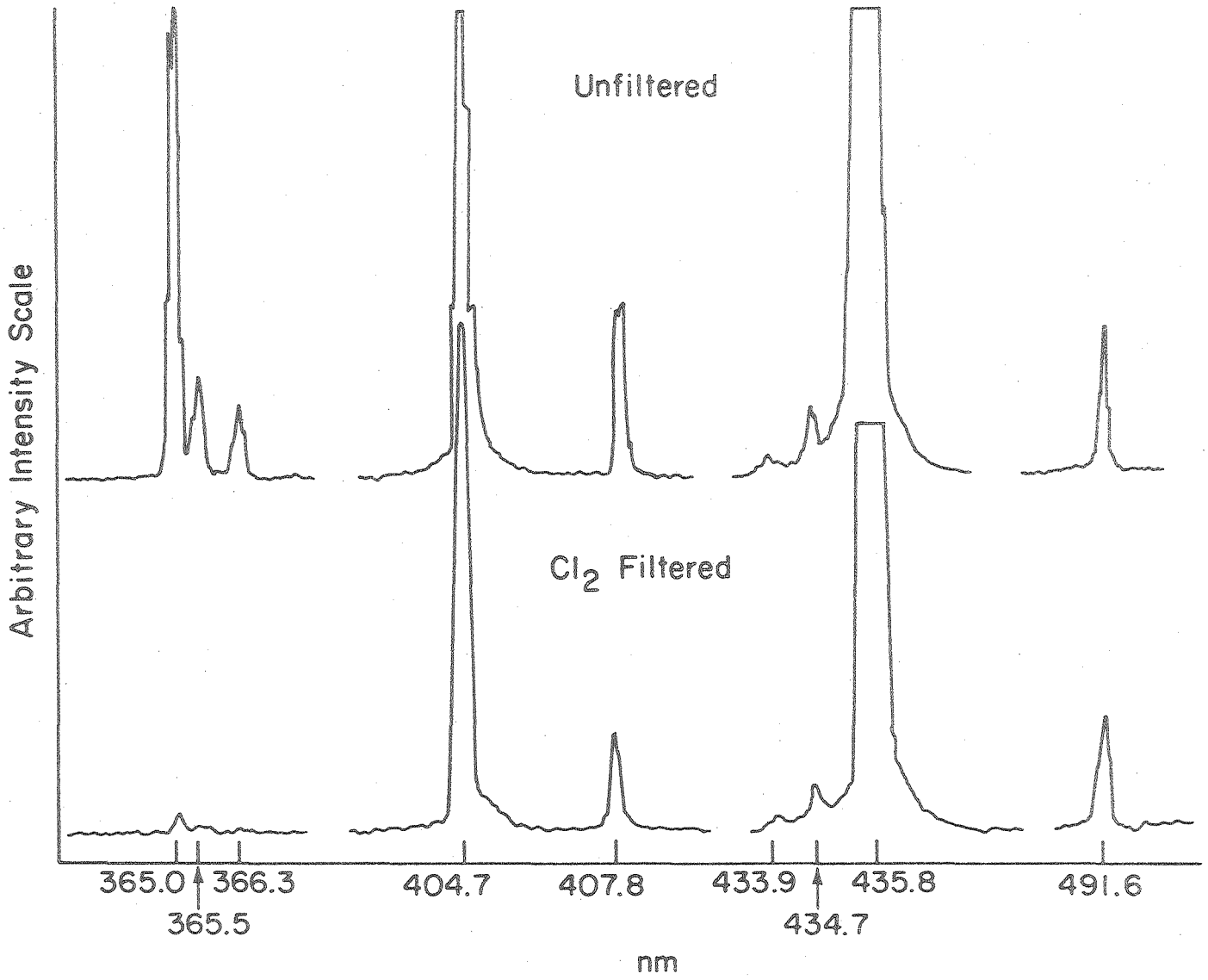

XBL 794-9332

Figure 6. Comparison of Cl_2 filtered and unfiltered photolysis lamp output.

chlorine jackets also serve to maintain the wall temperature of the lamps when the cell is cooled. Lamp output has a strong direct proportionality to wall temperature.

The 577 nm line, which would be active in dissociating NO_3, was searched for unsuccessfully, using an RCA 9258 phototube mounted on a McPherson 2051 one meter monochromator with a 1200 line/mm grating blazed at 300 nm. The next line, at 623 nm, if present would not be photochemically active.[27,33]

The cell and lamp assembly is surrounded on three sides by Alzak reflective aluminum sheets to maximize the photolytic intensity and increase the uniformity of light flux across the cell. At room temperature the intensity of 254 nm radiation in the cell is about 8×10^{15} photons$\cdot$cm$^{-2}\cdot$sec^{-1}, decreasing with temperature to 3×10^{15} photons$\cdot$cm$^{-2}\cdot$sec^{-1} at 252 K.

The lamp electrodes are heated to a red glow by six volt transformers to ensure rapid firing at low temperatures. The lamps are powered by a 700 V regulated power supply, which can power the lamps continuously or switch them on and off in response to the low frequency reference.

An EG&G UV100B photodiode was used continuously to monitor relative lamp output. A significant and variable portion of the lamp output resides in the two blue Hg lines, to which ordinary photodiodes are much more sensitive. In order to be sure that only the intensity of thr 254 nm light contributed, the UV-enhanced photodiode was placed behind an interference filter with 12% transmittance at 254 nm and a bandpass (FWHM) of about 15 nm. The output of the photodiode is amplified by a

factor of 100 with an operational amplifier, the input resistance of the amplifier serving as the load resistance for the photodiode. The maximum photocurrent drawn was kept well within the device's linear response region. Mounted internally, the photodiode is subject to cooling as the cell is cooled. The subsequent increase in responsivity at 254 nm is about 7% from 300 to 250 K.

C. GASES AND FLOW SYSTEM

High dry grade nitrogen and oxygen used in this study were supplied by the Lawrence Berkeley Laboratory. The nitrogen passed through a particulate filter and a U-tube packed with Linde 3A molecular sieve placed in a liquid nitrogen filled dewar in order to remove moisture. The oxygen was flowed through a column of 5% palladium on an alumina substrate at 620 K to convert hydrocarbon impurities to CO_2 and water. Ascarite and P_2O_5-coated glass bead columns removed these contaminants. The flow was directed through a U-tube packed with silica gel held at 196 K for further drying, before passing either through the ozonizer or to the cell. The supplier quotes the following impurity maximums:

	High Dry Nitrogen	High Dry Oxygen
N_2	99.999%	500 ppm
O_2	1.5 ppm	99.5%
H_2O	1.5 ppm	1.5 ppm
CO_2	---	10 ppm
Ar	5 ppm	4000 ppm

Nitric oxide from the Matheson Company was passed through a column of silica gel at 196 K to remove the NO_2 traces as N_2O_3. The nitric oxide was collected at liquid nitrogen temperatures. The pale blue product was freeze/thaw pumped and used without further purification.

Nitrogen dioxide of 99.5% purity from the Matheson Company was collected at 196 K and then stored under an atmosphere of oxygen for several days at room temperature, in order to oxidize residual NO. The NO_2 was then subjected to several freeze/thaw pumping cycles to remove the oxygen. The resulting white solid was stored at 196 K.

Dinitrogen pentoxide was prepared using the method of Schott and Davidson.[34] An oxygen flow, purified in the manner described above, was split into two streams. One passed to an Ozone Research and Equipment Company ozonator which produced a stream of about 7% ozone in oxygen. The other stream was bubbled through liquid NO_2/N_2O_4 at 262 K. The stream with the entrained NO_2 passes through a flow regulating needle valve and is mixed with the ozone stream. The exothermicity of the reaction between O_3 and NO_2 warms the Pyrex tubing to the touch for several centimeters in the mixing region. The flows are adjusted so that the brown color of the nitrogen dioxide is totally absent after the junction and ozone can be detected at the exhaust. The flow is then diverted into a Pyrex saturator in a dewar at 196 K.

The needle-shaped white crystals are collected until the NO_2 in the bubbler is exhausted. The oxygen is pumped off and the N_2O_5 is stored at 196 K until use. Warming to 273 K produced no visible NO_2 and spectroscopic examination in the IR showed less than 1% NO_2 and around

10% HNO_3. The HNO_3 is presumably formed by heterogeneous reaction of N_2O_5 with water on the walls of the manifold and lines. Since the system is not bakeable the production of HNO_3 was unavoidable.

All gas handling took place in a Pyrex line with stainless steel greaseless Ultra-Torr fittings. The fittings and the Kontes high-vacuum greaseless Teflon and glass bore stopcocks were equipped with Viton o-rings, greased with a small amount of Apiezon H, L or N grease. The manifold was evacuated with a liquid nitrogen trapped glass oil diffusion pump. Gas pressures were measured with a Texas Instruments model 145 quartz spiral manometer.

Gases were expanded or flowed into the cell through a disperser tube. The disperser tube has holes spaced at 1" intervals on alternate sides made such that the pressure drop across the holes is large compared to the pressure drop along the tube. An even distribution of gas throughout the cell is thus provided immediately upon filling. The exhaust is through a similar tube. The pressure drop through the cell at one atmosphere under flowing conditions was about 2 kPa. Flow rates were measured at the cell inlet with Manostat Predictability flowmeters.

Flowing at low pressures was accomplished with a Granville Philips automatic pressure controller. A Pace capacitance manometer measured the pressure in the cell to provide feedback for a servo-driven variable leak valve at the cell inlet. The exhaust was conducted to a Welch Duo-seal mechanical pump.

III. EXPERIMENTAL PROCEDURES AND DATA

A. INFRARED ABSORPTION CROSS SECTIONS

Absorption cross sections as functions of optical density and temperature for infrared spectral bands of NO_2 and N_2O_5 were determined as

$$\sigma(\lambda) = \ln (I_o(\lambda)/I(\lambda))/cl, \qquad (37)$$

where c is the number density and l the pathlength. The spectrometer was employed as a single beam instrument, $I_o(\lambda)$ being recorded and stored, followed by measurement of $I(\lambda)$. The baselines of absorption spectra are adjusted linearly when necessary to be zero in regions where no species absorb. All spectra and sepcies monitoring in kinetic runs were recorded at 0.013 μm resolution. Spectra were scanned at a rate of 0.08 μm/min for NO_2 and 0.16 μm/min for HNO_3 and N_2O_5. Points were recorded at intervals of 0.4 sec with a 1 second time constant. The 6.1 - 6.4 μm IR band of NO_2 used in this study exhibits marked dependence on the total pressure shown in Fig. 7, presumably a result of pressure broadening of rotational lines. Consequently all NO_2 optical densities were measured at 1 atm total pressure. HNO_3 and N_2O_5 absorptions were free of pressure dependence between 1.3 Pa and 1 atm.

The NO_2 cross sections were measured by collecting a sample of purified NO_2 in a 273.6 cm^3 bulb at room temperature (295 K), recording the pressure with the TI spiral manometer and then expanding the sample into the cell. Residual NO_2 in the bulb and lines was entrained into the cell with the nitrogen used to bring the total pressure to an atmosphere. Corrections for dimerization of NO_2 to N_2O_4 in both the bulb

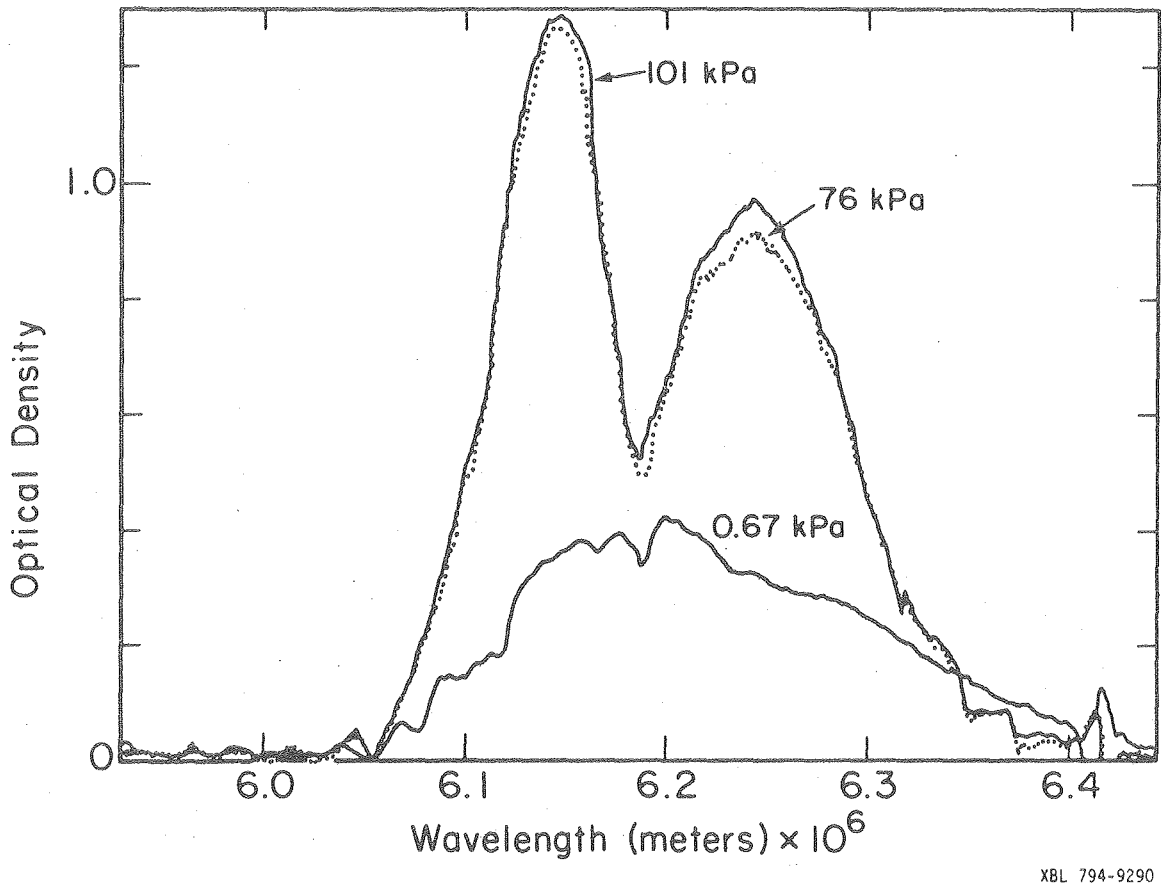

Figure 7. Pressure dependence of the 6.2 μm NO_2 absorption.

and cell were applied, calculated from the data of Verhoek and Daniels.[35] The concentration of NO_2 determined was used in Eq. (37) to calculate the cross section, $\sigma(\lambda)$. Figure 8 shows the absorption at 295 K, with an 8 meter pathlength and an NO_2 concentration of 9.29×10^{14} molecules/cm^3. At lower temperatures the peaks narrow and become taller as expected for the narrowing rotational distributions. The values of σ at 6.25 μm, the center of the P-branch, given below were obtained by averaging three optical density data points about this wavelength.

$$\begin{aligned} A = 1;\ \lambda = 6.25\ \mu m \qquad & \sigma(295\ K) = 9.1 \times 10^{-19}\ cm^2/molecule \\ & \sigma(287\ K) = 9.3 \times 10^{-19} \\ & \sigma(268\ K) = 9.7 \times 10^{-19} \\ & \sigma(262\ K) = 9.8 \times 10^{-19}. \end{aligned} \tag{38}$$

The absorption coefficients so obtained are dependent on optical density. Figure 9 is a plot of absorption coefficient at 6.25 μm versus optical density at 262 K. The expression,

$$\sigma(262\ K) = (1.082 - 0.10\ A) \times 10^{-18}\ cm^2/molecule \tag{39}$$

was used to derive NO_2 concentrations from measured optical densities. The value of 9.6×10^{-19} cm^2/molecule obtained by Alan Harker,[36] a former graduate student, under similar conditions at 1 atm and room temperature, with an unknown optical density, is in reasonable agreement with the present results.

Several attempts to measure the cross sections of N_2O_5 and HNO_3 by the method of Harker[36] and Graham[37] met with no success. Their technique involves a stabilized flow of NO_2 and O_2, to which is added sequentially without change in the flowrates, ozone and water. The ozone quantitatively converts the NO_2 to N_2O_5 and the water converts the N_2O_5 to

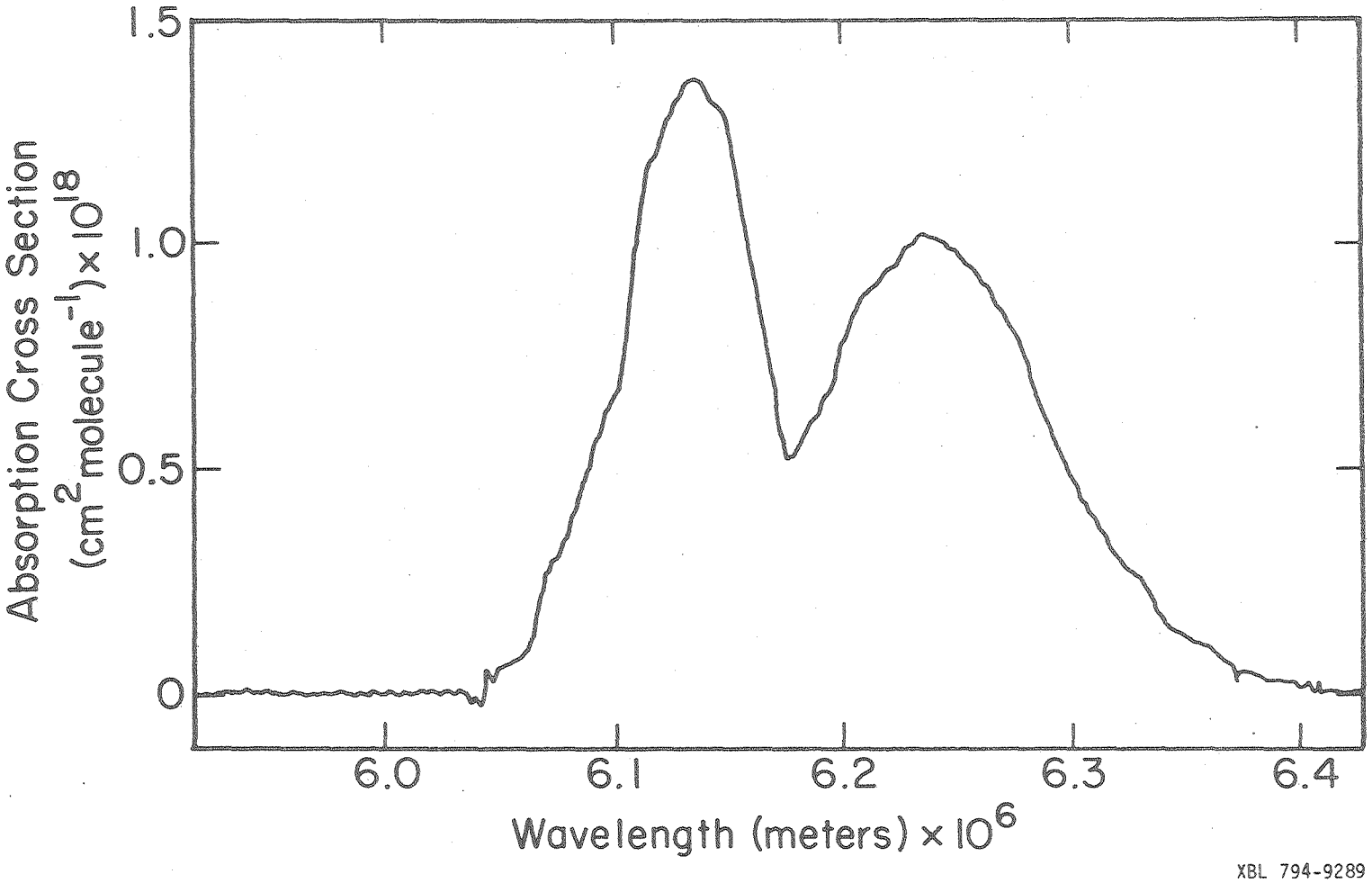

Figure 8. Nitrogen dioxide (NO_2) infrared spectrum at 295 K. (NO_2 optical density = 0.68).

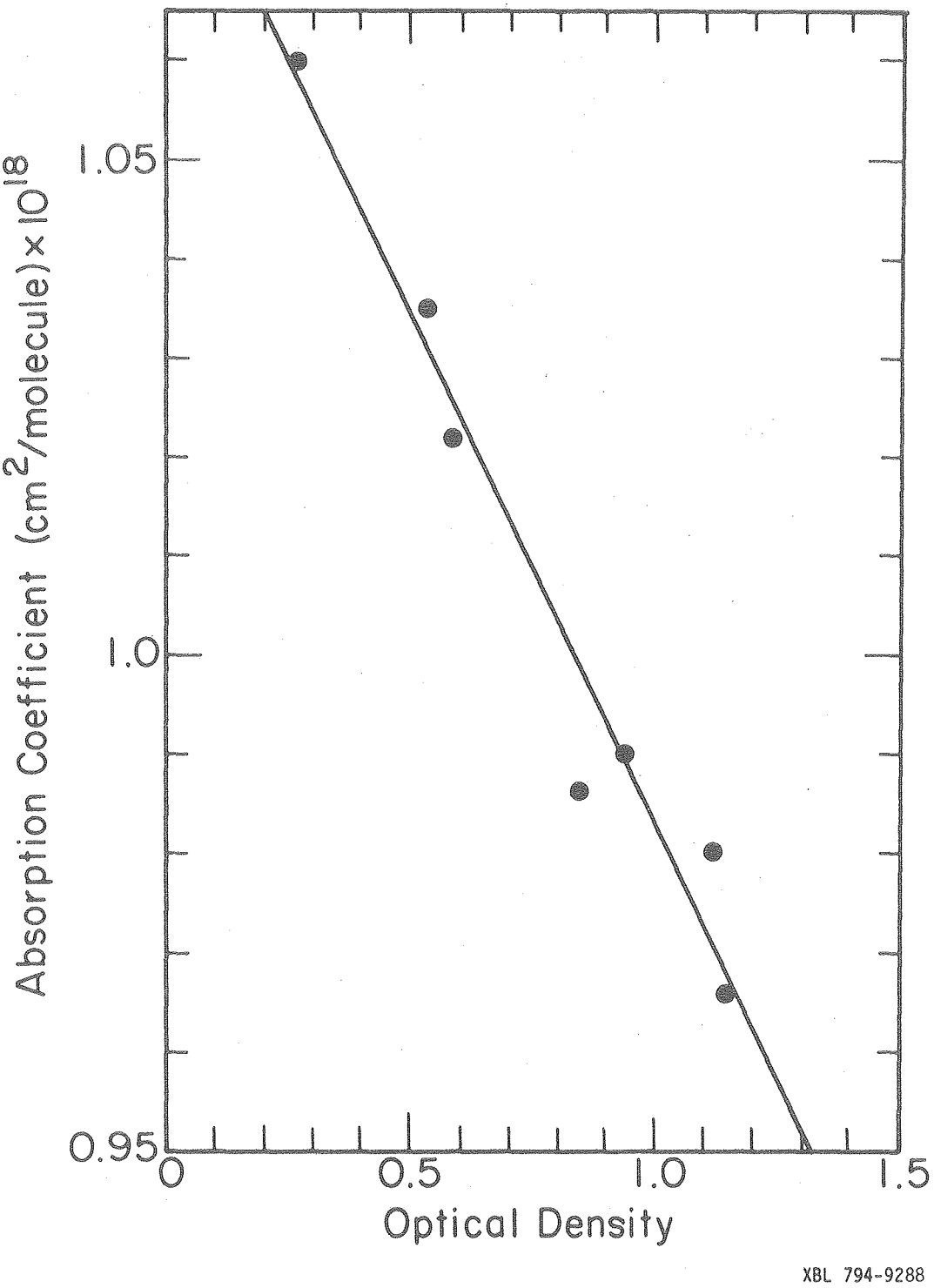

Figure 9. Dependence of the absorption coefficient of NO_2 at 6.25 μm on optical density at 262 K.

HNO_3. The NO_2 absorption coefficient, previously measured, and mass balance considerations are used to compute the cross sections for N_2O_5 and HNO_3. The nitric acid formation step relies on an heterogeneous reaction, which gave unpredictable results in the present work.

Instead, it was found that N_2O_5 could be produced and collected while maintaining NO_2 impurity levels to less than 1%, and HNO_3 to a relatively reproducible 10-12%. Samples of N_2O_5 were measured into a small bulb at room temperature and then quickly expanded into the cell. The region of interest was scanned and the nitric acid present was corrected for using the absorption cross sections of Grahma.[37] The cross sections of N_2O_5, measured as the average of three points about 8.028 μm, the center of the Q-branch, show no dependence on total pressure or optical density between 0.2 and 3.3 absorbance units. The N_2O_5 absorption is shown in Fig. 10. The cross section values at 8.028 μm are:

$$0.2 \leqslant A \leqslant 3.3,\ \lambda = 8.028\ \mu m$$

$$\begin{aligned} \sigma(295\ K) &= (1.77 \pm 0.05) \times 10^{-18}\ cm^2/molecule \\ \sigma(272.5\ K) &= (1.83 \pm 0.1) \times 10^{-18} \\ \sigma(268\ K) &= (1.91 \pm 0.05) \times 10^{-18}. \end{aligned} \tag{40}$$

The room temperature value agrees well with the results of both Harker and Graham. The temperature dependence observed by Graham above room temperature also extends in a fairly linear fashion below it. The temperature dependence of the NHO_3 absorption cross section used to correct the N_2O_5 pressure is weak, about a per cent per ten degrees, and because of the relative amounts of N_2O_5 and HNO_3 in the original sample, an error of 5% in the determination of HNO_3 concentrations will produce an error

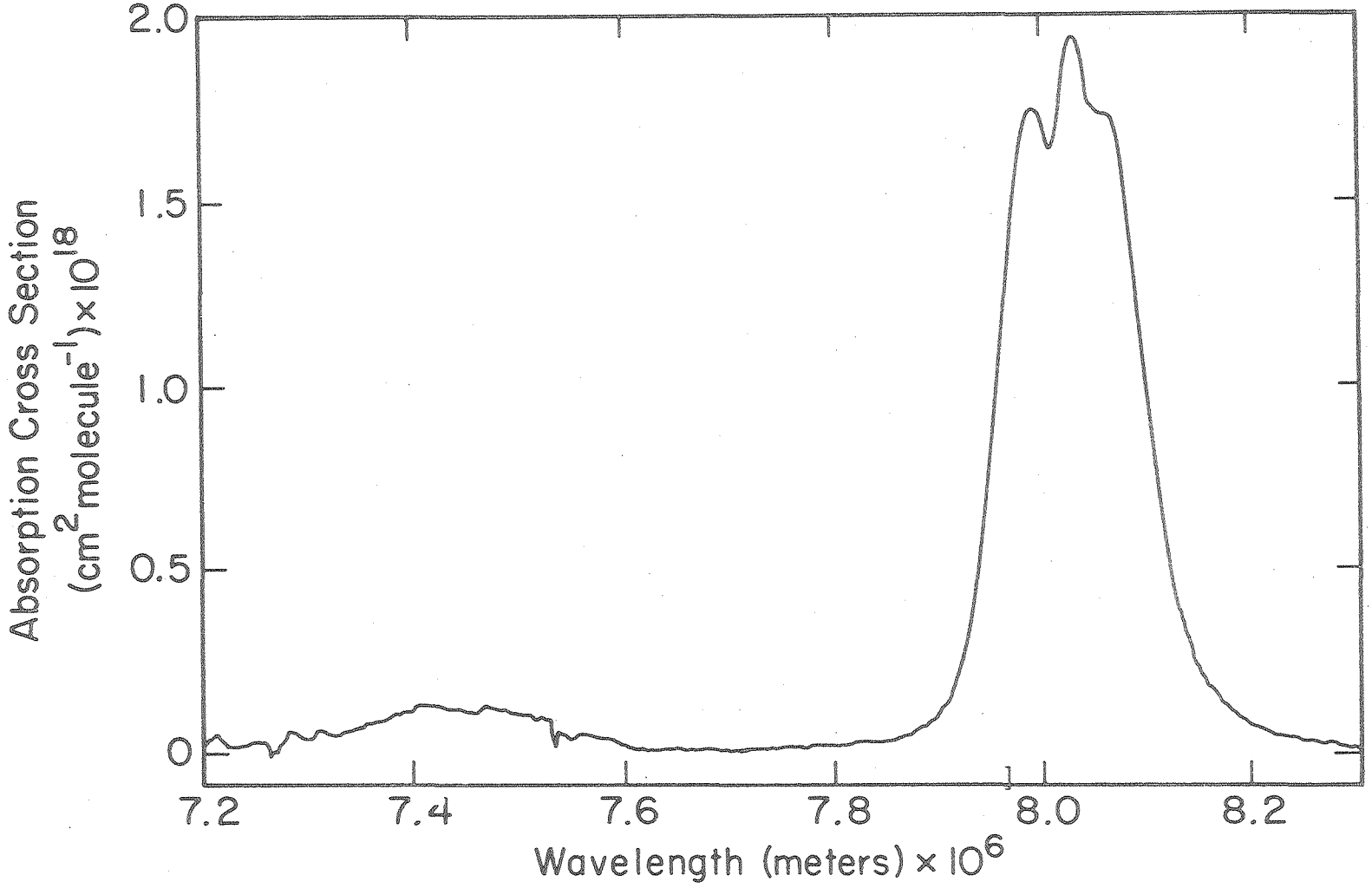

XBL 794-9331

Figure 10. Dinitrogen pentoxide (N_2O_5) infrared spectrum at 268 K.

of less than 1% in the calculation of N_2O_5 cross sections.

Two alternate independent methods were used to check the results at various temperatures. In the first a stable flow of N_2O_5 in a carrier gas of either nitrogen or oxygen at atmospheric pressure was established at 268 K. Spectra of NO_2, N_2O_5 and HNO_3 were recorded, then the germicidal lamps were turned on and the system was allowed to come to photochemical equilibrium. The change in NO_2 concentration was calculated from the change in absorbance, corrected for dimerization and divided by the stoichiometric factor of two from

$$N_2O_5 + h\nu \longrightarrow 2\ NO_2 + \frac{1}{2} O_2 \qquad (41)$$

to obtain the change in N_2O_5 concentration. The HNO_3 level remained fairly constant. The value of $1.90 \pm 0.07 \times 10^{-18}$ cm^2/molecule derived by dividing the change in N_2O_5 absorbance by its calculated change in concentration agrees with the values above.

The second set of independent cross section measurements was obtained by measuring the NO_2 produced during a thermal decomposition experiment. In this case the stoichiometric ratio of NO_2 produced is three,

$$N_2O_5 + NO \longrightarrow 3\ NO_2. \qquad (42)$$

Again corrections for NO_2 dimerization and in this case for heterogeneous loss of N_2O_5, first order decay that does not produce NO_2, were applied. Cross sections determined in this way were also in agreement within experimental error, which is larger for this method because of the need to correct for heterogeneous production of HNO_3. This correction becomes large at low temperatures for which the heterogeneous rate

constant. From the initial concentration of N_2O_5 calculated from the NO_2 produced, and from the measured pressure of the N_2O_5 sample an estimate of the HNO_3 concentration can be made. The HNO_3 absorption is shown in Fig. 11 and the cross section is determined as an average of three points about 7.605 μm, the center of the P-branch. Since the initial charge of HNO_3 was usually small and the cross section is based on the remaining difference of large numbers, the value of $1.0 \pm 0.3 \times 10^{-18}$ is a crude estimate, but it falls within experimental error of the value of Graham.

B. THERMAL DECOMPOSITION EXPERIMENTS

The unimolecular thermal decomposition rate of N_2O_5 was measured in the IR cell as a function of temperature and total pressure. In the presence of excess NO, the decomposition reaction is rate determining in the scheme;

$$\begin{aligned} N_2O_5 + M &\xrightarrow{A} NO_2 + NO_3 + M \\ NO + NO_3 &\xrightarrow{f} 2\ NO_2. \end{aligned} \qquad (43)$$

Since the absorption cross section of N_2O_5 is independent of optical density over the experimental range, the rate constant for reaction A is obtained from the slope of the first order plot of $\ln(A_{N_2O_5}(t=0)/A_{N_2O_5}(t))$ as a function of time, where A(t) is the absorbance of N_2O_5 at time t. Knowledge of the absolute concentration of N_2O_5 is necessary only in calculation of the total effective pressure. The empirical rate constant is free of errors introduced by absorption coefficients or pressure measurements. The total pressure was considered constant over the reaction

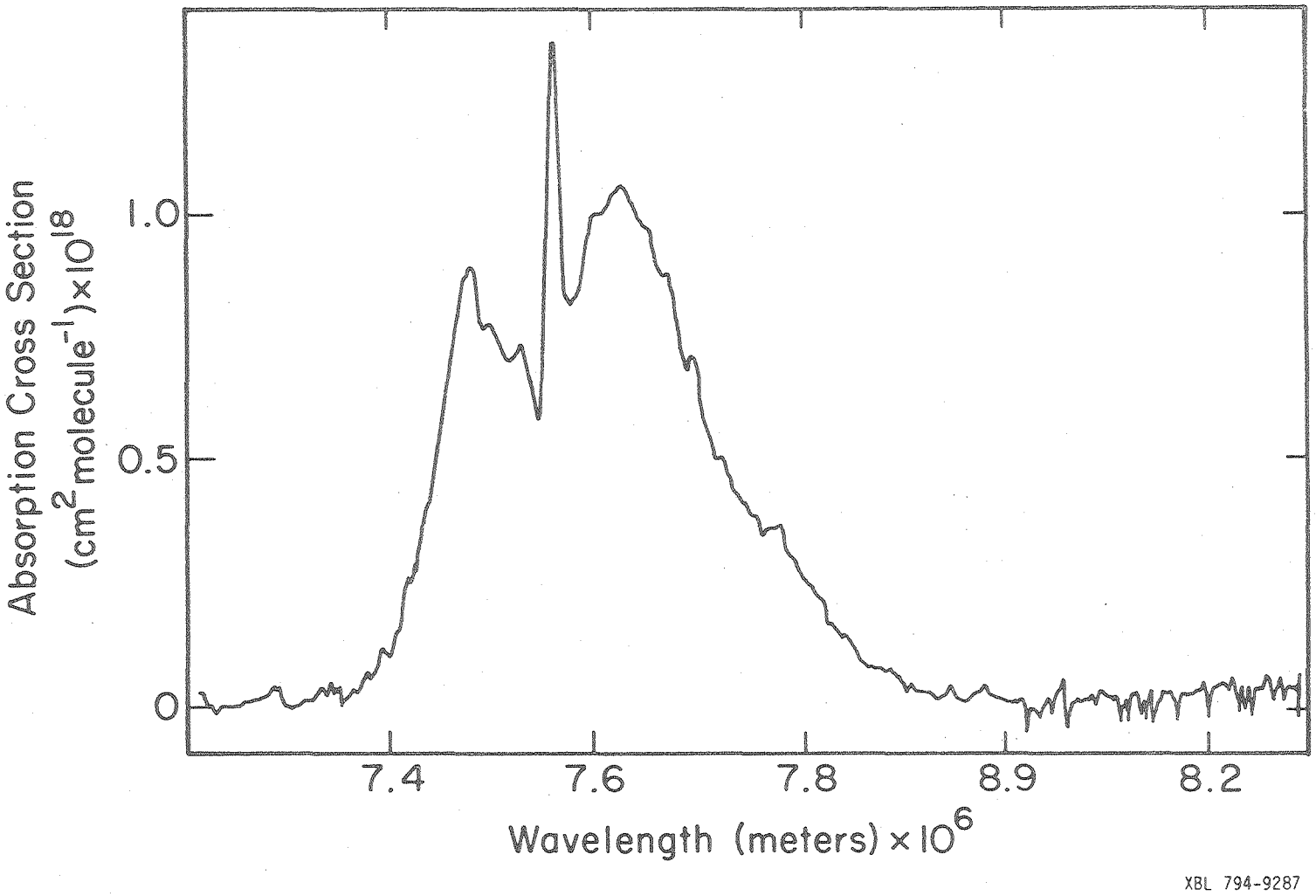

Figure 11. Nitric acid (HNO_3) infrared spectrum at 268 K.

period, typically because the reactant concentrations were much smaller than the total pressure. In the lowest pressure experiments in which only pure reactants were used, the efficiency for activation of N_2O_5 by the products was considered equal to that of the reactants. The simple exponential N_2O_5 decays observed in these experiments indicate this to be a reasonable assumption.

Two different reactant mixing methods were used to test the possibility of inadequate mixing in the cell. Initially the sample of N_2O_5 was measured into a 273.6 cm^3 bulb close to the cell inlet and then quickly expanded into the evacuated cell. The measured NO sample was then expanded into the cell through the same disperser tube, along with any buffer gas. The jetting action of the gas expanding from the many small holes in the disperser tube was intended to provide turbulent mixing of the reactants.

To ensure complete mixing, the second method used involved reactant mixing at a three-way stopcock external to the cell. Measured pressures of N_2O_5 and NO were placed into bulbs of 80.15 and 81.74 cm^3 or 5328 and 5442 cm^3 displacement. The bulbs were then pressured equally with nitrogen and the two mixtures were admitted into the evacuated cell through a three-way stopcock. If necessary additional buffer gas was added subsequently. In both alternatives to filling the cell an interval for mixing was allowed before monitoring of the 8.028 μm N_2O_5 absorbance commenced. Results from the two methods were identical within experimental error.

When practical the N_2O_5 decay was followed for two or three half-lives and in almost all cases was characterized by a single exponential factor. Individual empirical decay contants were obtained by a linear least square fit to the 1024 data points, plotted as $\ln(A_o/A)$ vs. t, where $A(t) = \ln(I_o/I(t))$. The standard deviation of the decay constant, the slope of the semilog plot, was typically smaller than 1%.

The thermal decomposition constant is the difference between the empirical rate constant of N_2O_5 disappearance in the presence of excess NO and the heterogeneous loss rate constant in the absence of NO. This constant is determined by interspersing runs without added NO. The rate constant for decay in the pure N_2O_5 system is corrected for the homogeneous contribution of

$$\begin{aligned} N_2O_5 + M &\xrightarrow{A} NO_2 + NO_3 \\ NO_2 + NO_3 &\xrightarrow{e} NO + NO_2 + O_2. \end{aligned} \tag{44}$$

This correction is about 4×10^{-5} sec^{-1} at room temperature[26] and is negligible below room temperature.

The cell was conditioned, or "aged", by exposure to N_2O_5 and deconditioned by exposure to other gases, undried gases and leakage from the atmosphere. Evacuating the cell between experiments did not affect the heterogeneous decay rate constant. In their work on the reaction of dinitrogen pentoxide with water, Morris and Niki[23] reported an heterogeneous loss constant of 6 to 8×10^{-4} sec^{-1} in a 67 liter Pyrex conditioned cell. Heterogeneous decay constants in the present work varied from 1×10^{-3} sec^{-1} for the initial runs to as low as 7×10^{-5} sec^{-1} after the cell was well conditioned.

A few heterogeneous runs were conducted for which both N_2O_5 disappearance and HNO_3 appearance were monitored by alternating the monochromator between the respective wavelengths. In these runs, HNO_3 appeared at a rate of 50 to 75% the rate of N_2O_5 disappearance, indicating that a considerable fraction of the HNO_3 formed remained on the walls.

The total effective pressure in the cell was calculated from the initial values of N_2O_5, NO and N_2 concentrations, determined by applying the perfect gas law to the measured pressures in the small bulbs. The partial pressures of N_2O_5 and NO were multiplied by their relative activational efficiencies with respect to N_2 of 4.27 and 1.28, as determined by Johnston.[8] The total pressure is then expressed as the number density of nitrogen:

$$[N_2]_{TOT} = [N_2] + 4.27[N_2O_5] + 1.28[NO]. \qquad (45)$$

Nitric acid was taken to have the same efficiency as N_2O_5.

The data set is given in Table 2 and plotted in Fig. 12. The time required to fill the cell with the reactants restricted the observations to rate constants smaller than 10^{-2} sec^{-1}. The error in individual empirical decay constants, less than 1%, is small compared to the error introduced by the determination of the heterogeneous constant. In a well conditioned cell, the reproducibility of a particular experimental result fell within about 5×10^{-6} sec^{-1}, but for most runs the irreproducibility was on the order of 2×10^{-5} sec^{-1}. The errors from this largest recognized source of imprecision vary from 1% for fast rate constants (high T and P) to about 80% for the slowest measured constants. Figure 13 shows a representative plot of the decay of N_2O_5 in the presence

TABLE TWO

[N2O5]	[NO]	EFF [N2]	K(UNI)X1E4 SEC(-1)
307.0 K			
7.44E+13	9.75E+13	4.42E+14	0.95 +/- 0.10
8.20E+13	8.33E+13	4.57E+14	1.00 +/- 0.10
2.18E+14	2.55E+14	1.25E+15	2.10 +/- 0.20
4.22E+14	5.20E+14	2.47E+15	3.90 +/- 0.20
4.26E+14	5.15E+14	2.48E+15	4.60 +/- 0.20
8.39E+14	1.06E+15	4.94E+15	8.10 +/- 0.20
6.37E+14	9.28E+14	6.42E+15	11.30 +/- 0.20
6.32E+14	9.72E+14	6.62E+15	11.30 +/- 0.20
6.52E+14	9.45E+14	1.09E+16	17.50 +/- 0.20
6.32E+14	9.70E+14	1.09E+16	17.90 +/- 0.20
6.46E+14	1.04E+15	1.88E+16	27.90 +/- 0.30
6.73E+14	1.07E+15	1.92E+16	27.50 +/- 0.30
6.46E+14	8.80E+14	3.73E+16	46.00 +/- 0.30
7.36E+14	8.76E+14	3.79E+16	46.00 +/- 0.30
295.0 K			
2.13E+14	2.43E+14	1.22E+15	1.04 +/- 0.10
4.26E+14	4.72E+14	2.42E+15	1.41 +/- 0.10
5.80E+14	1.70E+15	4.67E+15	2.50 +/- 1.00
6.42E+14	1.61E+15	4.81E+15	2.85 +/- 0.10
1.15E+15	1.71E+15	4.91E+15	3.00 +/- 1.00
6.32E+14	2.42E+15	5.80E+15	3.30 +/- 0.10
6.30E+14	7.42E+14	6.73E+15	4.55 +/- 0.10
1.16E+15	3.48E+15	9.40E+15	6.00 +/- 3.00
6.38E+14	1.08E+15	1.11E+16	6.80 +/- 0.05
1.44E+15	4.16E+15	1.15E+16	6.00 +/- 2.00
5.93E+14	1.78E+15	1.47E+16	8.00 +/- 1.00
6.22E+14	1.02E+15	1.96E+16	10.80 +/- 0.10
1.14E+15	1.76E+15	2.53E+16	12.00 +/- 1.00
6.55E+14	1.02E+15	3.75E+16	17.50 +/- 0.20
1.15E+15	1.72E+15	5.57E+16	22.00 +/- 1.00
1.14E+15	1.53E+15	7.62E+16	28.00 +/- 2.00
6.29E+14	9.11E+14	7.66E+16	28.30 +/- 0.20
7.19E+14	1.58E+15	1.16E+17	33.20 +/- 1.00
5.99E+14	1.58E+15	3.02E+17	67.50 +/- 1.00
5.69E+14	2.23E+15	3.03E+17	68.50 +/- 1.00
287.0 K			
7.38E+14	8.67E+14	5.44E+16	3.80 +/- 0.50
5.75E+14	1.20E+15	2.74E+17	24.30 +/- 0.50
6.13E+14	1.42E+15	2.98E+18	76.50 +/- 0.50

[N2O5]	[NO]	EFF [N2]	K(UNI)X1E4 SEC(-1)
272.5 K			
5.71E+14	6.57E+14	6.28E+16	2.00 +/- 0.30
4.33E+14	9.36E+14	1.25E+18	7.90 +/- 0.30
1.30E+15	4.96E+15	2.04E+18	9.30 +/- 0.10
7.08E+14	6.54E+15	4.10E+18	11.60 +/- 0.10
5.72E+14	1.03E+15	7.24E+18	13.00 +/- 0.30
7.08E+14	6.23E+15	7.82E+18	13.90 +/- 0.20
1.56E+15	4.18E+15	1.56E+19	16.50 +/- 0.20
5.83E+14	6.66E+14	1.87E+19	14.50 +/- 0.30
1.73E+15	8.92E+15	2.63E+19	18.70 +/- 0.50
268.0 K			
8.09E+14	7.95E+14	4.47E+15	0.05 +/- 0.04
6.72E+14	1.66E+15	5.00E+15	0.03 +/- 0.03
6.30E+14	8.52E+14	6.21E+15	0.07 +/- 0.04
6.33E+14	1.20E+15	7.08E+15	0.05 +/- 0.05
6.43E+14	1.00E+15	1.09E+16	0.11 +/- 0.05
6.11E+14	1.18E+15	1.09E+16	0.06 +/- 0.03
6.51E+14	9.50E+14	1.11E+16	0.12 +/- 0.04
6.55E+14	1.05E+15	1.85E+16	0.50 +/- 0.50
6.68E+14	9.05E+14	1.88E+16	0.50 +/- 0.50
6.44E+14	1.07E+15	2.03E+16	0.20 +/- 0.06
7.21E+14	1.02E+15	2.18E+16	0.21 +/- 0.02
6.55E+14	1.04E+15	3.91E+16	0.48 +/- 0.02
7.64E+14	2.88E+15	7.08E+16	0.85 +/- 0.02
6.43E+14	1.04E+15	7.78E+16	0.95 +/- 0.03
6.37E+14	1.69E+15	1.47E+17	1.34 +/- 0.03
6.23E+14	4.38E+15	3.68E+17	2.14 +/- 0.03
1.16E+15	2.08E+15	4.53E+17	2.31 +/- 0.02
7.64E+14	4.74E+15	5.61E+17	2.79 +/- 0.02
6.23E+14	6.54E+15	1.05E+18	3.40 +/- 0.04
6.55E+14	8.05E+14	1.14E+18	3.40 +/- 1.00
5.66E+14	2.80E+15	2.04E+18	4.02 +/- 0.03
7.92E+14	6.65E+15	2.08E+18	4.20 +/- 0.03
6.47E+14	4.00E+15	2.12E+18	4.40 +/- 0.10
6.38E+14	4.22E+15	2.14E+18	4.10 +/- 0.10
8.64E+14	7.91E+15	2.15E+18	4.30 +/- 0.10
7.22E+14	2.80E+15	3.84E+18	4.90 +/- 0.10
1.03E+15	5.54E+15	3.88E+18	5.16 +/- 0.10
1.13E+15	1.08E+15	4.10E+18	4.60 +/- 0.05
9.06E+14	1.36E+15	7.79E+18	5.32 +/- 0.05
1.08E+15	1.08E+15	1.59E+19	5.90 +/- 0.10
7.14E+14	2.06E+15	2.78E+19	7.30 +/- 0.10

[N2O5]	[NO]	EFF [N2]	K(UNI)X1E4 SEC(-1)
262.0 K			
9.53E+14	8.41E+14	5.68E+16	0.30 +/- 0.30
1.13E+15	2.22E+15	1.03E+18	1.60 +/- 0.10
8.49E+14	2.22E+15	2.03E+18	1.70 +/- 0.10
6.51E+14	2.16E+15	4.08E+18	1.80 +/- 0.10
5.55E+14	8.08E+14	7.64E+18	1.85 +/- 0.20
1.02E+15	2.88E+15	7.71E+18	2.00 +/- 0.10
1.02E+15	2.49E+15	1.54E+19	2.40 +/- 0.10
8.49E+14	2.36E+15	2.66E+19	2.50 +/- 0.10
5.59E+14	1.42E+15	2.78E+19	2.60 +/- 0.20

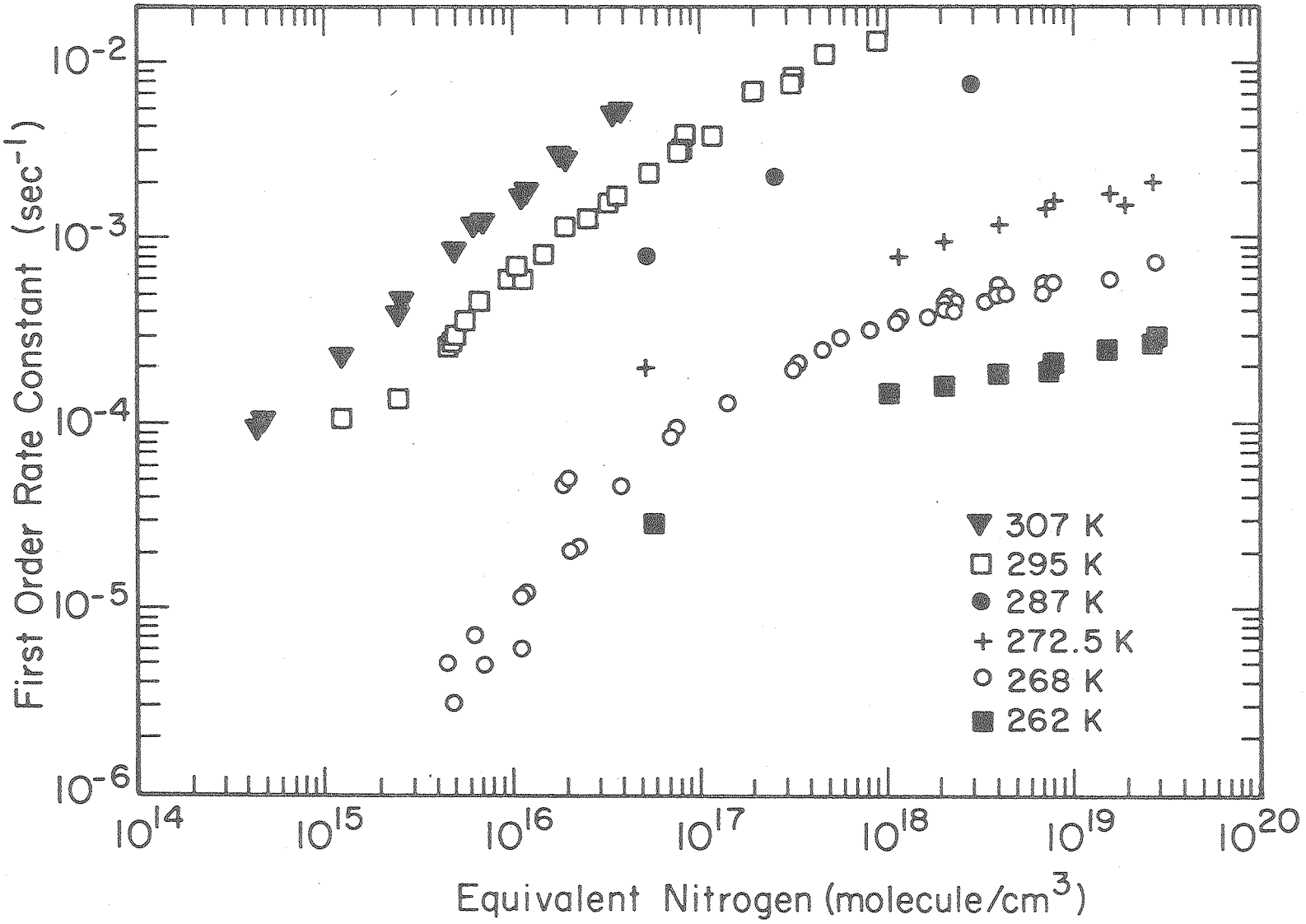

XBL 794-9328

Figure 12. First order thermal decomposition constants of N_2O_5 in N_2.

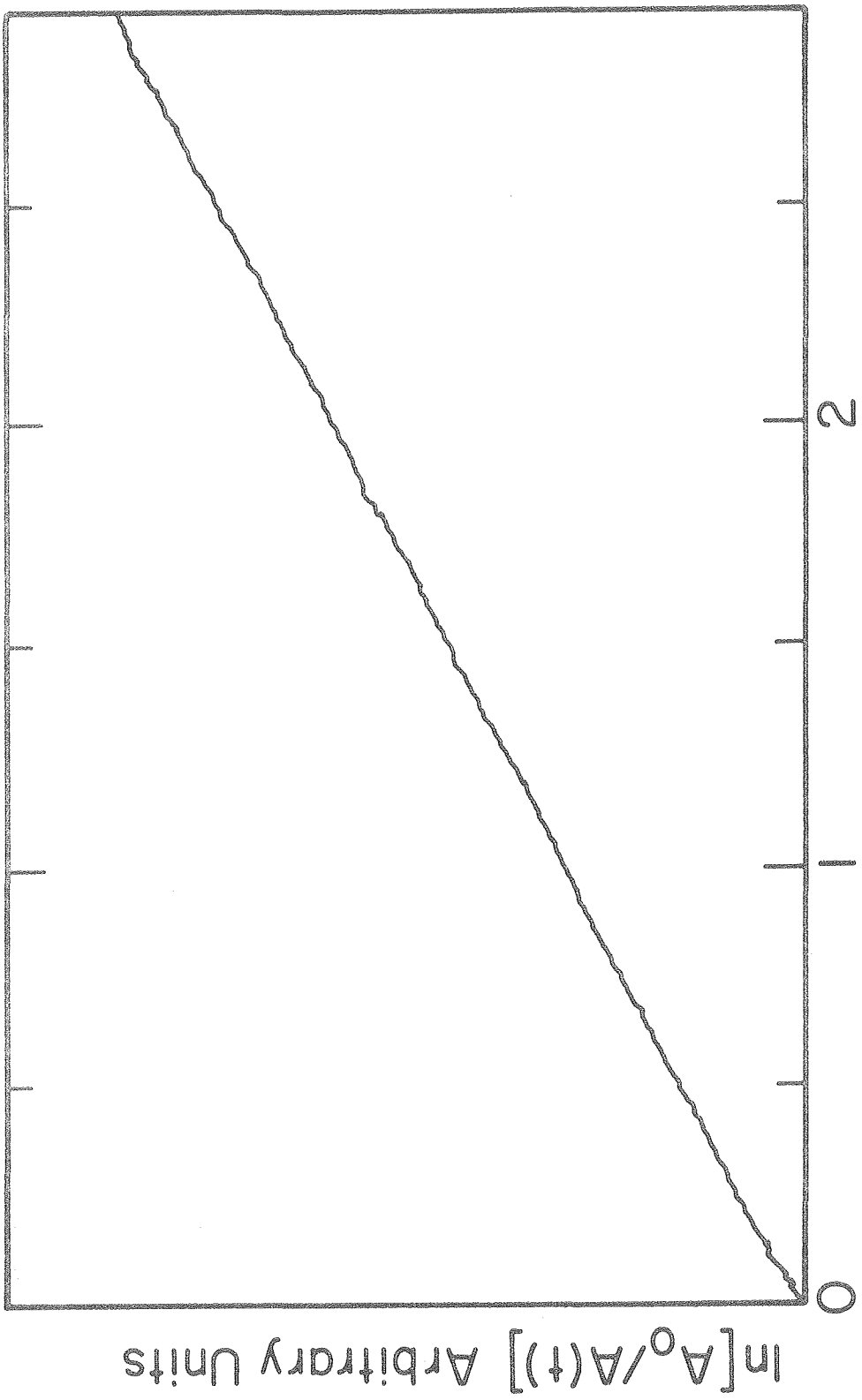

Figure 13. Experimental thermal decomposition curve.

of NO obtained at 287 K. Figure 14 is the plot of the heterogeneous decay of N_2O_5 in nitrogen at 266 K.

Several data points at room temperature (297 K) and 268 K were also obtained through observation of NO_2 absorbance in the visible at 435.6 nm. This work was performed with a Cary 118C UV/Vis spectrometer with external optics mated to a stainless steel cell of 8.285 l volume and optical pathlength of 2.95 m. This apparatus, with its associated vacuum system and temperature control was constructed by a coworker, Gary Selwyn. A run was initiated by preparing a mixture of NO and N_2 in a 3.03 l bulb. A sample of N_2O_5 was measured into a 251.0 cm^3 bulb close to the cell and admitted to the evacuated cell before irreversible decomposition to NO_2 could take place. The NO/N_2 mixture was then flushed through the N_2O_5 bulb into the cell. The NO_2 absorbance as a function of time was recorded on a strip chart recorder until the conversion of N_2O_5 to NO_2 was complete. Since the visible absorption of NO_2 in this region is free of dependence on pressure or optical density,[32] the rate constant can be calculated from the equation

$$\ln \frac{A(NO_2)_\infty - A(NO_2)_o}{A(NO_2)_\infty - A(NO_2)_t} = k_{uni}t. \qquad (46)$$

Under the experimental conditions corrections for the dimerization of NO_2 were always less than 2% of the total concentration. Figure 15a and 15b show a representative run at each temperature. The rate constants are listed in Table 3 and plotted in Fig. 12 corrected for the 2 K temperature difference. The agreement with the reactant loss data is quite

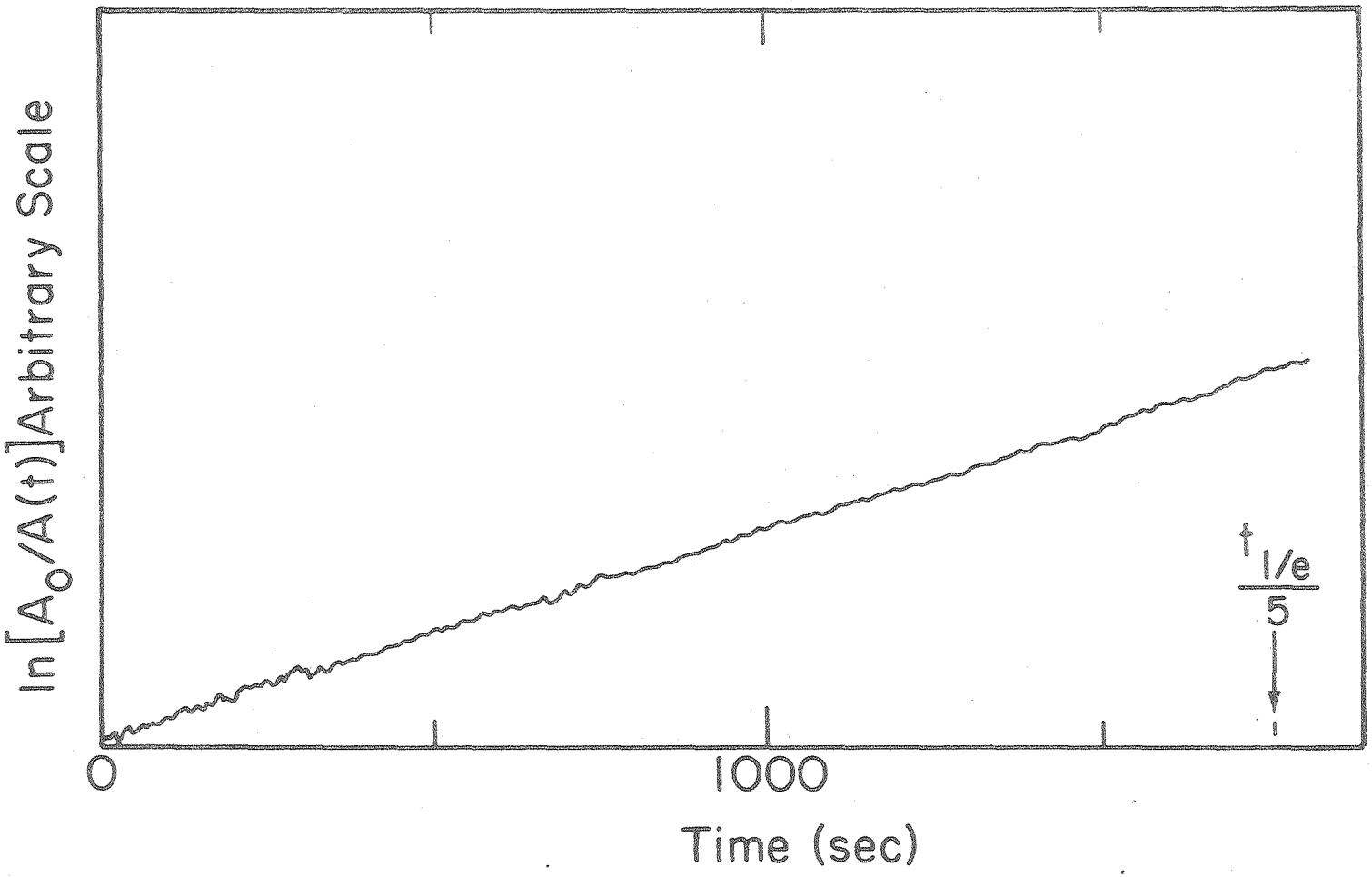

XBL 794-9319

Figure 14. Experimental heterogeneous decomposition curve.

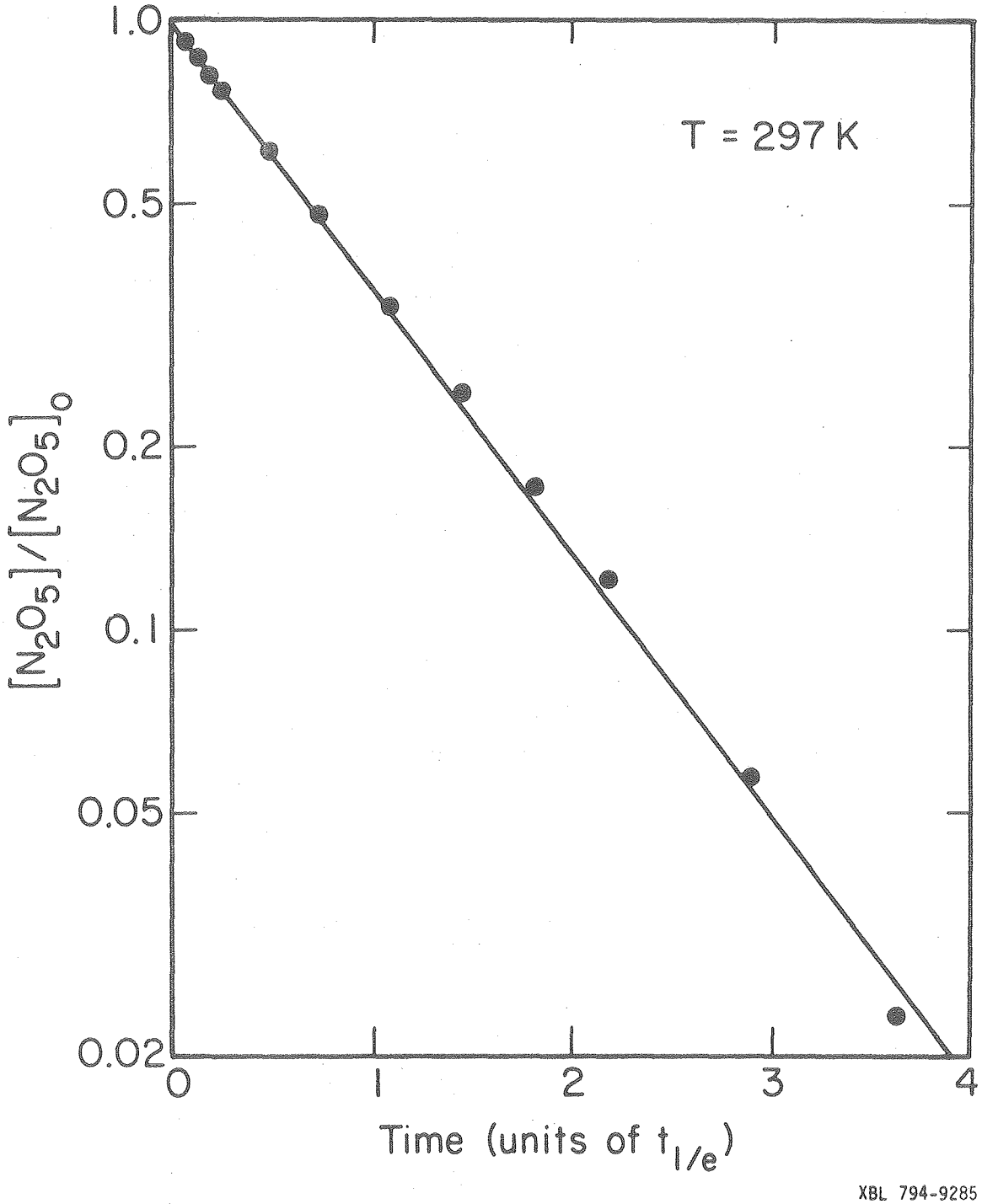

Figure 15a. Experimental N_2O_5 decomposition curve at 297 K from NO_2 appearance.

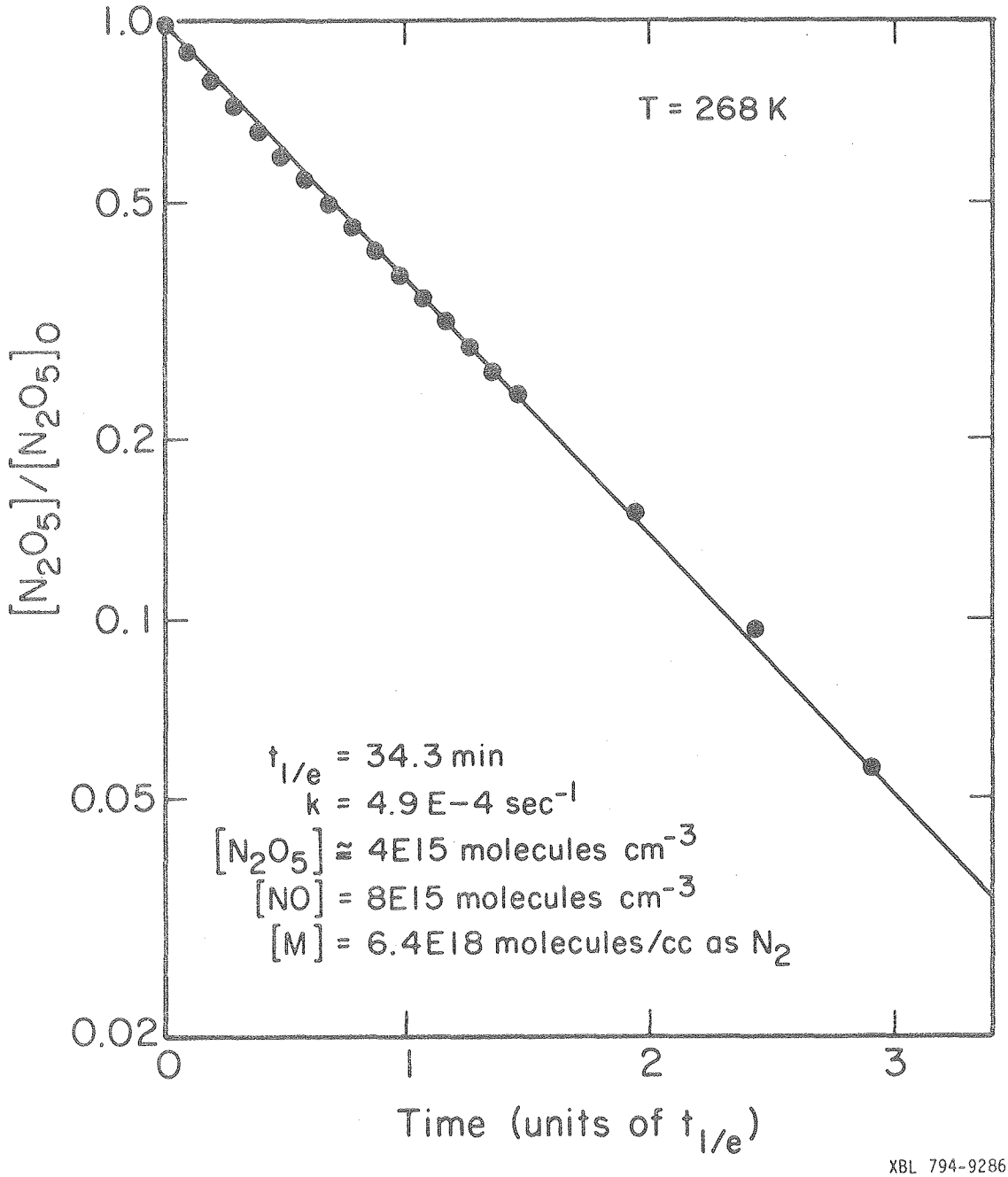

Figure 15b. Experimental curve at 268 K.

TABLE THREE

[N2O5]	[NO]	EFF [N2]	K(UNI)X1E4 SEC(-1)
297.0 K			
1.50E+15	1.50E+15	6.82E+15	5.60 +/- 0.20
2.28E+15	1.22E+16	2.53E+16	18.00 +/- 0.50
2.50E+15	4.78E+16	7.18E+16	44.00 +/- 1.00
2.50E+15	8.00E+15	1.87E+17	80.00 +/- 3.00
2.60E+15	8.13E+15	4.47E+17	119.00 +/- 5.00
9.80E+14	6.50E+15	8.31E+17	141.00 +/- 5.00
268.0 K			
3.80E+15	7.80E+15	3.17E+17	2.02 +/- 0.20
3.80E+15	7.80E+15	8.15E+17	3.09 +/- 0.30
3.90E+15	7.80E+15	1.63E+18	3.40 +/- 0.30
3.80E+15	7.80E+15	3.20E+18	4.40 +/- 0.30
4.00E+15	8.00E+15	6.40E+18	4.90 +/- 0.30
3.80E+15	7.80E+15	6.70E+18	5.70 +/- 0.30

good. Several data points obtained at higher pressures at room temperature were discarded as anomalously low as a result of inadequate mixing of the reactants in the cell.

C. CLOSED CELL PHOTOLYSES

Photolysis of a chemical species in an optically thin cell under constant irradiation is a first order process in the absence of complicating secondary reactions. The photolytic rate constant, "j", the product of the incident intensity, absorption cross section and quantum yield, can be measured in the same way as the first order decomposition rate constants evaluated above. By proper choice of conditions the restriction on the presence of secondary reactions can be made more or less applicable for N_2O_5.

Experimental procedures were similar to those described in the previous section. The cell was evacuated, the transmitted IR intensity at 8.028 μm was recorded amd the photolytic lamps were powered in order to allow them to rise to operating temperature and stable UV output. Lamp output was monitored by the UV100B photodiode. The N_2O_5 was then expanded from the 273.6 cm^3 bulb into the cell, along with the buffer gas. For experiments in oxygen the lamps were turned off during the period the cell was charged with gases, in order to avoid the buildup of ozone, which suppresses the photolytic decay by reoxidizing the products to form N_2O_5.

The optical density at 8.028 μm was followed as a function of time using the 12-bit A/D and the Fabritek instrument computer. Light intensity was constant or varied slowly in most cases and was recorded

by hand. Linear least squares fits to the slope of semilog plots of $A_o/A(t)$ vs. time yield the photodecomposition rate constant. If the intensity of the photolysis lamps changes significantly during a run, the plot of $\ln[A_o/A(t)]$ was corrected point by point by multiplication by $I_{final}/\int_{x=0}^{x=t} I(x)dx$, for which the integrals were obtained numerically.

The photolytic rate constants were computed from the difference of the total decay rate constants and the measured heterogeneous decay constants. From the optical density and the previously measured IR cross section, the concentration of N_2O_5 was calculated. The quantum yields were calculated by dividing the photolytic rate constant by the product of the UV cross section of N_2O_5 at 254 nm and the absolute light intensity. The sources of these values will be discussed later.

The results are presented in Table 4. The runs were characterized by linear semilog plots in the nitrogen buffered case, but showed pronounced negative curvature with oxygen as the buffer gas. For the oxygen runs, the limiting initial slope was calculated, resulting in much larger error, since the photolytic lamp intensity changed rapidly at the outset of the oxygen runs.

D. CONSTANT INTENSITY PHOTOLYSIS OF FLOWING SYSTEMS

A second set of photolysis experiments concerned N_2O_5, NO_2 and HNO_3 in a flow system at 101 kPa (1 atmosphere). The concentrations of these species were monitored with and without the presence of UV light. Again the experiments were conducted in both oxygen and nitrogen in order to test for differentiation of the mechanism if oxygen atoms are produced

TABLE FOUR

[N2O5]	[N2]	[O2]	PHI
252.0 K			
7.87E+14	0.00E-01	4.17E+16	0.56
6.52E+14	0.00E-01	3.70E+17	0.53
8.80E+14	0.00E-01	3.52E+18	0.23
7.83E+14	0.00E-01	2.45E+19	0.19
1.03E+14	0.00E-01	0.00E-01	0.71
5.47E+14	0.00E-01	0.00E-01	0.62
6.94E+14	0.00E-01	0.00E-01	0.61
7.36E+14	0.00E-01	0.00E-01	0.56
2.86E+13	1.54E+15	0.00E-01	1.14
3.29E+13	1.54E+15	0.00E-01	0.89
6.90E+13	1.54E+15	0.00E-01	0.87
1.38E+14	1.54E+15	0.00E-01	0.79
1.63E+14	1.54E+15	0.00E-01	0.75
3.30E+14	1.54E+15	0.00E-01	0.65
5.98E+14	7.04E+15	0.00E-01	0.40
6.11E+14	5.89E+13	0.00E-01	0.60
6.72E+14	1.75E+16	0.00E-01	0.78
6.88E+14	7.96E+13	0.00E-01	0.82
6.93E+14	3.99E+16	0.00E-01	0.53
7.06E+14	1.33E+16	0.00E-01	0.65
7.58E+14	1.54E+15	0.00E-01	0.50
7.80E+14	3.51E+17	0.00E-01	0.46
1.52E+15	1.54E+15	0.00E-01	0.48
9.23E+14	3.50E+18	0.00E-01	0.38
1.04E+15	2.45E+19	0.00E-01	0.24
273.0 K			
9.04E+14	0.00E-01	3.40E+18	0.36
9.79E+14	0.00E-01	1.02E+19	0.17
9.79E+14	0.00E-01	2.50E+19	0.05
6.99E+14	3.72E+16	0.00E-01	0.86
7.87E+14	3.72E+16	0.00E-01	0.82
7.31E+14	4.14E+16	0.00E-01	0.77
8.31E+14	3.60E+17	0.00E-01	0.84
1.00E+15	3.46E+18	0.00E-01	0.74
7.80E+14	1.02E+19	0.00E-01	0.61
9.12E+14	2.45E+19	0.00E-01	0.57
7.26E+14	2.50E+19	0.00E-01	0.79

[N2O5]	[N2]	[O2]	PHI
295.0 K			
8.01E+14	0.00E-01	2.45E+19	0.23
2.35E+13	0.00E-01	2.45E+19	0.24
8.01E+14	2.45E+19	0.00E-01	0.50
1.58E+15	2.45E+19	0.00E-01	0.60

in the primary photolytic step.

Concentrations were measured at 6.26 μm for NO_2, 7.6 μm for HNO_3 and 8.028 μm for N_2O_5 in the usual way. Light intensity was monitored with a photodiode. Table 5 includes the steady state concentrations observed. Figure 16 is a plot of the approach to photochemical equilibrium of N_2O_5 in three sets of experiments in nitrogen and oxygen after a steady flow had been established. Since the lamps increase in intensity as they warm, the abscissa has been adjusted to units of constant illumination by numerically integrating the product of the photon flux and time. The integral is then expressed as an adjusted time, obtained by dividing it by the maximum(final) intensity. All runs were collected at 268 K.

E. MODULATION EXPERIMENTS

The modulation experiments provide a general test of our understanding of the complete photochemical mechanism. The experimental observations of the modulation parameters are compared to predictions of phase angles and modulation amplitudes based on a detailed computer model to identify the model they most closely resemble. By altering the experimental conditions of temperature and pressure, correspondence of the results with a particular hypothesis can be well established.

Measurements were made in a flowing system at flashing frequencies of 0.306 Hz. The modulation amplitudes of stable reactants and products are generally inversely proportional to the flashing frequency, and in these experiments signals could not be detected at higher frequencies. Two temperatures, 268 and 295 K, and three pressures, 1.72,

TABLE FIVE

	M	N_2O_5	NO_2	HNO_3
A				
Dark	N_2	1.00E15	---	---
Light		5.10E14	---	---
Dark	O_2	1.05E15	---	---
Light		8.40E14	---	---
B				
Dark	N_2	9.18E14	1.44E15	6.12E14
Light		3.33E14	2.60E15	4.19E14
Dark	O_2	8.47E14	4.00E13	1.60E14
Light		6.95E14	3.26E14	1.70E14
C				
Dark	N_2	6.36E14	7.20E13	1.90E14
Light		3.85E14	5.53E14	1.63E14
Dark	O_2	6.64E14	6.47E13	3.7E14
Light		5.6214	---	---

Units of molecule cm^{-3}.

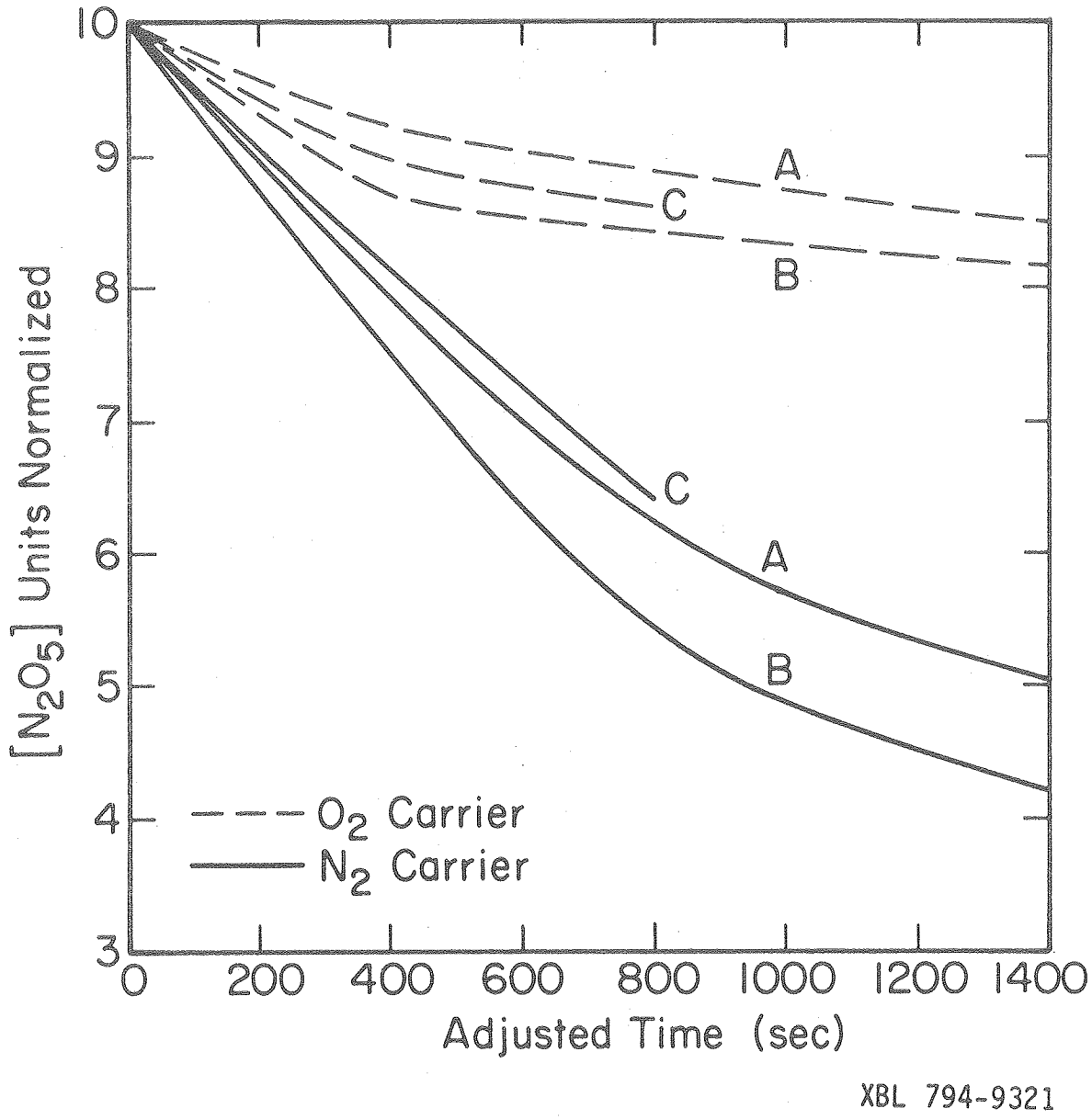

Figure 16. Approach to photochemical/flow steady state.

6.67 and 101 kPa, were studied, using both nitrogen and oxygen as carrier gases. N_2O_5 modulation was observed at 8.028 μm, NO_2 at 6.25 μm. Observations at 6.9 μm, where no species absorb, showed no phase coherence, showing that the observed modulation signals were of chemical origin.

Signals were typically averaged for 30 minutes to an hour, resulting in standard deviations of about 50% for the small amplitudes observed. Precision was somewhat better for cases of larger amplitudes. Phase angles are to within 5°. The results are listed in Table 6. The phase angles for N_2O_5 fall in the first quadrant, indicative of species being photolyzed, while NO_2 appears at -90°, showing product behavior. The 180° phase difference confirms the reactant-product relationship.

F. ACTINOMETRY

Calculation of photolysis quantum yields requires knowledge of the absolute light intensity at the active wavelengths. As noted previously, the germicidal lamps are line sources which emit light at various wavelengths between 254 nm and the IR. The absorption spectrum of N_2O_5, to be discussed in section IV.B.1, is such that it absorbs only the desired 254 nm line. NO_2, O_3 and to a small extent NO_3 however absorb many of the lines present. The absorption coefficient of NO_3 at 436 nm is small,[27] and the contribution of its photolysis to the chemical mechanism is estimated to be negligible. The cross section of the Chappius band of ozone is nearly 10^4 smaller than its maximum cross section in the Hartley region[38] so that only its absorption at 254 nm need be considered.

NO_2 absorbs the 254, 313, 366, 405 and to a very small extent the 436 nm light with decomposition to NO + O. The chlorine lamp filters

TABLE SIX

O_2 Results

	N_2O_5[a]	NO_2[a]	M[b]	$\phi(N_2O_5)$°	ΔI/I	$\phi(NO_2)$°	ΔI/I
295	3.5	1.1	2.45	94 ± 5	(5±2)E-4	-84 ± 10	(3.5±1)E-4
267	6.0	1.1	2.75	---	---	-91 ± 3	(4±1)E-4
267	9.0	---	2.75	89 ± 5	(2.0±0.6)E-4	---	---

N_2 Results

295	1.9	---	2.45	60 ± 15	(1.2±0.5)E-4	---	---
267	6.0	---	0.18	89 ± 5	(2.0±0.6)E-4	---	---
267	6.0	---	0.055	83 ± 8	(3 ± 1)E-4	---	---

[a]Units of 10^{14} molecules cm^{-3}.

[b]Units of 10^{19} molecules cm^{-3}.

reduce the two near UV lines, but pass the 405 nm light, for which the quantum yield for NO_2 destruction is about 0.4.[31] Harker[39] has measured the overall quantum yield for NO_2 disappearance under illumination of wave lengths less than 400 nm at atmospheric pressure and obtained a value of 1.64. In the present work, the photodecomposition rate constant.

$$j_{NO_2} = \int d\lambda\ I(\lambda)\ \sigma(\lambda)\ \phi(\lambda), \tag{47}$$

was measured as the first order disappearance of NO_2 under photolysis in an atmosphere of nitrogen. The empirical rate constant obtained, 2.8×10^{-4} sec^{-1}, was then divided by the overall quantum yield of 1.64, to obtain the j-value of the primary step of 1.7×10^{-4} sec^{-1}. The calculated j-value at 254 nm is 1.4×10^{-4}, so that the active absorption of higher lines has been reduced to about 20% of the total.

The intensity of the 254 nm line was measured by observing the first order decay of hydrogen peroxide under illumination. The UV spectrum of H_2O_2 has been measured by Holt[40] and recently by Molina,[41] and Lin and DeMore,[42] who agree on a cross section of 7.6×10^{-20} cm^2/molecule at 253.7 nm. The spectrum of hydrogen peroxide, Fig. 17 is qualitatively similar to that of N_2O_5 and in particular shows little absorption above 300 nm. The overall quantum yield for destruction is two, based on the mechanism

$$\begin{aligned} H_2O_2 + h\nu &\longrightarrow HO + HO \\ HO + H_2O_2 &\longrightarrow H_2O + HOO \\ HOO + HOO &\longrightarrow H_2O_2 + O_2 \\ \text{net: } 2H_2O_2 + h\nu &\longrightarrow 2H_2O + O_2. \end{aligned} \tag{48}$$

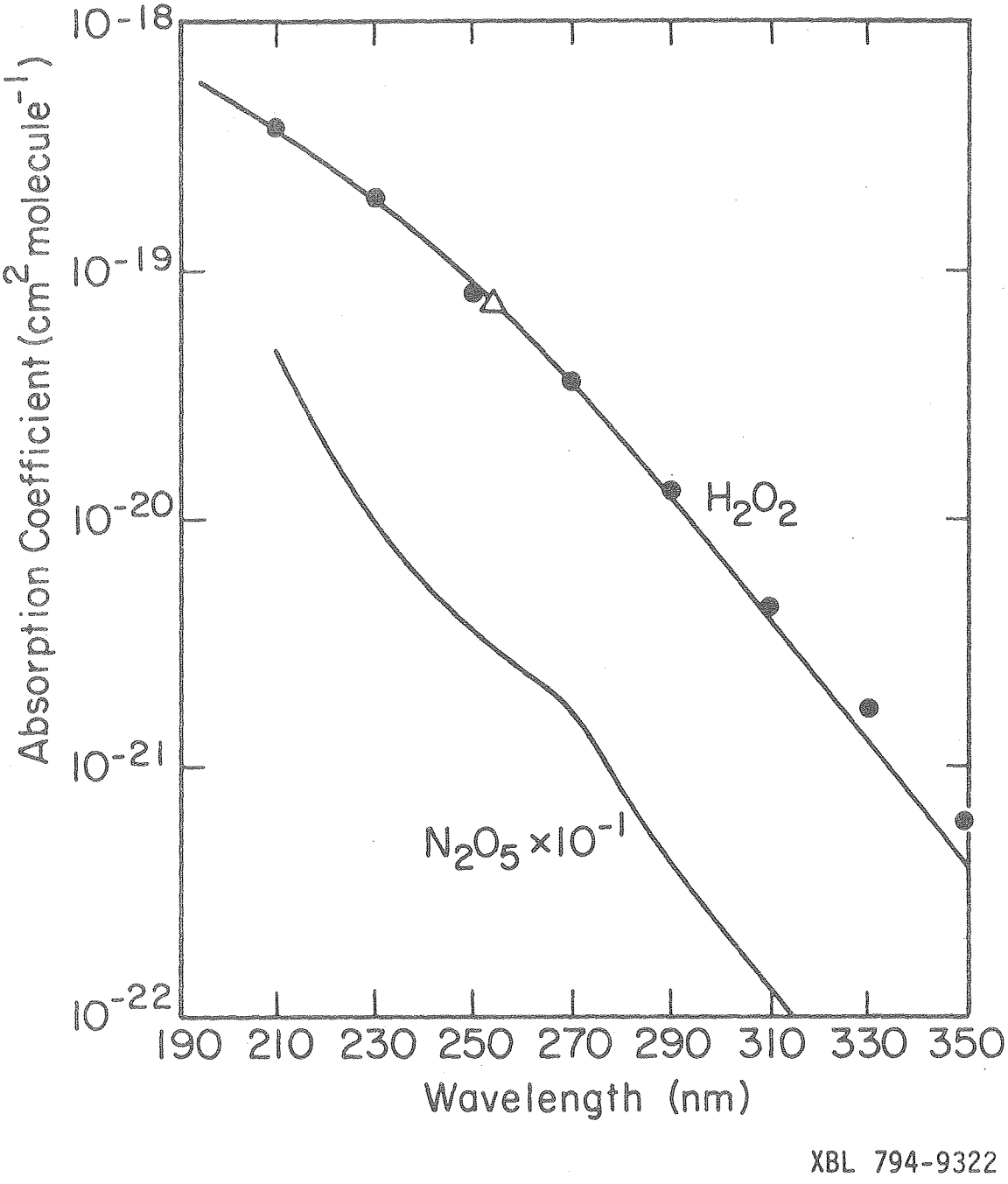

Figure 17. UV absorption spectrum of hydrogen peroxide (H_2O_2).

The photolysis step is rate-determining so the overall reaction is the first order disappearance of H_2O_2.

Actinometry runs were performed at 295 K with concentrations of H_2O_2 on the order of 3×10^{15} molecules/cm^3, corresponding to optical densities of less than 0.25. Gas samples of H_2O_2 were expanded from a 5.4 l bulb into the cell, in order to avoid any possibility of condensation inside the cell, which, when it occurred, caused severe degradation of the gold surface mirrors. Time was allowed before a run commenced for stabilization of the lamp output, complete dispersal of reactant and establishment of the HOO steady state. Lamp intensity was continuously monitored by the UV100B photodiode, so that the photodiode output could be calibrated in terms of absolute intensity. H_2O_2 absorbance was monitored at 6.155 μm and the photocomposition rate was taken as the difference of the total observed rate and the heterogeneous loss rate, which was measured to be about 15% of the total decay rate. Additional experiments at 6.26 μm gave the same result.

The lamp intensity was

$$I(T) = (1.99\text{-}0.0035(295\text{-}T) \pm 0.2) \times 10^{14} \quad (49)$$

photons/cm^2·sec·mV of UV100B output.

The temperature dependence in Eq. (49) arises from the temperature dependence of the responsivity of the photodiode. Photon flux at a lamp wall temperature of 330 K, typical of a room temperature experiment, was about 8.5×10^{15} photons/cm^2·sec in the cell. With the cell held at lower temperatures, the wall temperature and lamp output decreased, to 6×10^{15} at 273 K and 3×10^{15} at 252 K.

IV. RESULTS AND DISCUSSION

A. THERMAL DECOMPOSITION

Modern theories of unimolecular reactions rest upon the mechanism proposed by Lindemann[44] and Hinshelwood.[45] Applied to the case of N_2O_5, the mechanism

$$\begin{aligned} N_2O_5 + M &\xrightarrow{a_i} N_2O_{5i}^* + M \\ N_2O_{5i}^* + M &\xrightarrow{b} N_2O_5 + M \\ N_2O_{5i}^* &\xrightarrow{c_i} NO_2 + NO_3 \end{aligned} \qquad (50)$$

postulates a finite lifetime before molecules with sufficient excitation react or decompose. This allows the excited molecules to be deactivated by collision and results in the prediction of a transition from first to second order as the pressure decreases. At sufficiently low pressures, all molecules with more than the critical energy react before the possibility of a deactivating collision. In this case step (a) is rate-determining and the first order rate constant, which is the rate constant of activation by collision, is proportional to the concentration of M. In this regime, the decomposition is then characterized by a second order rate constant k_o' and the rate of decomposition is $k_o'[N_2O_5][M]$.

At high pressures, activation and deactivation occur much more rapidly than step (c), decomposition. If the deactivation rate from a particular state above the energy threshold, $b[N_2O_{5i}^*][M]$, is much faster than the production of products, $c_i[N_2O_{5i}^*]$, an effective equilibrium distribution of molecules with energy above the threshold is maintained. Step (c) becomes rate-determining and the process becomes strictly first order.

The pressure range over which this transition from first to second order behaviour occurs is usually several orders of magnitude. In the case of N_2O_5 in nitrogen, a plot of k_{uni} vs. [M] is linear within experimental error for pressures less than 2×10^{16} molecules/cm^3. Fig. 18 a and b are plots of the three substantial sets of data obtained in this pressure regime. The slopes of these lines, obtained by linear least squares regression, are the limiting low pressure second order rate constants, k_o':

$$\begin{aligned} k_o'(307\ K) &= (1.72 \pm 0.04) \times 10^{-19} cm^3/mol \cdot sec \\ k_o'(295\ K) &= (6.0 \pm 0.4) \times 10^{-20} \\ k_o'(268\ K) &= (1.0 \pm 0.6) \times 10^{-21}. \end{aligned} \tag{51}$$

The intercepts obtained

$$\begin{aligned} b(307\ K) &= (-1 \pm 14 \times 10^{-6}\ sec^{-1} \\ b(285\ K) &= (9 \pm 27) \times 10^{-6} \\ b(268\ K) &- (-7 \pm 81) \times 10^{-6} \end{aligned} \tag{52}$$

are all zero within one standard deviation, indicating that the low pressure regime has indeed been reached and that there are no residual heterogeneous contributions to the reaction rate.

These second-order rate constants are plotted as circles in Fig. 19 along with limiting second order values (+) derived by a multi-parameter non-linear least squares fit to all the data which will be described below. The triangles in Fig. 19 are values taken from older work[7,8] at higher temperatures. The least squares fit to the present data gives an Arrhenius expression for k_o' of

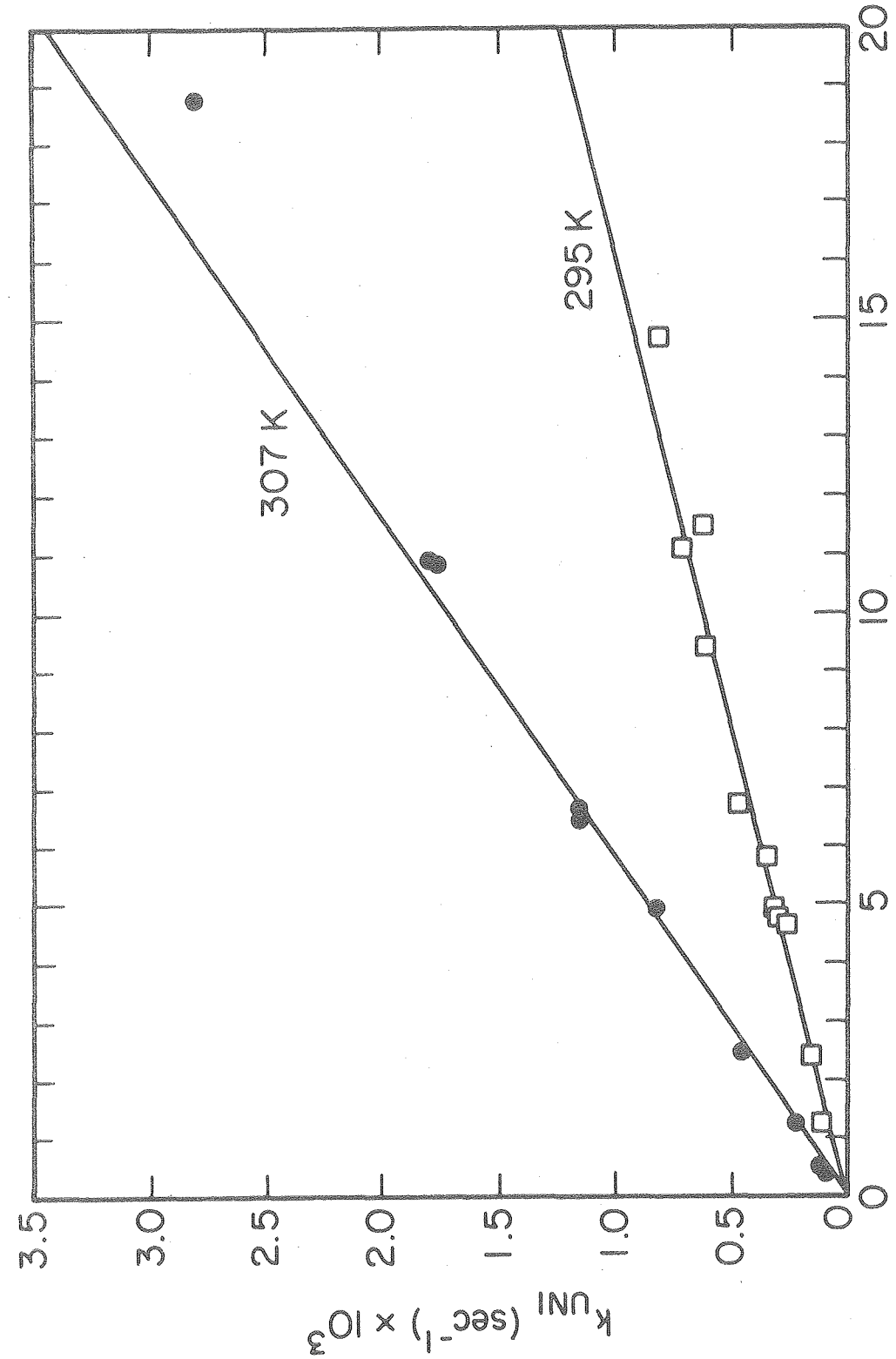

XBL 794-9329

Figure 18a. Low pressure decomposition constants at 307 and 295 K.

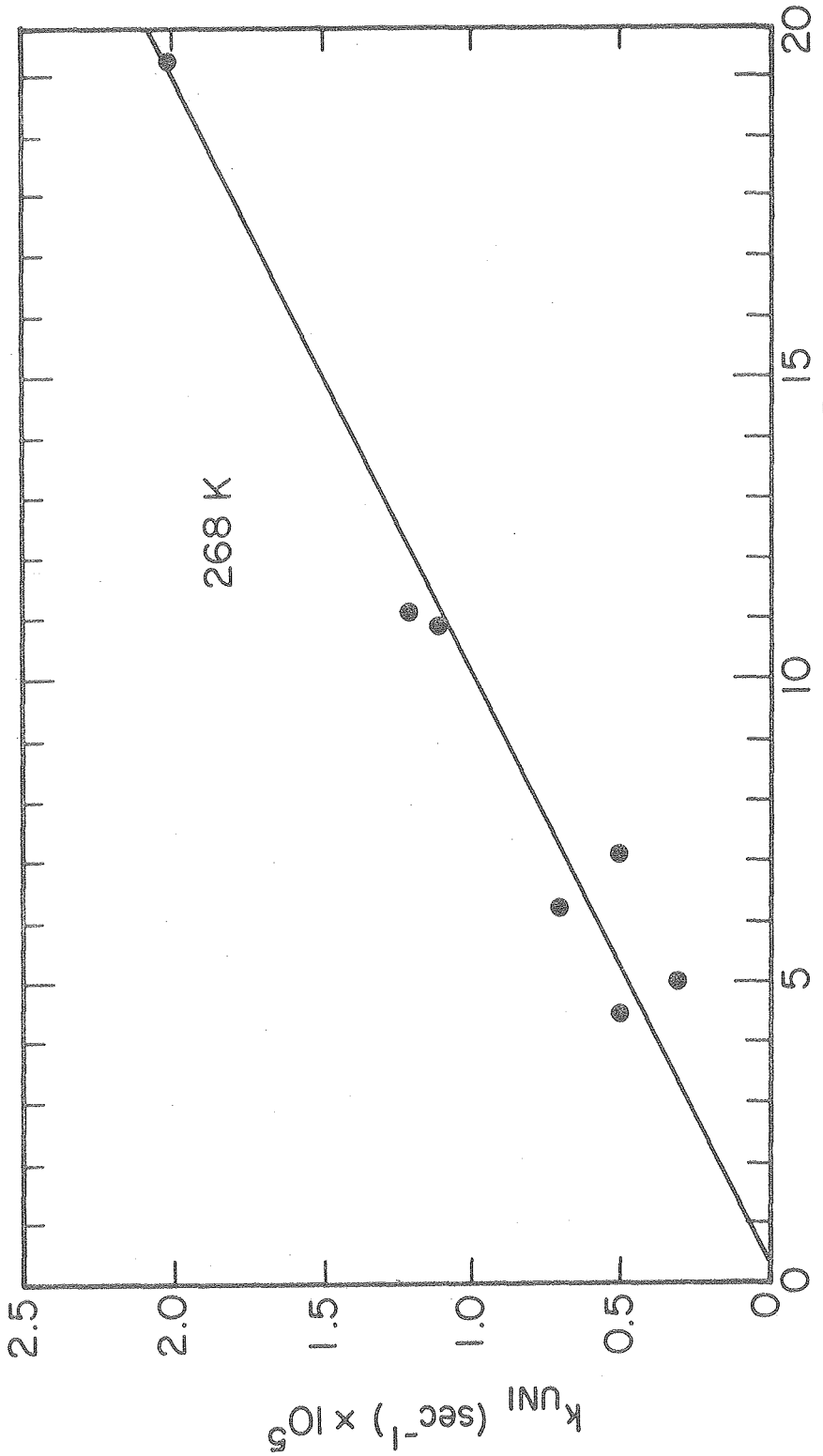

XBL 794-9330

Figure 18b. Low pressure decomposition constants at 268 K.

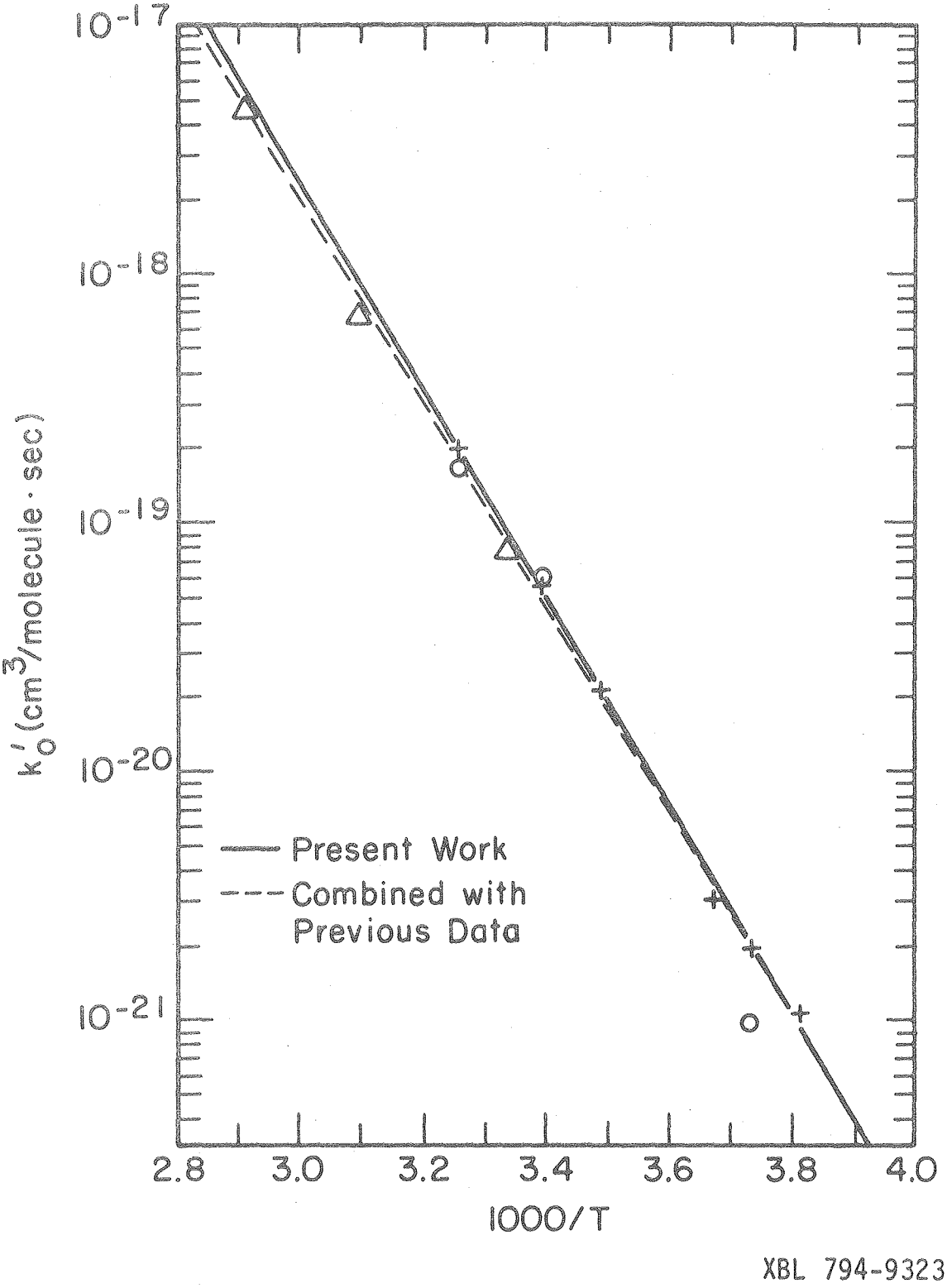

Figure 19. Arrhenius plot of second order low pressure rate constants.

$$k_o' = 8.05 \times 10^{-6} \exp(-9630 \pm 400)/T \text{ cm}^3 \text{ molecules}^{-1}\text{sec}^{-1}. \quad (53)$$

This value is in good agreement with the previously determined value of $6.5 \times 10^{-6} \exp(-9640/T)$. Combining the data gives a value of $\exp(-12.0-9570/T\pm0.7)$ cm^3 molecules^{-1}sec^{-1}. The difference in A-factor of the two independent values is equivalent to a total shift in temperature of 2 K by either or both data sets, or could be explained in terms of curvature of the Arrhenius plot, which will be discussed later.

From the Lindemann-Hinshelwood expression

$$1/k = 1/k_\infty + 1/k_o'[M] \quad (54)$$

it is evident that for the two state model, a plot of 1/k vs 1/[M] will be a line of slope $1/k_o'$ and intercept $1/k_\infty$.[46] Although the spread of states above the critical energy in real molecules produces curvature in such a plot, k_∞ is still obtained from the limiting intercept. The three sets of data for which values at [M]>7 $\times 10^{18}$ molecules cm^{-3} are available are plotted in this fashion in Fig. 20. The first order rate constants in the high pressure limit are

$$\begin{aligned} k_\infty(272.5 \text{ K}) &= (1.93 \pm 0.12) \times 10^{-3}\text{sec}^{-1} \\ k_\infty(268 \text{ K}) &= (7.9 \pm 0.4) \times 10^{-4} \\ k_\infty(262 \text{ K}) &= (2.99 \pm 0.09) \times 10^{-4} \end{aligned} \quad (55)$$

where the error limits are the standard deviation of the least squares fit. The inverses of the slopes of the lines

$$\begin{aligned} 1/m\ (272.5 \text{ K}) &= 6 \times 10^{-24} \text{cm}^3 \text{ molecules}^{-1} \text{ sec}^{-1} \\ 1/m(268 \text{ K}) &= 2 \times 10^{-24} \\ 1/m(262 \text{ K}) &= 7 \times 10^{-25} \end{aligned} \quad (56)$$

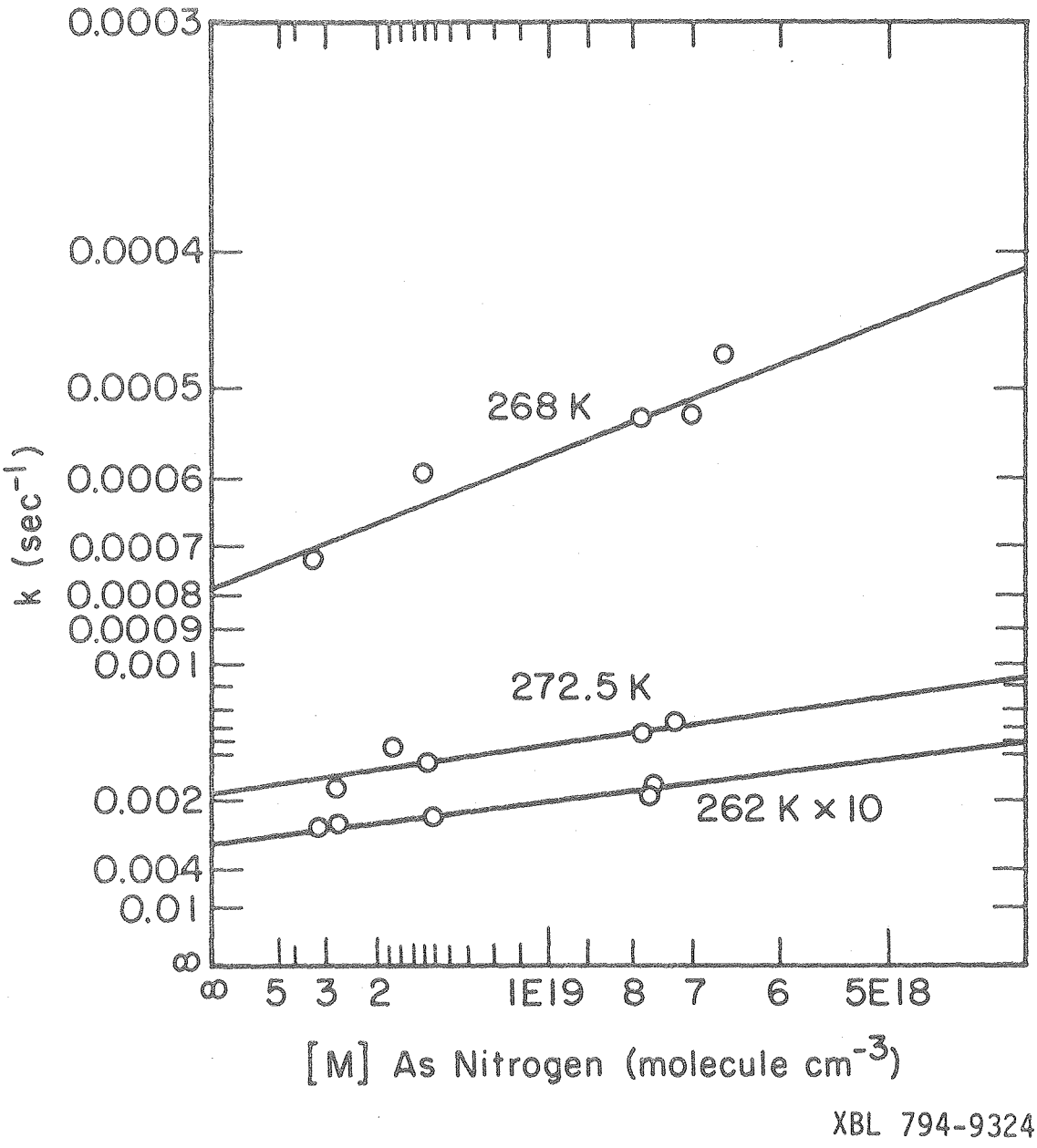

Figure 20. High pressure decomposition constants.

properly represent (extreme) lower limits to the second-order rate constants, $k_o'(T)$.

The only previous high pressure limiting value is that of Mills and Johnston[6], who extrapolated data taken at 300 K near and above 101 kPa, of N_2O_5 decomposition in nitrogen to give a limiting high pressure value of

$$k_\infty(300\ K) = 0.29\ sec^{-1} \quad . \tag{57}$$

The value of 0.0088 sec^{-1} obtained in the same way at 273 K was later shown to be heterogeneously catalyzed.[7,47] In order to allow examination of a very wide range of pressures, the work of Mills was carried out in three separate apparati, one for the low pressure region, one for intermediate pressures to an atmosphere and one for the measurements at pressures greater than an atmosphere. The detection technique in all three cases was optical observation of the visible absorption of the product NO_2. In the low and intermediate pressure experiments N_2O_5 concentrations as a function of time were calculated by subtracting a third of the corrected NO_2 concentration measured from the initial N_2O_5 concentration obtained manometrically. This proved unfeasible in the high pressure cell and the initial N_2O_5 concentration was calculated from the NO_2 present after the reaction had proceeded to completion.

Although the presence of heterogeneously catalyzed production of NO_2 from N_2O_5 can be detected as a non-zero intercept in the plot of k_{uni} vs [M] in the low pressure limit when detection is by observation of NO_2, this cannot be tested at higher pressures. In addition, the presence of heterogeneous processes producing HNO_3, noted in the present work and previous studies,[23] cannot be observed. The effect

of consideration of this process on the result of Mills's experiment is dependent on the method of data reduction. In the low and medium pressure experiments, a derivation of the empirical rate constant, based on the mechanism

$$\begin{aligned} N_2O_5 &\xrightarrow{A} \underset{f}{NO_2} + NO_3 \\ NO + NO_3 &\longrightarrow 2\ NO_2 \\ N_2O_5 &\xrightarrow{w} HNO_3, \end{aligned} \tag{58}$$

gives the expression

$$k_{uni}(\text{observed}) = \frac{A\ e^{-(A+w)t}}{1 + \dfrac{[HNO_3]_o}{[N_2O_5]_o} - \dfrac{A}{A+w}(1-e^{-(A+w)t})} \quad . \tag{59}$$

The initial slope of the logarithmic plot of $[N_2O_5]/[N_2O_5]_o$ would be $A/(1+[HNO_3]_o/[N_2O_5]_o)$ and the first order plot would be curved upward. By careful technique, the ratio of initial nitric acid in the dinitrogen pentoxide can be held to a few percent, so that a fairly good value for the decomposition rate constant A is obtained. In the high pressure experiments, for which the initial $[N_2O_5]_o$ was inferred from the final value for $[NO_2]$, the expression derived for the empirical rate constant is

$$k_{uni}(\text{observed}) = A + w \quad . \tag{60}$$

The faster rate constants obtained by Mills, those in the high pressure apparatus and a few in the intermediate pressure region, also appear related to high NO/N_2O_5 ratios, perhaps indicating complication by the heterogeneous NO/HNO_3 reaction. For these reasons, the values obtained by Mills in the intermediate pressure apparatus have been

replotted, corrected to equivalent nitrogen gas density, over the same range as Fig. 5 in Ref. 6, $[M] > 7 \times 10^{18}$ molecules cm^{-3}. A least squares fit to these points, shown in Fig. 21, taken mostly in CO_2, yields an intercept of 0.125 sec^{-1} with a standard deviation of 0.012 sec^{-1}. The broken line in Fig. 21 indicates the fit from Fig. 5 in Ref. 6.

This value is included in Fig. 22 as a square, along with the three present values. The value originally determined by Mills is indicated by the triangle. The least squares fit to the present work and the revised 300 K point is

$$k_\infty(T) = 1.78 \times 10^{17} \exp(-12540 \pm 130)/T \qquad (61)$$

where the error is the standard deviation of the fit. The corresponding activation energy is 104.3 kJ/mole, larger than Mills's estimate of 88±9 kJ/mole.

In order to develop a convenient representation for data obtained between the pressure limits in the so-called fall-off region, an interpolation formula with a theoretical basis is desirable. If the steady-state assumption for $[N_2O_{5i}^*]$ is made in mechanism (50), the familiar result is derived:

$$k_{uni} = \sum_i \frac{a_i c_i [M]}{c_i + b[M]} \quad , \qquad (62)$$

in which deactivation, b, is considered independent of the energy. The limiting expressions are

$$\lim_{[M]\to 0} k = k_o' = \sum_i a_i [M] \qquad (63)$$

and

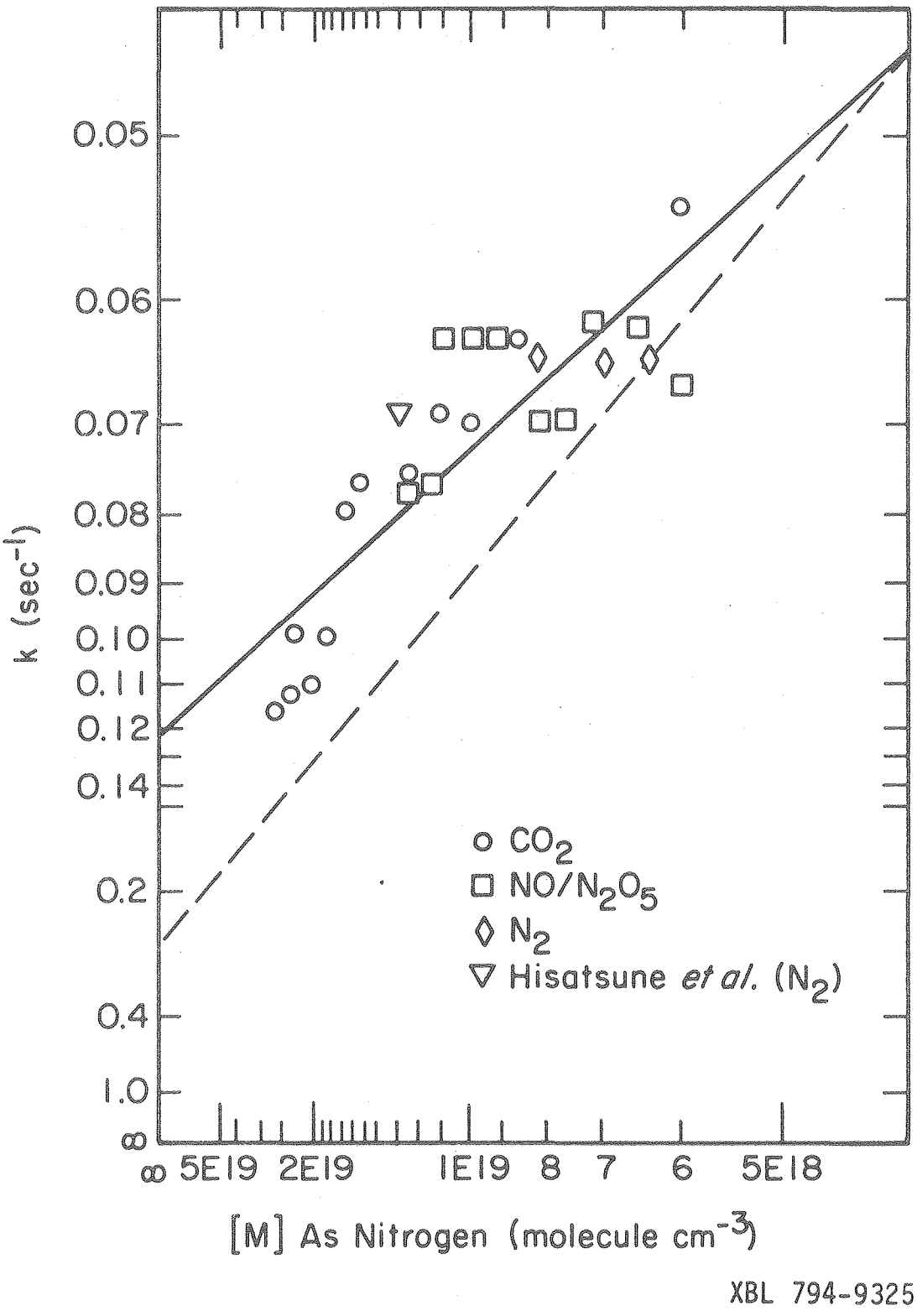

Figure 21. Intermediate pressure decomposition constants of Mills and Johnston.

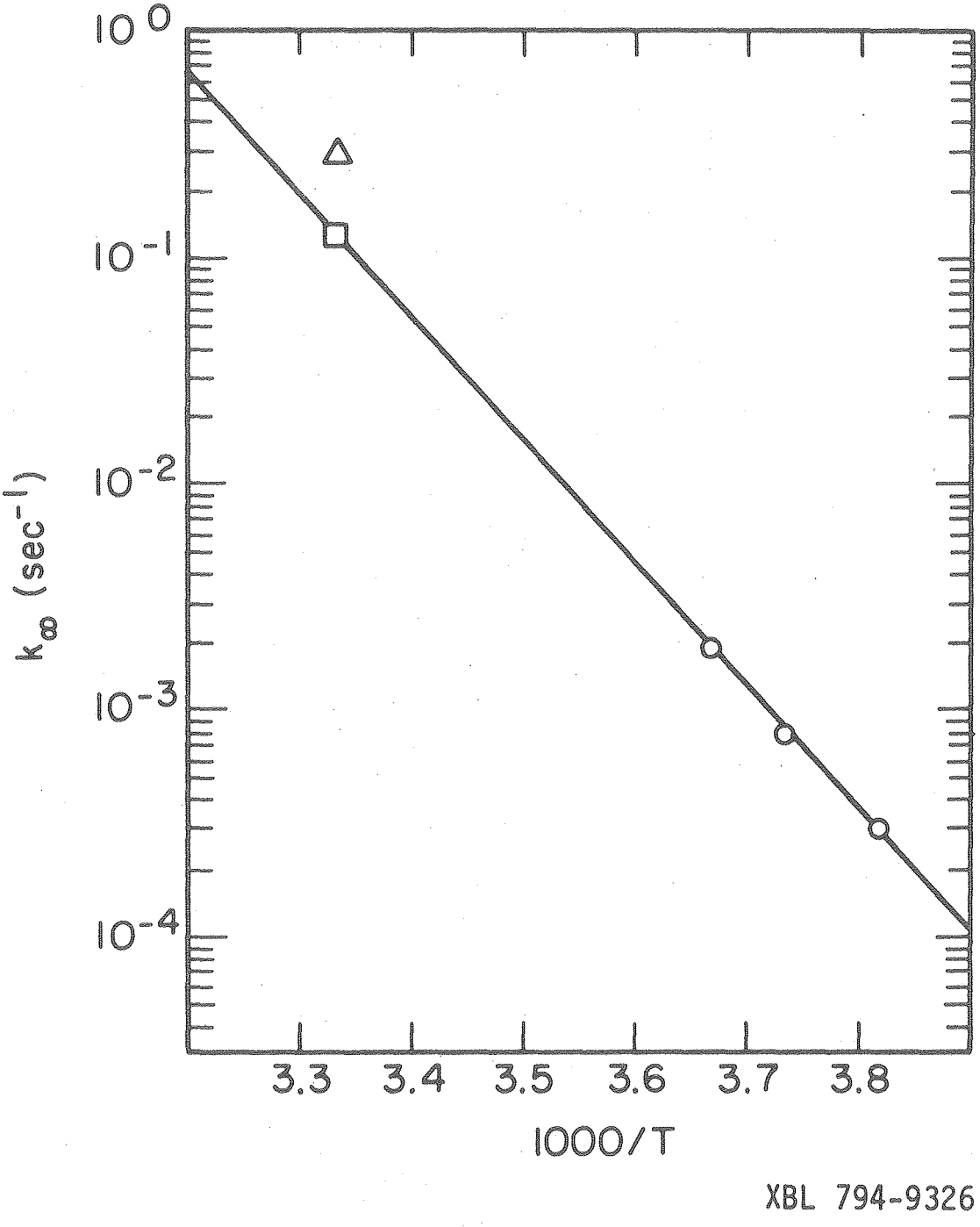

Figure 22. Arrhenius plot of first order constants in the high pressure limit.

$$\lim_{1/[M]\to 0} k = k_\infty = \sum_i a_i c_i / b \tag{64}$$

Johnston and White[13] have derived the general relationships

$$b \left\langle \frac{k_\infty - k}{k/[M]} \right\rangle = \left\langle c_i \right\rangle^T \tag{65}$$

and

$$\frac{1}{b} \left\langle \frac{k_o' - k/[M]}{k} \right\rangle = \left\langle 1/c_i \right\rangle^T \quad , \tag{66}$$

where the T indicates the averages are over the Tolman distribution, the distribution of molecules that react. The population of state i of this distribution is simply the ith term in (62). Clearly if the energy of state i is below the critical energy, the specific rate constant for decomposition, c_i, is zero as is the term in the Tolman distribution.

The physical meanings of the two terms are approximately the average rate constant for decomposition from the reacting states and the average lifetime with respect to decomposition of these states, respectively. In the two-state model, with one ground state and one state with sufficient energy to react, each average is necessarily the inverse of the other, the distributions collapse and the product of the two terms is

$$J = \left(\frac{k_\infty - k}{k}\right)\left(\frac{k_o'[M] - k'}{k'}\right) = 1. \tag{67}$$

With many vibrational and rotational states above and below the critical energy, the average rate constant for decomposition must be larger than the average lifetime and J is restricted to values greater than one.

Since the distribution of energized molecules across the quantum states higher than the critical energy is a function of pressure and temperature (pressure dependence of the non-equilibrium distribution

is the reason for the difference in high and low pressure activation energies), the value of J is also to be expected to vary with these factors. The expression (67) will however be an adequate interpolating function if J is relatively constant near the midrange of pressure $[M] = k_\infty/k_o'$.

The Kassel quantized statistical form of RRK theory[48] provides one way to test this assumption. RRK theory considers an ensemble of weakly interacting harmonic oscillators of a single frequency. The weak interaction allows them to transfer energy without perturbing each other's energy levels. When the m quanta of vibrational energy sufficient to overcome the critical energy reside in a particular distribution, i.e. the reaction coordinate, the reaction is considered to occur. The distribution over states greater than the critical energy and the specific rate constant for reaction from such a state i are given by statistical arguments concerning the number of ways possible to distribute the m+i energy quanta among the s oscillators.

$$p_i = \frac{(m+i+s-1)!(1-e^{-x})^s e^{-mx} e^{-ix}}{(m+i)!(s-1)!} \tag{68}$$

and

$$c_i = D\,\frac{(m+i)!(i+s-1)!}{i!(m+i+s-1)!} \tag{69}$$

$$mx = E_c/kT \quad . \tag{70}$$

D is a proportionality factor with units of sec^{-1}, which is equated to the high pressure A-factor.

The quantities $\langle c_i \rangle$ and $\langle 1/c_i \rangle$ can be evaluated over the Tolman distribution

$$T_i = \frac{bP_i c_i[M]}{b[M]+c_i} \tag{71}$$

to give an expression for J([M])

$$J = 1 + \frac{\sum_{i=0}^{\infty}\sum_{j>i}^{\infty}\left(\prod_{k=1}^{s-1}\frac{(k+i)^2(k+m+j)}{(k+m+i)} + \prod_{k=1}^{s-1}\frac{(k+j)^2(k+m+i)}{(k+m+j)} - \prod_{k=1}^{s-1}2(k+i)(k+j)\right)\frac{e^{-(i+j)/x}}{(b+c_i/[M])(b+c_j/[M])}}{\left(\sum_{i=0}^{\infty}\frac{(i+s-1)!}{i!}\frac{e^{-ix}}{b+c_i/[M]}\right)^2} \tag{72}$$

For this model, as the size of the quanta become large compared to the critical energy, m tends toward one, the distribution approaches a two-state system and J approaches one. If m becomes large the system becomes classical and J becomes large. For the purpose of evaluating J, computation of k'_o, k_∞, and k is numerically easier than evaluation of (72). Fig. 23 shows the result of a calculation of k, plotted as filled circles, using (68), (69) and (70). The collision rate constant has been set at 5.6×10^{-10} cm^3 $molecule^{-1}sec^{-1}$, the number of quanta m to equal the critical energy is 22, setting the energy of a quantum at 396 cm^{-1}. All fifteen oscillators are considered active as is usually assumed in the quantum application of RRK theory. The values of these parameters have been chosen to match most closely the experimental data at 268 K, which are also indicated in the figure plotted as squares. The dotted line is an interpolating function fit to the data in a manner described below.

A non-linear multi-parameter (J, K_∞, k'_o) least squares computer program, listed in Appendix A, was used to fit the complete data set to Eq. (67), which rearranged gives

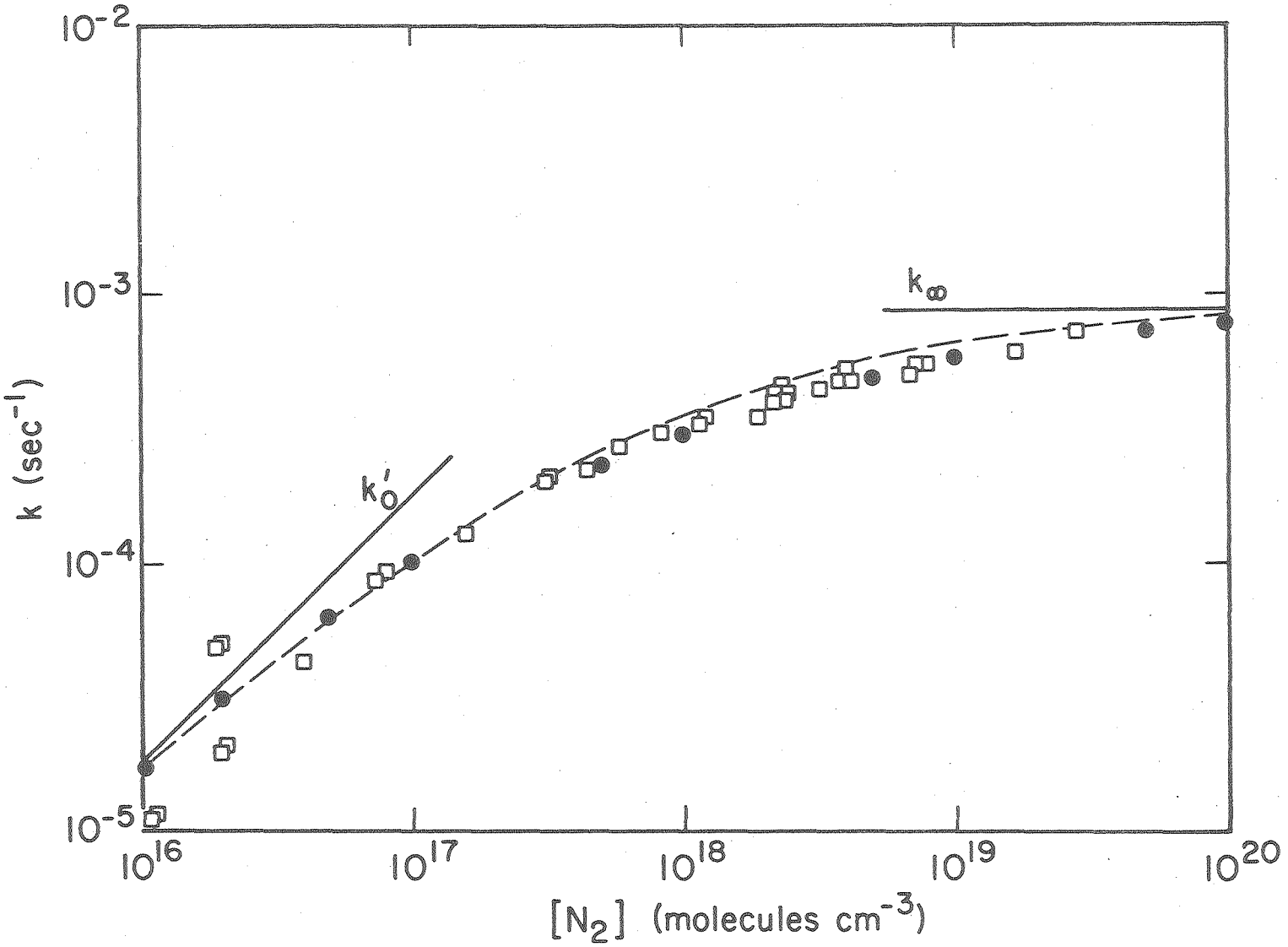

Figure 23. Results of Kassel calculation at 268 K.

$$k = \frac{-\left(k_o'[M]+ k_\infty\right)+ \left((k_o'[M]+k_\infty)^2 + 4(J-1)k_\infty k_o'[M]\right)^{1/2}}{2(J-1)} \quad . \qquad (67a)$$

The fitting parameters listed in Table 7 allow interpolation at each temperature except 287 K, for which not enough data was available. The program seeks a minimum in χ^2, the total error of the fit, on the three-dimensional surface. At higher temperatures for which no high pressure data were available the minimum in χ^2 was very shallow in the (J, k_∞) plane, allowing J and k_∞ to float proportionately. However in each case the best fit to J was on the order of 6.5±1, so a second two-parameter fit at fixed J independent of temperature was made. The values of k_o' thus obtained are the values plotted as + in Fig. 19. The k_∞ values produced by the fitting program are not representative of the true limiting values, but are only used for interpolation. The dotted line in Fig. 23 shows the interpolation function at 268 K.

Previous data[6,7,8] at intermediate pressures have been plotted in Fig. 24 in accompaniment with the interpolated results of the present work. The gas density range covered is $3 \times 10^{16} \leq [M] \leq 3 \times 10^{19}$ molecules cm^{-3}. The temperature range is 262 to 324 K. The A-factors and activation energies are tabulated below with the associated values for the reverse reaction

$$NO_2 + NO_3 \xrightarrow{B[M]} N_2O_5 \quad . \qquad (73)$$

Recently Viggiano et al.[11] have been able to apply their technique of flowing afterglow chemical ionization with mass spectrometric determination to study the thermal decomposition of N_2O_5 in a flowing

TABLE SEVEN

T K	k_o' $cm^3 molecule^{-1} sec^{-1}$	$k_\infty sec^{-1}$	J
307	1.95×10^{-19}	0.060	7.2
295	5.83×10^{-20}	0.031	6.0
272.5	5.31×10^{-21}	2.0×10^{-3}	13.1
268	1.95×10^{21}	7.1×10^{-4}	6.1
262	1.07×10^{-21}	2.55×10^{-4}	6.8

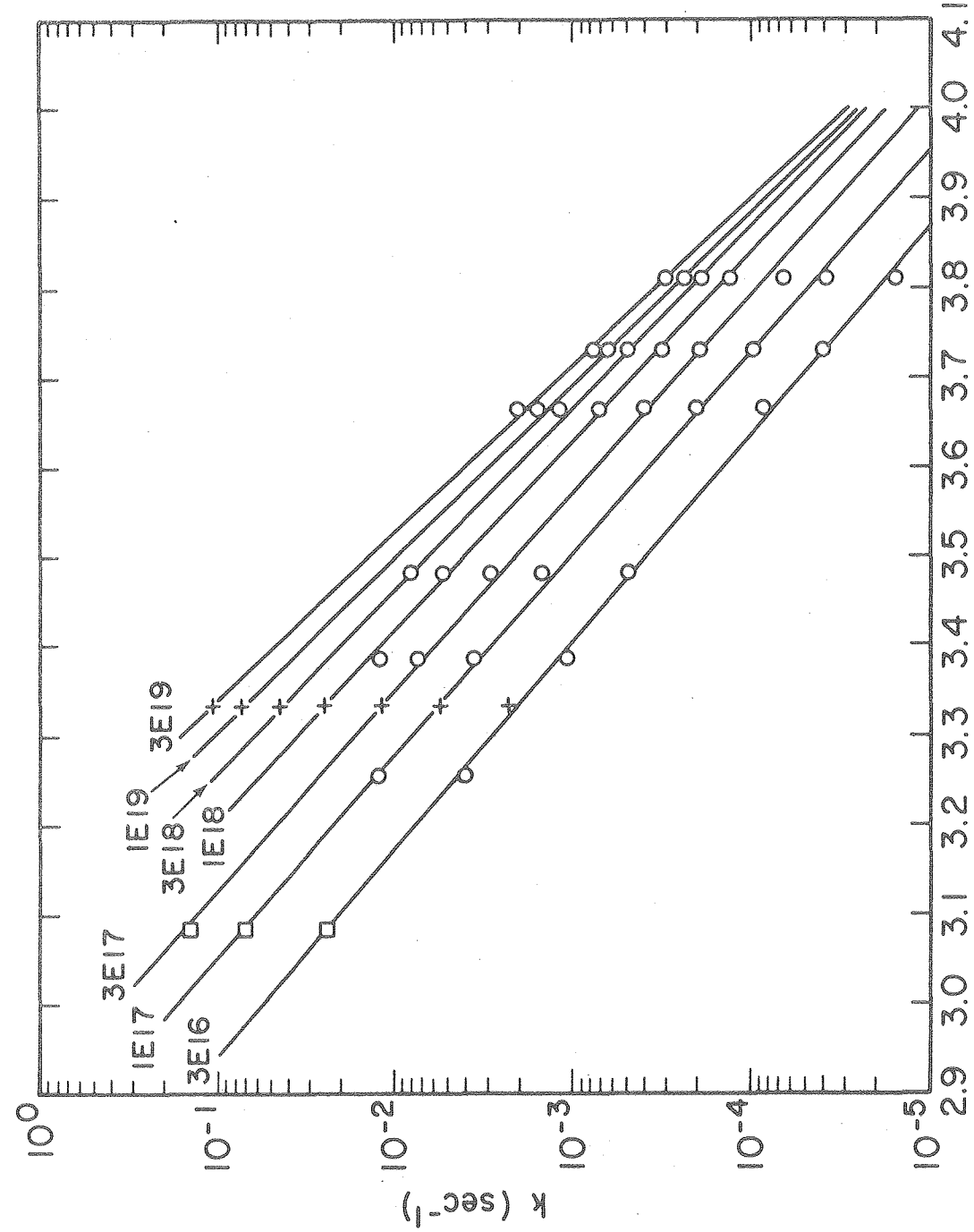

Figure 24. Arrhenius plot of intermediate pressure rate constants.

TABLE EIGHT

N_2[a]	A_f[b]	E_f[c]	A_r[d]	E_r[c]
3×10^{16}	4.9×10^{11}	9940	5.9×10^{-16}	-1240
1×10^{17}	3.6×10^{12}	10230	4.3×10^{-15}	- 950
3×10^{17}	1.78×10^{13}	10480	2.13×10^{-14}	- 700
1×10^{18}	1.64×10^{14}	10920	1.96×10^{-13}	- 260
3×10^{18}	1.24×10^{15}	11360	1.48×10^{-12}	180
1×10^{19}	1.53×10^{16}	11960	1.83×10^{-11}	780
3×10^{19}	9.7×10^{16}	12410	1.16×10^{-10}	1230

a. Units of molecule cm^{-3}.

b. Units of sec^{-1}.

c. Units of K.

d. Units of cm^3 $molecule^{-1}$ sec^{-1}.

system. Their experimental system was restricted to the intermediate pressure range of 1.87 to 47.5 kPa but allowed the variation of temperature to cover 267 to 377 K. Figure 1 includes results of their work at 268 K, including one interpolated point and five points extrapolated downwards from 6 to 28 degrees. These values, obtained in a cell of 735 cm^3 volume, agree closely with the present work within the respective limits of experimental error.

The requirements on experimental data, placed by the need to extrapolate 40 degrees below the 40 to 80 degree experimental temperature range to reach stratospheric conditions are stringent. The present results differ from earlier conclusions[6,7,13] primarily with regard to the high pressure Arrhenius parameters. The high pressure rate constants extrapolated to 220 K differ by nearly a factor of 20 between the present smaller result and the previous value.[6] The present work also shows an earlier onset of the high pressure limit, reflected in the magnitude of J (around 6.5 at 268 K) as opposed to the value of 20 to 30 at 300 K deduced from the earlier results.[13] Part of the discrepancy is resolved if the data of Mills in his high pressure cell are discarded in favor of his intermediate pressure cell results. The revised k_∞ value of 0.125 vs 0.29 sec^{-1} reduces his experimental J values to about 12 or smaller at 300K.

The present high pressure activation energy of 12540 K, and thus the value of $A_\infty = 1.78 \times 10^{17}$ sec^{-1}, are both greater than the previous estimates of 11000 K and 5×10^{14} sec^{-1}.

Many attempts to fit the previous data to various theories of unimolecular decomposition have been made. In each case the high pressure

activation energy is, however, an input parameter, as is the high pressure A-factor in some others. Consequently only the relationship of the predicted pressure dependence to the experimental results can be tested. Johnston[49] applied Kassel theory to the pressure extremes observed by Mills and concluded that no possible combination of active oscillators and quantum size could reproduce the observations. Kassel[50] agreed, but pointed out that the fault lay in the high pressure data, which was inconsistent with any possible distribution based on the data at medium pressures. He was able to fit the remaining data with Kassel theory using all 15 oscillators as active with 25 quanta equalling the estimated critical energy of 35RT. He also showed that a simple model based on constant J=9.90 fit the data fairly well.

Kassel concluded that the shape of the experimental pressure dependence was an insensitive tool for study of the distribution of specific rate constants, C_i, for decomposition from individual quantum states above the critical energy and thus for testing theories of the nature of the distribution. Certainly data would have to cover a wide range of pressure with great precision to study the behavior of J. A function based on a constant value of J has been used to fit the data, but experimental values of J, plotted in Fig. 25, show trends with both pressure and temperature. The Kassel quantum calculation described earlier, which was adjusted to fit the data by variation of b, the collision rate constant, and the other disposable parameters in the theory, predicts a slow increase in J with both pressure and temperature. Figure 25 shows these results at 268 and 300 K. There is a great spread in the experimental values for J, and it is not clear whether the increase

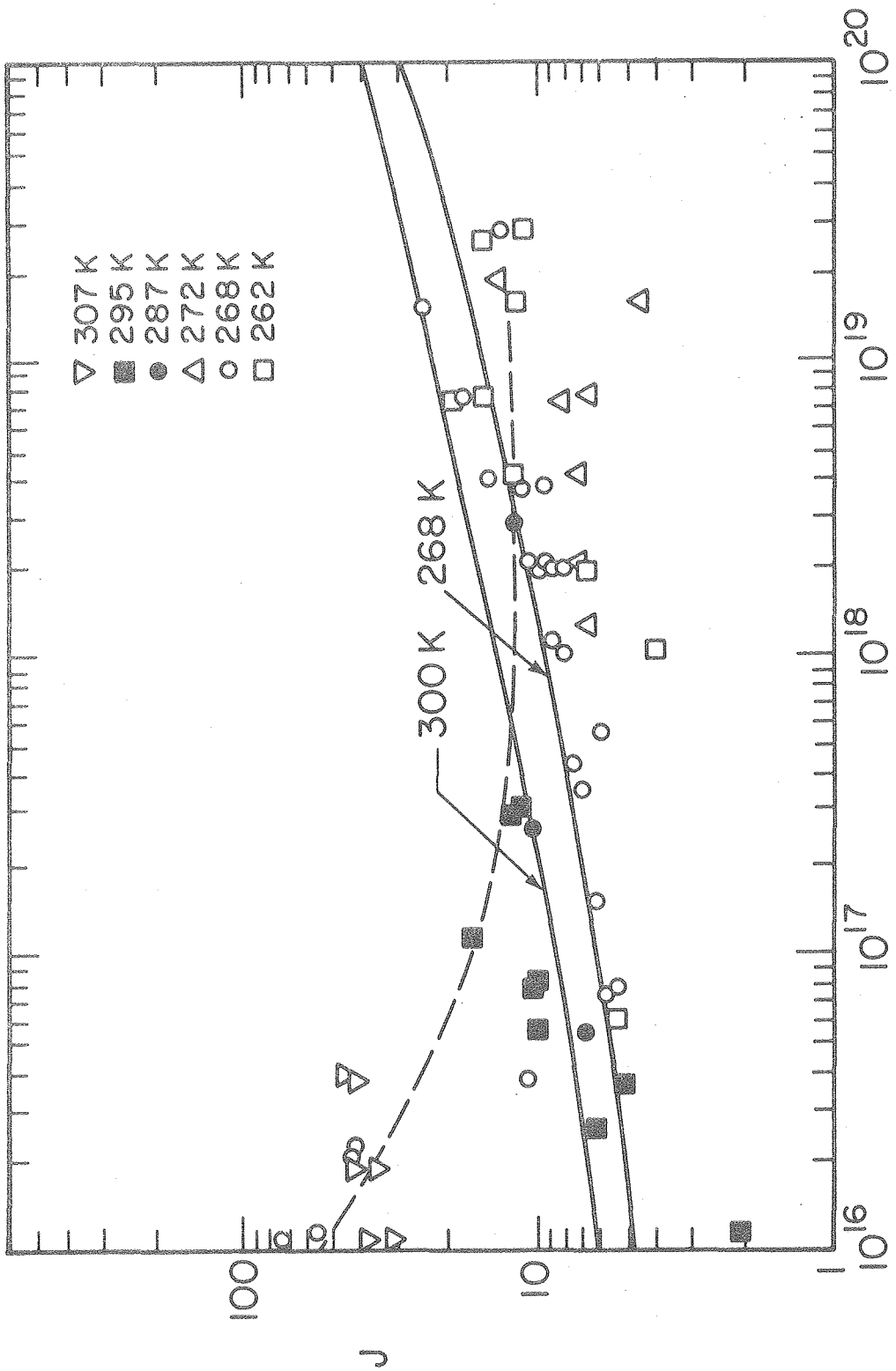

Figure 25. Experimental values of J.

with pressure predicted by RRK theory is observed.

The RRK model of 15 identical harmonic oscillators is not a realistic picture of the spread of frequencies in the actual molecule. An attempt to match the data with Slater's theory, in which only certain vibrations, those of the proper symmetry, are active, has also been made.[51] Although provision is made for a spread of the active oscillators, the agreement with experiment of the pressure at which the rate constant has fallen to 95% of its high pressure value was poor. The restriction of active modes to those of a single symmetry type is probably responsible for the discrepancy, since anharmonicity in general allows energy transfer among all modes.[48]

The most realistic theory of unimolecular reaction processes is the extension by Marcus[48,52] of RRK theory. RRKM retains the statistical nature of the theories proposed by Kassel and by Rice and Ramsperger, but calculates the ad hoc parameter, D, in the RRK expression for the specific rate constant, c_i, using the formalism of transition state theory.

Wieder and Marcus,[53] in further developing RRKM theory, treated the case of N_2O_5. The distribution of energized molecules, determined combinatorially by Kassel, is calculated by evaluating the density of states at energy E from knowledge of the structure and vibration frequencies of the molecule. The specific rate constant for reaction from a state of energy $E>E_c$ is calculated by evaluating the density of states in a particular region of phase space, the transition state, in which a critical configuration has been obtained and a certain amount of energy, the critical energy, has been fixed. The resulting expression for the

unimolecular rate constant depends on knowledge of the high pressure activation energy, the partition functions of the molecule and the density of states of the energized molecule and activated complex as functions of energy,

$$k_{uni} = \frac{\sigma Q_1^+ \exp(-E_c/kT)}{hQ_1Q_2} \int_{E^+=0}^{\infty} \frac{\left\{ \sum_{E_{vr}^+=0}^{E^+} P(E_{vr}^+) \right\} \exp(-E^+/kT)\, dE^+}{1+k_a(E_c+E^+)/b[M]} \tag{74}$$

and

$$k_a(E_c+E^+) = \frac{\sigma Q_1^+}{hQ_1 N^*(E_c+E^+)} \sum_{E_{vr}^+=0}^{E^+} P(E_{vr}^+) \tag{75}$$

where E_c = critical energy

E^+ = energy above the critical energy

σ = symmetry factor

Q_1, Q^+ = partition function of adiabatic modes of molecule, activated complex

Q_2 = partition function for active degrees of freedom of the molecule

$\sum_{E_{vr}^+=0}^{E^+} P(E_{vr}^+)$ = total number of quantum states of activated complex up to E^+

$N^*(E_c+E^+)$ = density of quantum states of molecule at energy (E_c+E^+)

b = collision rate constant.

The structure of the transition state and its vibrational frequencies must be chosen to apply RRKM theory. Wieder and Marcus chose a "loose" transition state, expected to conform to decompositions for which the reverse reaction is the recombination of radical fragments with little activation energy, for their calculations. The model of the activated complex is of a quasidiatomic species in which the "atoms", the NO_2 and NO_3 molecules, are free to rotate. The predicted A-factor at 300 K from this model was about 60 times larger than that estimated by Mills and Johnston and the shape of the pressure dependent curve (Fig. 7 in Ref. 53) was sharper than that observed by Mills. In particular, the predicted pressure at which the rate constant falls to half its high pressure limit, $P_{1/2}$, was a factor of two smaller than the experimental value. If the revised value of 0.125 sec^{-1} is replaced for the old value of 0.29 sec^{-1} the experimental value for $p_{1/2}$ comes into close agreement with the calculation.

Recently Golden and Smith have developed a Gorin-type hindered rotational model for the transition state of simple bond fission reactions with radical products.[54,55,56] The model is similar in concept to the "loose" transition state described above. The free internal rotation allowed by Wieder and Marcus is, however, replaced by hindered internal rotation, in which the moments of inertia of the internal rotors are reduced by a function $\sqrt{1-\eta}$, of the hindrance parameter, η. The physical picture is of a volume of phase space denied to the rotating fragment by the presence of the other fragment. If the distance between the rotating fragments is taken to be the top of the centrifugal barrier

in the potential, this model also explains the negative temperature dependence of the A-factor often observed experimentally,[55] since the position of the centrifugal barrier will decrease with temperature, thus increasing the hindrance.

Using van der Waals radii for atoms, a simple excluded volume picture indicates hindrances around 50%. In application to HNO_3 and HO_2NO_2, larger values of the hindrance parameter, around 95%, were necessary to reproduce the observed A-factors. The program has been applied to the present data set, with vibrational frequencies and moments of inertia taken from the JANAF tables. The vibrational frequencies in the transition state were taken to be those of the free NO_2 and NO_3 fragments. The collision efficiency of nitrogen was taken to be 0.3 as suggested by other results.[55]

The result[57] obtained with a critical energy of 11000 K at 300 K and with the hindrance of 99.5% necessary to fit the high pressure limits of the present data set is also in good agreement in the low and intermediate pressure regions. The shape of the fall-off curve is similar to that of the experimental data. The predicted pressure dependence of J at 300 K is included in Fig. 25 as the broken line. In contrast to the result of Kassel theory and perhaps in better agreement with the experimental observations, J is larger at low pressure and is fairly constant throughout the intermediate pressures for which stratospheric rate constant extrapolations are made. This behavior of J was also observed in the study of the isomerization of methyl isocyanide by B. S. Rabinovitch.[46,58] Little temperature dependence of the value of J between 300 and 268 K is predicted by the RRKM model.

Raising the critical energy used in the calculation to 12240 K produces agreement in the high pressure limit with internal rotor hindrances of around 40%, giving the higher A-factor of 1.6×10^{17} sec^{-1}. The fit to the data of the calculated rate constant is, however, much poorer. Figure 26 shows the fit to the data at 268 K for the two calculations. The density of states in the energized molecule does not increase rapidly enough with energy to compensate for the reduced Boltzmann factor in the case of the high critical energy. Consequently, the low pressure limit is underestimated. The shape of the curves is similar, but the falloff is shifted to higher pressure in the high activation energy calculation.

Although the new value of 1.78×10^{17} sec^{-1} is a much less anomalous high pressure A-factor than the previous estimates of 1 to 6×10^{14} sec^{-1}, (other A-factors for similar bond fission reactions are given below), the new value for the activation energy of 24.9 kcal/mole

TABLE NINE

HIGH PRESSURE A-FACTORS FOR BOND FISSION REACTIONS

Reactant	Products	$10g_{10}A$	Reference
C_2H_6	$2CH_3$	17.4	59
$C_2H_6N_2$	$2CH_3+N_2$	17.2	59
$C_8H_{18}O_2$	$2C_4H_9O$	15.6	59
HNO_3	$HO+NO_2$	16.5	56
HO_2NO_2	HO_2+NO_2	16.4	60
N_2O_5	NO_2+NO_3	17.3	This work
N_2O_5	NO_2+NO_3	(14.4)	Previous estimate[6]

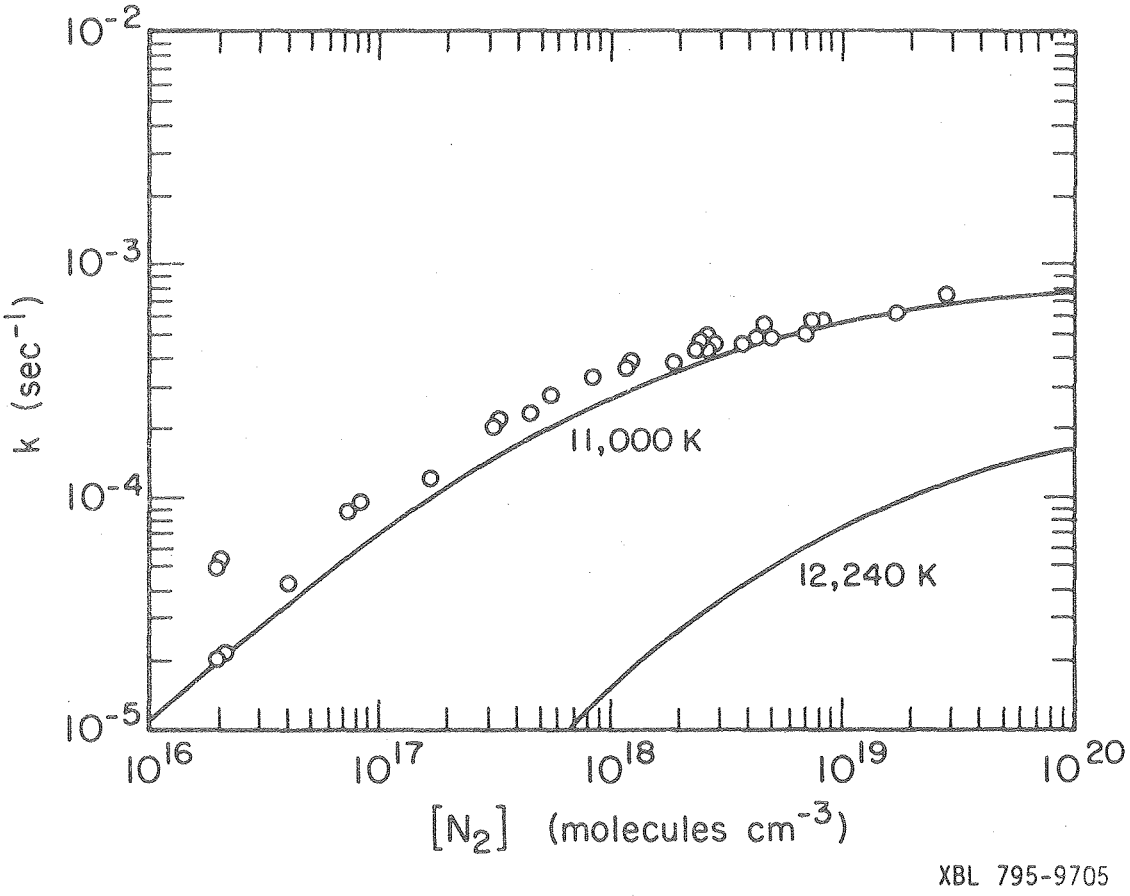

Figure 26. Results of RRKM calculation at 268 K.

implies a chemical barrier of about 2.7 kcal/mole in the recombination reaction, from the reaction enthalpy obtained by Graham of 22.2 kcal/mole. The hindered rotational transition state is based on recombination reactions with little or no activation energy, for which the barrier to recombination is only centrifugal. A chemical barrier to reaction would probably occur at a smaller separation of the fragments, corresponding to a tighter transition state and lower A-factor. Additionally, for the reaction

$$NO_2 + NO_3 \xrightarrow{e} NO + NO_2 + O_2 \qquad (76)$$

Graham[27] reported an activation energy at 300 K of 2.44±0.2 kcal/mole. It is difficult to imagine that the recombination reaction could have a larger activation energy than this.

A final consideration before extrapolation to stratospheric temperatures is the possible non-applicability of the Arrhenius form over wide temperature ranges. Tolman's definition of the activation energy is the difference of the average energy of the molecules that react and the average energy of all molecules. Since the average energy of all molecules is independent of pressure at a constant temperature, the difference of the activation energies at the high and low pressure limits represents the changing distribution of energized molecules.

At the low pressure limit, virtually all molecules with sufficient energy eventually react, since deactivation by collision is made slow with respect to reaction. The rate constant becomes the rate of energization, which the RRKM theory gives, assuming that the distribution of molecules below the critical energy is the equilibrium distribution, as

$$k_o' = (Q^*/Q)b \exp(-E_c/kT) \quad . \tag{77}$$

Q is the partition function for the molecule and Q^* is the partition function for energized molecules for the active vibrations and rotations measured from the ground state of the activated complex as $E^* = 0$. It depends only on the height of the barrier and the structure of the molecule. Q^* is much larger than Q, because the density of states increases rapidly with energy and the exponential energy term, $\exp(-E_c/kT)$, has been explicitly separated out. Hinshelwood[45] showed that the ratio of partition functions is approximately proportional to $(E_c/kT)^{s-1}$ where s is related to the number of modes. From the definition of the activation energy

$$E_a = kT^2 \, d \ln k/dT \tag{78}$$

the low pressure activation energy is seen to be

$$E_o = E_c - (s-1)RT. \tag{79}$$

The critical energy is usually on the order of the high pressure Arrhenius activation energy. In RRKM theory the high pressure rate constant is proportional to

$$(kT/h)(Q^+/Q) \exp(-E_c/kT), \tag{79a}$$

in which Q^+ and Q are the complete partition functions for the activated complex and reactant respectively. The factor kT/h arises from transforming one of the asymmetric stretching modes of the molecule, a high frequency vibration, into the reaction coordinate, which for a broad energy barrier corresponds to a low frequency vibration contributing kT/h to the activated complex partition function. Applying Eq. 78 to the expression for k_∞ gives

$$E_\infty = E_c + RT + RT^2 \left(\frac{\partial \ln Q^+}{\partial T} - \frac{\partial \ln Q}{\partial T}\right) . \qquad (79b)$$

If no other modes change dramatically in spacing of the energy levels, the critical energy will be RT smaller than the high pressure activation energy, or for the present result, about 12240 K. From the observed low pressure activation energy, s-1 is 8. This temperature dependence of the activation energy would be reflected in negative curvature in the Arrhenius plot.

An alternate expression for the low pressure rate constant, based on this derivation, is

$$k_o' = 3.1 \times 10^{18} T^{-8} \exp(-12240/T) \text{ cm}^3 \text{ molecule}^{-1} \text{sec}^{-1} . \qquad (80)$$

This expression is supported experimentally by the work of Schott and Davidson on the decomposition of N_2O_5 in shock tubes at high temperatures. They estimated the second order rate constant in the low pressure limit at 500 K, measured in argon, to be 6.4×10^{-15} cm^3 molecule^{-1}sec^{-1}. From the relative efficiencies measured by Wilson and Johnston[9] the corresponding value in nitrogen would be 1.14×10^{-14} cm^3 molecule^{-1}sec^{-1}. Eq. 80 predicts a value of 1.83×10^{-14} while the simple Arrhenius expression (53) gives 3.41×10^{-14} cm^3 molecule^{-1}sec^{-1}. Additionally they obtained over the range of 450-550 K at an equivalent gas density of about 2×10^{18} molecules cm^{-3} of nitrogen an activation energy of 8300 K. This density is somewhat above the second order limit at this temperature, so that the value is expected to be somewhat larger than the value of 8240 K obtained from Eq. 79, but the agreement in both activation energy and rate constant is very good.

The error made by extrapolating the simple Arrhenius form (53)

to the lowest stratospheric temperature of 229 K is nearly a factor of two in overestimation at high pressure compared to the value predicted by (80). The high pressure data to not cover a sufficient temperature range and are not of sufficient quality to investigate the T dependence of the high pressure activation energy. The RRKM result expressing the high pressure limit of E_a is from Eq. 79b.

$$E_\infty = E_c + RT + \langle E^+ \rangle - \langle E \rangle \quad . \tag{81}$$

The temperature dependence again results from changes in the distributions of all molecules and molecules that react, which change the average energy of the two groups. For loose complexes this produces a negative contribution to the apparent activation energy. The effect should be smaller than at the low pressure limit and the simple Arrhenius form (61) will also overestimate the rate constant at low temperature. The RRKM calculation of Baldwin and Golden[57] predicts only a 50 K change in the Arrhenius activation energy over an 82 degree temperature change about 300 K.

B. PHOTOCHEMISTRY

1. UV Spectrum of N_2O_5

The ultraviolet spectrum of N_2O_5 has been observed quantitatively by Urey, Dawsey and Rice,[61] by Jones and Wulf,[62] and by Johnston and Graham.[27] Daubendiek and Calvert also have published a near UV spectrum at low resolution.[63] The absorption first becomes evident at 380 nm and the cross-section increases smoothly with decreasing wavelength. The absorption is structureless at or below a resolution of 0.87 nm FWHM.

The work of Jones and Wulf and of Johnston and Graham agrees fairly well quantitatively. The cross-sections determined by Holmes and Daniels at 265 and 280 nm are also in close agreement. The low resolution values of Daubendiek and Calvert are about 30% smaller in the vicinity of 254 nm and somewhat outside of the ±20% error limits estimated by Johnston and Graham for their results.

Recent work in our laboratory by Ivan Wilson[64] at 243 and 273 K with 0.3 nm resolution agrees closely with the earlier work, showing little temperature dependence for the absorption below 280 nm. The results of the various workers are shown in Fig. 27. The value used in the quantum yield calculations was

$$\sigma(254\ \text{nm}) = 2.95 \times 10^{-19}\ \text{cm}^2\ \text{molecule}^{-1} \quad . \qquad (82)$$

2. Closed Cell Photolyses

The major interfering reactions in the photolysis of N_2O_5 are the reactions of NO_3

$$NO + NO_3 \xrightarrow{f} NO_2 + NO_2 \qquad (83)$$

and

$$NO_2 + NO_3 + M \xrightarrow{B} N_2O_5 \quad . \qquad (84)$$

The reaction of N_2O_5 with O atoms is negligible and the photolysis of NO_2, an effect of a few per cent, will not interfere at all if the reaction of NO with NO_3 can be suppressed. The experiments at 252 K were performed for this purpose. With a typical light intensity of 3×10^{15} photons $cm^{-2}sec^{-1}$, a cross section for absorption of 2.95×10^{-19} cm^2 and a quantum yield of one for the primary process, the photolytic

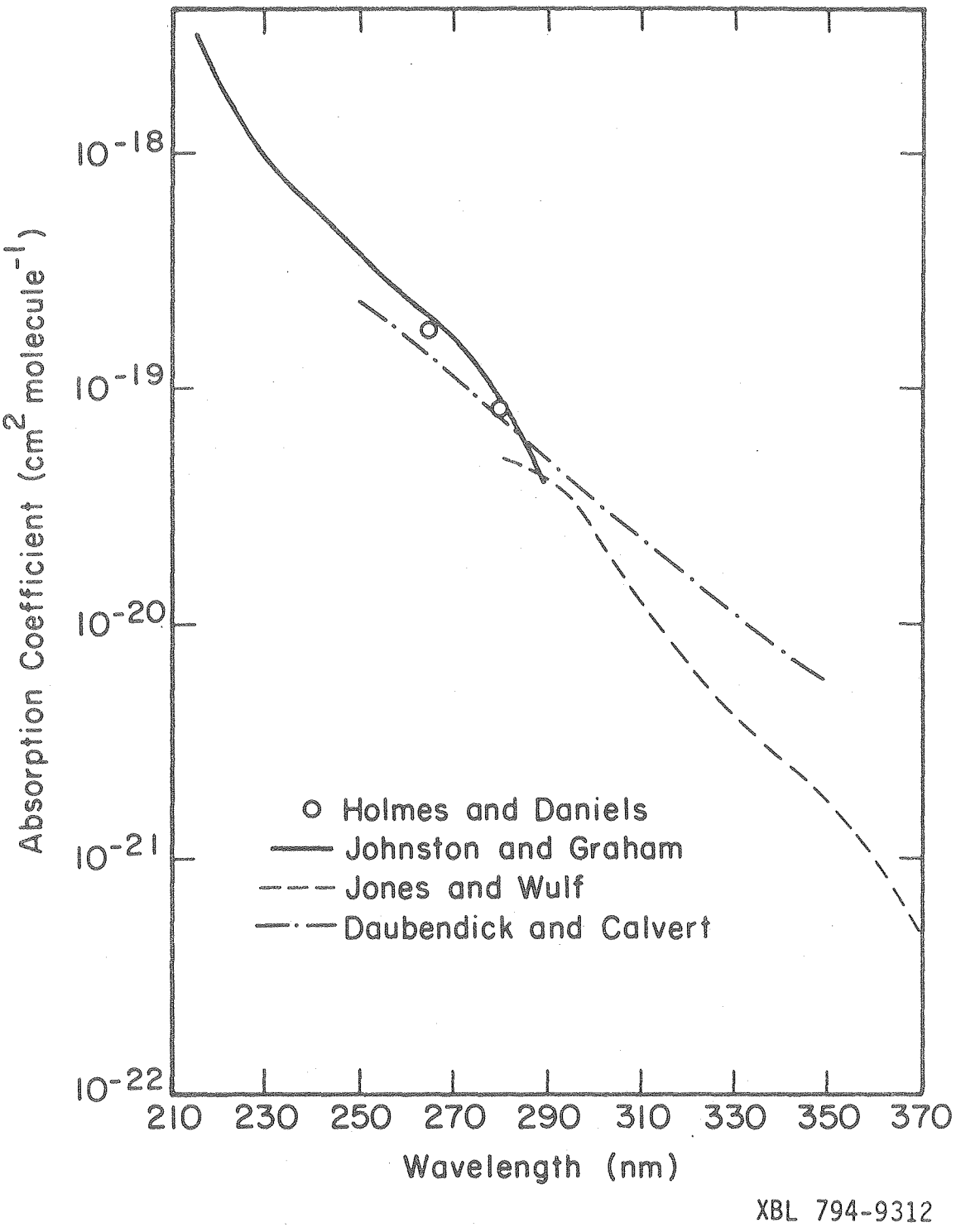

Figure 27. UV absorption spectrum of N_2O_5.

rate constant would be $8.7 \times 10^{-4} sec^{-1}$. The high pressure limit of the decomposition rate constant at this temperature is $4.4 \times 10^{-5} sec^{-1}$ and its value will be substantially lower, less than $1 \times 10^{-5} sec^{-1}$, at total gas concentrations smaller than 5×10^{17} molecules cm^{-3}. Its effect can then be ignored compared to the 10-20% experimental error.

For the typical ratio of N_2O_5 to NO_2 concentration of about 10, the recombination rate at low pressure of NO_2 and NO_3 is also less than 10% of the photolysis rate. The experiments under these conditions yield a direct measure of the primary quantum yield. The series of points obtained at a constant total effective nitrogen concentration of 1.5×10^{15} molecules cm^{-3}, but with varying N_2O_5 concentration are plotted in Fig. 28.

The clear dependence on N_2O_5 concentration apparently contradicts the finding of Murphy[15] of a lack of quantum yield dependence on N_2O_5 concentration between limits of 1.87 and 6.67 kPa ($5 \times 10^{17} < [N_2O_5] < 1.75 \times 10^{18}$ molecules cm^{-3}). One explanation of the fractional quantum yields observed in previous experiments could be the recombination of the assumed photoproducts NO_2 and NO_3, although Murphy discounts this possibility on the basis of a predicted $1/[NO_2]$ dependence which he does not observe. The low temperature and pressure results in the present work show that quenching of the excited $N_2O_5^*$ by other N_2O_5 molecules can account for the diminished quantum yield.

A simple mechanism of N_2O_5 photolysis at low pressure and temperature

$$N_2O_5 + h\nu \xrightarrow{\sigma I} N_2O_5^*$$

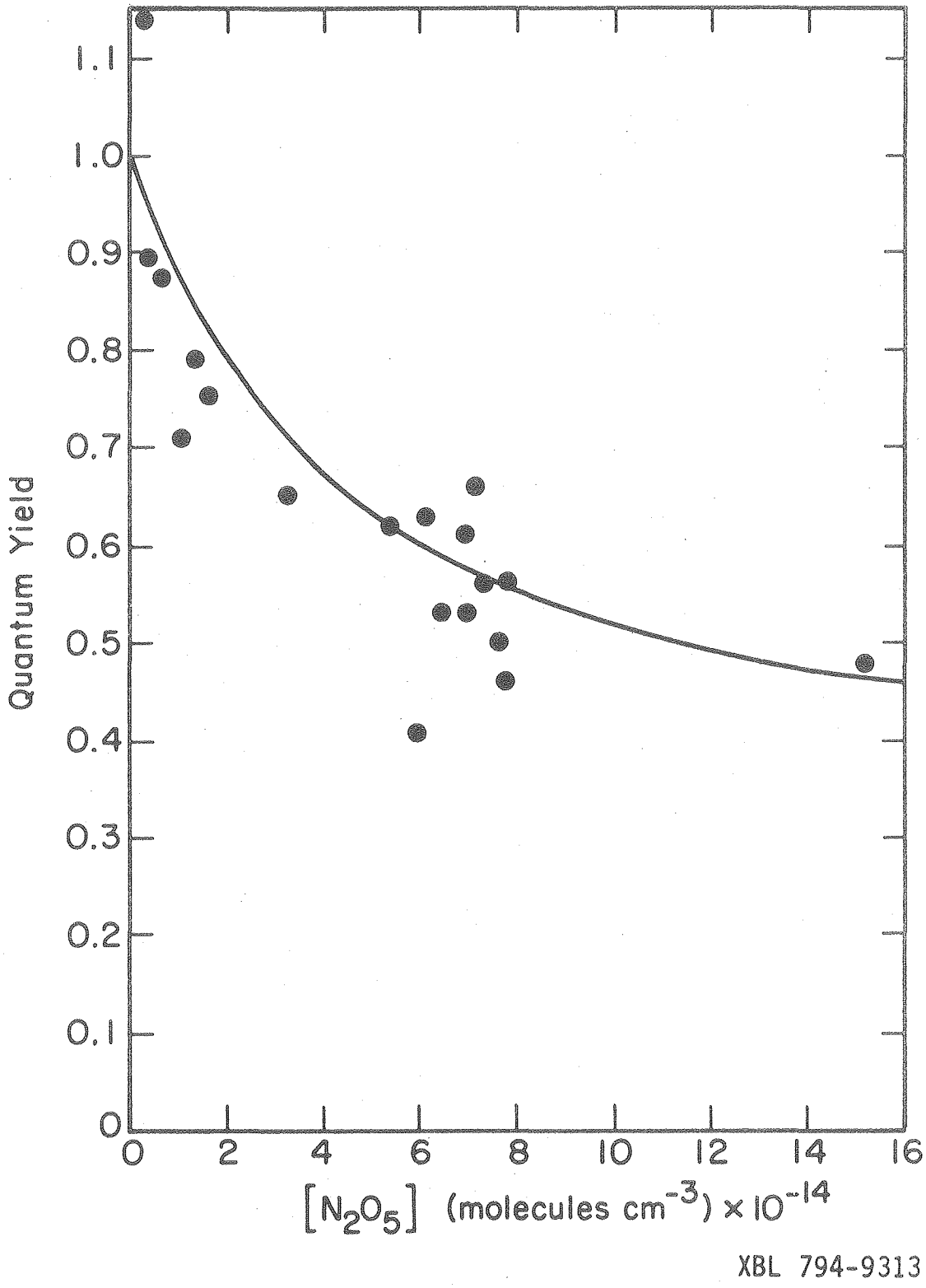

Figure 28. Photolysis quantum yields at low $[N_2]$.

$$N_2O_5^* \xrightarrow{k_1} \text{Products} \qquad (85)$$

$$N_2O_5^* + N_2O_5 \xrightarrow{k_{2a}} 2N_2O_5 \quad ,$$

properly predicts the approach to unit quantum yield as the N_2O_5 concentration is lowered, but also predicts near zero quantum yields for the concentrations used by Murphy. A second energy transfer reaction must be added

$$N_2O_5^* + N_2O_5 \xrightarrow{k_{2b}} \text{Products} + N_2O_5 \qquad (86)$$

to account for all observations. With (86) the steady state expression for $N_2O_5^*$ is

$$[N_2O_5^*]_{ss} = (\sigma I[N_2O_5])/k_1 + (k_{2a}+2b)[N_2O_5]) \quad . \qquad (87)$$

The quantum yield is given by

$$\Phi = (1/\sigma I[N_2O_5])\ (k_1+k_{2b}[N_2O_5])\ [N_2O_5^*]$$

$$= (k_1+k_{2b}[N_2O_5])/(k_1+(k_{2a}+k_{2b})[N_2O_5]) \quad . \qquad (88)$$

The limiting low pressure value is one and the high pressure result tends toward $k_{2b}/k_{2a}+k_{2b})$. Murphy's experiments in the high pressure region show that this ratio is 0.31 in pure reactant.

An upper limit to the rate constant k_1 can be deduced by assuming that $k_{2a}+k_{2b}$ is collisional. A least squares fit to the data using (88) produces a value of $(4.2\pm1) \times 10^{14}$ molecules cm^{-3} multiplied by the total quenching rate. At 252 K, the bimolecular collision rate constant, calculated with a collision diameter of 6Å, is 3.6×10^{-10} cm^3 $molecule^{-1}$

sec^{-1}, so that k_1, the collision-free decay constant of excited N_2O_5*, is less than or equal to 1.5×10^5 sec^{-1}. Eq. (88) is plotted as the line in Fig. 29. The corresponding collision-free lifetime is at least 6 μsec.

The marked variation in quantum yield with changing N_2O_5 concentration at a relatively constant total gas concentration is an indication that the products of photolysis are not the thermal products, NO_2 and NO_3. If this is the case, an estimate of the quenching constants of nitrogen and oxygen can be made from experiments at 252 K in higher pressures of the buffer gases, shown in Fig. 29. The thermal decomposition reaction is still much slower than photolysis, and although recombination will be faster, the assumption is that there is no NO_3 produced. The addition of foreign gas quenching to mechanism (85) and (86) adds the term $k_3[M]$ to the denominator of Eq. (83) for the quantum yield. A plot of $1/\Phi$ vs. $[M]$ should then be linear. There is inadequate medium pressure data to test this conclusion, but an estimate of about 1×10^{-14} cm^3 $molecule^{-1}$ sec^{-1} for the quenching constants of both nitrogen and oxygen can be made on the basis of the atmospheric pressure results.

The high pressure experiments in oxygen are apparently complicated by the production of ozone and the subsequent oxidation of NO_2 to NO_3. The reformation of N_2O_5 appears as diminished quantum yields and curvature in the semilog plots of N_2O_5 absorbance with time. In these cases, an estimate of the initial slope and light intensity were used to calculate the quantum yields.

Murphy quotes apparent quenching rate constants for several buffer gases that are about fifty times larger than the estimate above. The

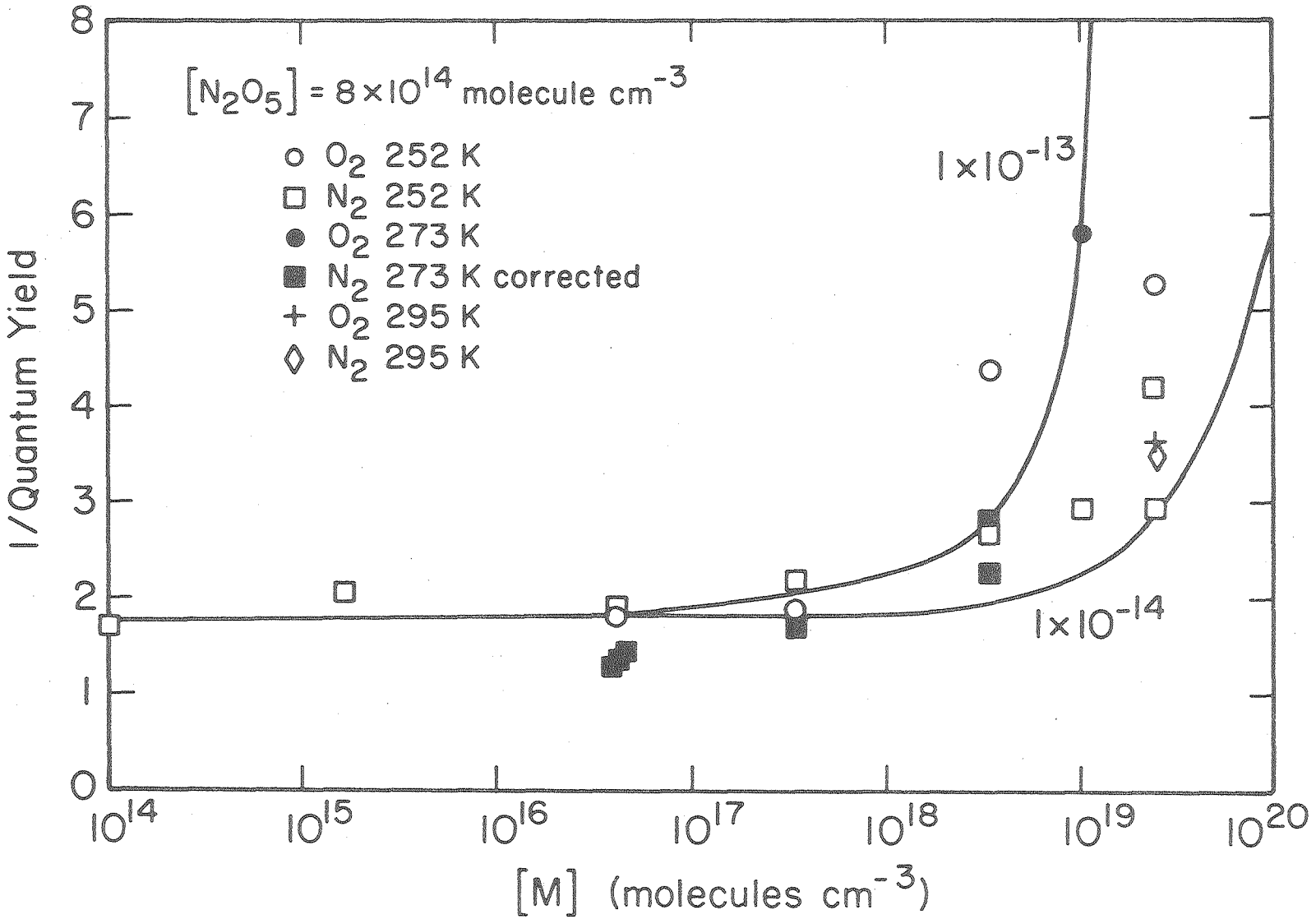

Figure 29. Photolysis quantum yields at varying $[N_2]$. XBL 794-9314

enhanced quenching efficiency he reports for oxygen is probably mostly due to oxidation of NO_2, but the discrepancy for nitrogen remains if Murphy's results are interpreted in terms of the proposed mechanism. However, the dependence on nitrogen pressure over his experimental range is small and perhaps negligible. SF_6 is generally much more efficient in quenching electronic excitation than is nitrogen, but Murphy reports only a factor of five between the quenching efficiency of SF_6 to N_2, suggesting that the quenching ability of nitrogen has been overestimated.

Data were also collected at 273 K in oxygen and nitrogen at a variety of pressures. At this temperature thermal decomposition becomes a significant additional reaction for number densities greater than about 3×10^{16} molecules cm^{-3}. NO produced either directly or subsequent to the photolytic event can eventually react with NO_3 produced by thermal decomposition, increasing the apparent quantum yield. Figure 30 shows the result of CHEMK calculations on the system

$$
\begin{aligned}
N_2O_5 + h\nu &\xrightarrow{\sigma I} 2NO_2 + O \\
NO_2 + O &\xrightarrow{m} NO + O_2 \\
N_2O_5 &\xrightarrow{A} NO_2 + NO_3 \\
NO + NO_3 &\xrightarrow{f} NO_2 + NO_2 \\
NO_2 + NO_3 &\xrightarrow{B} N_2O_5 \\
NO_2 + h\nu &\xrightarrow{j} NO + O \\
\hline
\text{net: } xN_2O_5 + h\nu &\xrightarrow{\sigma I} 2xNO_2 + 1/2xO_2 \quad .
\end{aligned}
\tag{89}
$$

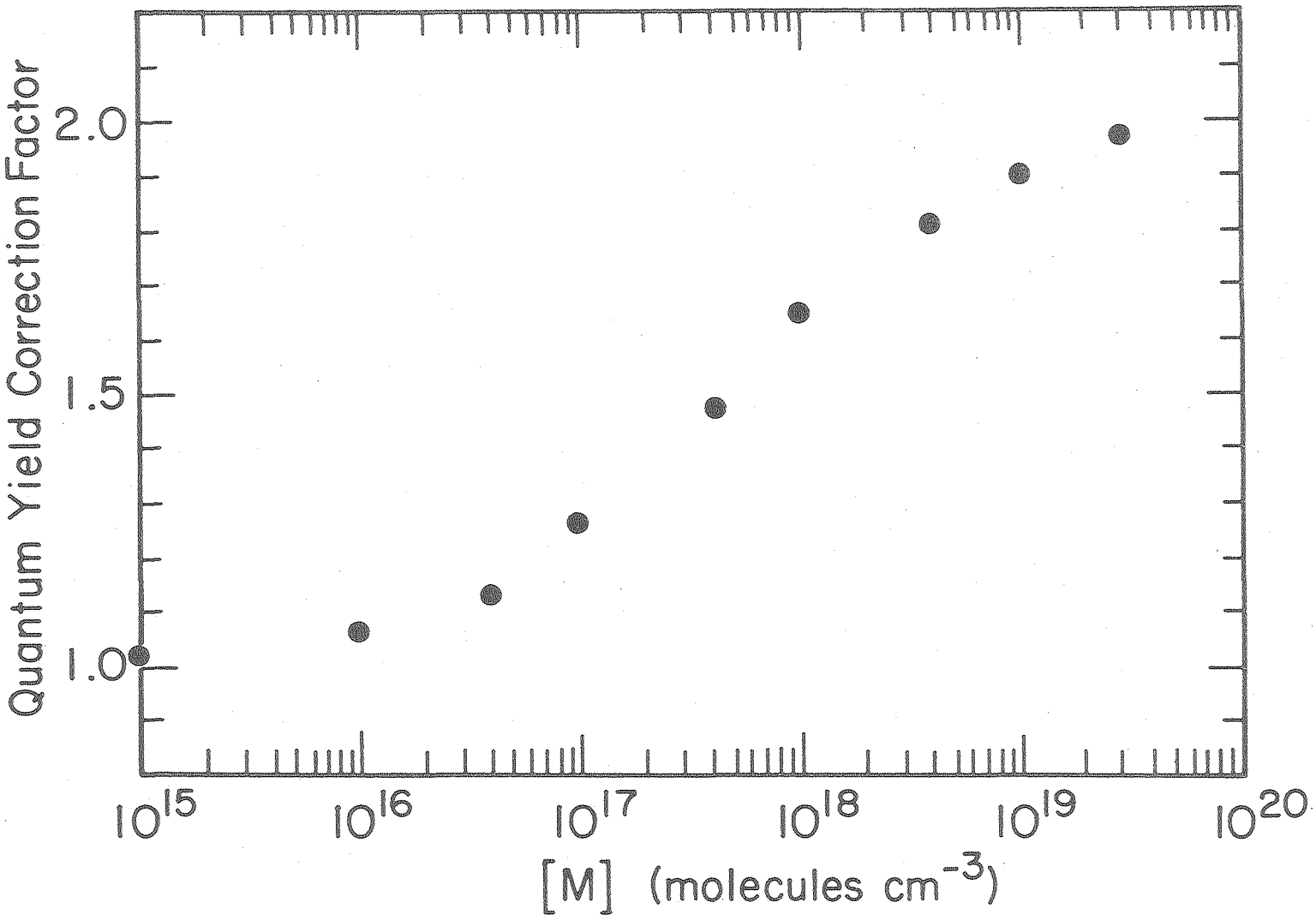

Figure 30. Primary quantum yield correction factors at 273 K.

XBL 794-9315

The quantum yield correction factor, x, is plotted as a function of total pressure, assuming $\sigma I = 1.0 \times 10^{-3} sec^{-1}$, a typical value at 273 K, and with appropriate rate constants for A and B measured previously. It is evident that the steady-state assumption fails for NO except at the highest pressures, that is, not every O atom ultimately participates in the destruction of another N_2O_5 molecule. The CHEMK program is thus used as a numerical integration technique for the expression of the N_2O_5 disappearance rate

$$- \frac{d[N_2O_5]}{dt} = \sigma I \Phi \, N_2O_5 + \frac{A[N_2O_5]}{1+\frac{B}{f}\frac{[NO_2]}{[NO]}} \quad . \tag{90}$$

The corrected data at 273 K are plotted as filled symbols in Fig. 29. Thus corrected for the pressure dependence of the thermal decomposition, the results indicate a quenching constant for nitrogen of the same magnitude as the 252 K results.

The 273 K results in oxygen again reflect the alternate pathway for O atoms in this system. The formation of ozone defeats the reaction step that contributes to the enhanced quantum yield in nitrogen. The subsequent ozone accumulation reoxidizes the product NO_2, further depressing the apparent quantum yield.

Finally, a few points obtained at 295 K and atmospheric pressure reemphasize the conclusion that an O atom is produced in the primary step. At this temperature and pressure, the dissociation-recombination rate constants are such that the quantum yield correction factor assumes its limiting value of two in nitrogen. In oxygen the initial limiting quantum yield is equal to that of the primary step. The factor of two

difference in empiric quantum yield obtained between N_2 and O_2 is strong evidence for O-atom production and against NO production in the primary step.

3. Constant Illumination in Flowing Systems

Constant intensity photolysis of chemical systems of N_2O_5 in a flowing carrier gas provides additional information on the primary products of photolysis. The basis of differentiation of the possibilities, $2NO_2$ + O and NO + NO_2 + O_2, is again the participation of oxygen in the chemistry if the O atom is produced. The decay with time, from the N_2O_5 concentration in a stabilized flow in the dark, after the lamps are turned on will be identical in oxygen and nitrogen, assuming equal quenching efficiencies, if the NO channel is followed, and different if the O channel is selected.

The experiments at 268 K have been simulated with the CHEMK package, using the complete chemical system detailed in Appendix B. Figure 31 shows the predictions of N_2O_5 behavior in oxygen and nitrogen assuming the two pathways. Figure 16 showed the experimental results. The good correspondence with the $2NO_2$ + O channel shows that the assumed mechanism is an adequate representation of the photolysis process.

4. Intermittent Photolysis in Flowing Systems

The results of the intermittent photolysis experiments provide independent confirmation of conclusions formed on the basis of the above constant illumination work. By probing the response of the chemical system to low frequency perturbations from a steady state, evidence

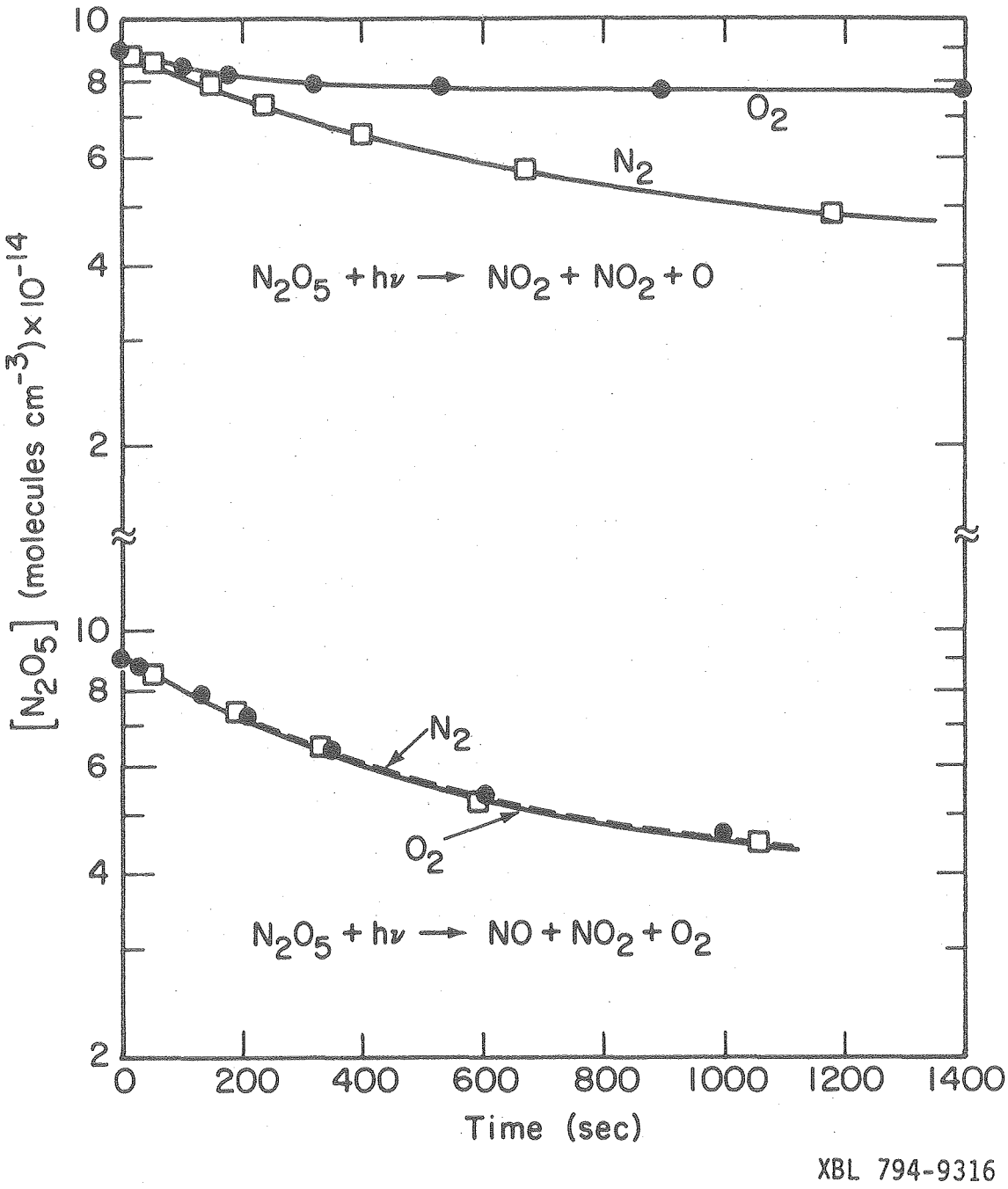

Figure 31. CHEMK model predictions in photolytic flow system.

on the role of a species in the scheme of reactions is available. The mechanism of Appendix B is used to predict the phase angles and modulation amplitudes of N_2O_5 and NO_2 as functions of photoproducts and photolysis rate constant.

Three different sets of conditions were explored. The predictions of the computer model in each of the cases are summarized in Table 10. The experimental results are also included. The first choice of conditions was modulation in nitrogen at 267 K and reduced pressures of 2.0 to 6.7 kPa. Under these parameters additional reactions dependent on the thermal decomposition, such as $NO + NO_3$, are slow compared to the 0.306 Hz flashing frequency. The recombination reaction of NO_2 with NO_3 is on the time scale of the flashing frequency. Consequently the two pathways

$$N_2O_5 + h\nu \longrightarrow 2\ NO_2 + O \qquad (91)$$

and

$$N_2O_5 + h\nu \longrightarrow NO + NO_2 + O_2 \qquad (92)$$

will result in the same N_2O_5 phase angle of $+90^\circ$, characteristic of a reactant destroyed by light in a first order process. The third possible channel

$$N_2O_5 + h\nu \longrightarrow NO_2 + NO_3 \qquad (93)$$

places the N_2O_5 phase angle into the second quadrant, indicative of a reactant reformed from the products of photolysis. The experimental results are in line with channels (91) and (92) with respect to phase angle. The modulation amplitudes are also in agreement, within their wide range of uncertainty, with those predicted using quantum yields interpolated from the static cell results. NO_2 modulation was below the detection limits in this system.

TABLE TEN

ASSUMED PRODUCTS	T	M	$[N_2O_5]$	$\phi_{N_2O_5}$	$\Delta I_{N_2O_5}/I$	$[NO_2]$	ϕ_{NO_2}	$\Delta I_{NO_2}/I$
$NO_2 + NO_3$	295 K	O_2:2.45E19	3.9E14	-156	3.9E-5	1.9E13	-30.9	1.7E-5
	267 K	O_2:2.75E19	7.0E14	141	2.3E-4	1.44E12	-39.9	0.11
	267 K	N_2:2.75E19	9.0E14	164	7.8E-5	1.12E12	-16.1	0.06
$NO + NO_2 + O_2$	295 K	O_2:2.75E19	2.2E14	75.5	2.2E-4	3.4E14	-148	1.46E-4
	267 K	O_2:2.75E19	8.0E14	91.1	2.6E-4	1.79E14	-90.0	2.46E-4
	295 K	N_2:2.45E19	1.8E14	63.2	2.4E-4	4.4E14	134.7	1.4E-4
	267 K	N_2:2.75E19	5.3E14	86.2	2.8E-4	6.9E14	-98.7	1.7E-4
	267 K	N_2:1.8E18	5.4E14	86.9	2.8E-4	6.5E14	-95.6	1.8E-4
$NO_2 + NO_2 + O$	295 K	O_2:2.45E19	3.5E14	89.0	2.5E-4	9.8E13	-95.0	1.8E-3
	267 K	O_2:2.75E19	6.4E14	89.0	1.2E-4	1.06E14	-91.0	1.4E-2
(a)	267 K	O_2:2.75E19	6.45E14	100.5	1.3E-4	1.06E14	-90.6	1.4E-3
	295 K	N_2:2.45E19	2.02E14	64.3	1.8E-4	3.9E14	152.8	1.7E-4
	267 K	N_2:2.75E19	5.8E14	89.4	2.2E-4	6.0E14	-105	2.0E-4
	267 K	N_2:1.8E18	6.0E14	91	2.0E-4			
Experimental	295 K	O_2:2.45E19	3.5E14	94±5	(5±2)E-4	1.1E14	-84±10	(3.5±1)E-4
	267 K	O_2:2.75E19	6.0E15	---	---	1.0E14	-91±3	(4±1)E-4)
	267 K	O_2:2.75E19	6.0E14	89±5	(2±.6)E-4	---	---	---
	295 K	N_2:2.45E19	1.9E14	60±15	(1.2±.5)E-4	---	---	---
	267 K	N_2:1.8E18	6.0E14	89±5	(2±.6)E-4	---	---	---

(a) ϕ = 0.3 for 2 NO_2 + O, 0.7 for $NO_2 + NO_3$.

The second set of conditions employed was flow at atmospheric pressure of nitrogen or oxygen at 267 K. Here again the thermal decomposition is too slow to affect the N_2O_5 phase angle for (91) or (92) in nitrogen or (92) in oxygen. The predicted modulation phase angle of 90° is again observed for N_2O_5, and while this eliminates (93) as the sole channel, the possibility of a partial contribution cannot be assessed on the basis of this experiment, since its contribution to the modulation amplitude is very small.

The modulation of NO_2 was observed in the oxygen runs. The phase angle observed of -90° falls at the expected 180° phase shift from its precursor N_2O_5. The steady state concentration and modulation amplitude are within the error limits of correspondence to the values calculated for channel (91). A somewhat larger steady state concentration would result for (92).

The final runs were made at room temperature with a low concentration of N_2O_5, maintained in a xylene slush bath, in an atmosphere of nitrogen or oxygen. The low concentration of N_2O_5 was intended to enhance the quantum yield by reducing quenching, while at room temperature the thermal decomposition was fast enough compared to the flashing frequency to alter the N_2O_5 phase angle, bringing it into the first quadrant. As in the prior static cell experiments, the alternative carrier gases will give different results for (91) and similar results for (92).

Both N_2O_5 and NO_2 modulation were observed in oxygen. The respective phase angles of +90° and -90° are again indicative of channel (91), in which the O is tied up by the high background concentration of

oxygen, rather than (92) for which the phase angle for N_2O_5 should be about 60°. The amplitudes are again of the proper order of magnitude.

The 60° phase angle of N_2O_5 observed at room temperature in nitrogen is final confirmation of O atom production in the primary step. It was hoped that some indication of the room temperature atmospheric pressure thermal decomposition rate constant could be obtained from the phase angle, but the experimental error is much larger than the small changes in phase angle calculated for factor of two changes in the decomposition rate constant.

5. Summary of Photolysis Results

In summary of the complete body of photolysis experiments the conclusions reached are:

1. The reduced quantum yields determined in this and previous work are not the result of rapid recombination of NO_2 and NO_3 as photoproducts, but of quenching of the electronically excited N_2O_5 by ground state N_2O_5 and to a certain extent by buffer gases (low pressure and temperature static cell decays).

2. The empiric quantum yield is also a function of secondary reactions involving the thermal decay of N_2O_5 (medium and high pressure static cell decays in N_2 and O_2 at 273 and 295 K).

3. The primary photoproducts include an oxygen atom and do not include any significant production of NO (flowing constant photolysis and modulation).

Theoretical structural studies, infrared spectral analysis and electron diffraction studies suggest a structure for N_2O_5 in which the N atoms are bound to a central O atom. Production of an oxygen atom in

photolysis could proceed by loss of one of the outer oxygens. The remaining product is the unsymmetrical isomer of dinitrogen tetroxide, N-O-N bonded, as opposed to the usual N-N bonded isomer. This unsymmetrical isomer has been observed in matrix isolation at liquid helium temperature[65] but disappears on warming of the matrix to liquid nitrogen temperature. This suggests that the O-N central bond requires only a few hundred joules/mole to break, allowing formation of the thermodynamically favored symmetrical form. Thus, the ΔH_f of N-O-N bonded N_2O_4 must be close to that of two isolated NO_2 molecules.

The 254 nm radiation used in the present study provides 472 kJ/mole of energy, of which about 303 are needed to produce two nitrogen dioxides and an oxygen atom, based on the known heats of formation of N_2O_5, NO_2 and $O(^3P)$. The 169 kJ/mole remaining falls short of the 190 kJ/mole necessary to excite the O atom to its first excited singlet state, ^1D. The excess energy must go to some combination of electronic, vibrational and rotational excitation of NO_2 and to translation of the three products.

The complete mechanism for the photolysis of N_2O_5 based on these results is

$$N_2O_5 + h\nu \xrightarrow{\sigma I} N_2O_5^*$$

$$N_2O_5^* \xrightarrow{k_1} NO_2 + NO_2 + O(^3P)$$

$$N_2O_5^* + N_2O_5 \xrightarrow{k_{2a}} N_2O_5 + N_2O_5$$

$$N_2O_5^* + N_2O_5 \xrightarrow{k_{2b}} NO_2 + NO_2 + O(^3P)$$

$$N_2O_5^* + M \xrightarrow{k_3} N_2O_5 + M$$

$$N_2O_5 \xrightarrow{A(M)} NO_2 + NO_3$$

$$NO_2 + NO_3 \xrightarrow{B(M)} N_2O_5$$

$$NO_2 + O \xrightarrow{m} NO + O_2$$

$$NO + NO_3 \xrightarrow{f} NO_2 + NO_2.$$

For $M=O_2$ the reactions

$$O + O_2 + O_2 \xrightarrow{P} O_3 + O_2$$

$$NO_2 + O_3 \xrightarrow{e} NO_3 + O_2$$

are also important.

V. STRATOSPHERIC IMPLICATIONS

A. EXTRAPOLATION OF THE THERMAL DISSOCIATION RATE CONSTANT

At sunset in the stratosphere, practically all the NO present is rapidly oxidzed to NO_2 by ozone

$$NO + O_3 \longrightarrow NO_2 + O_2 \tag{94}$$

The NO_2 is then more gradually oxidized to NO_3, with which it then combines to form N_2O_5

$$\begin{aligned} NO_2 + O_3 &\xrightarrow{e} NO_3 + O_2 \\ NO_2 + NO_3 + M &\xrightarrow{B} N_2O_5 + M. \end{aligned} \tag{95}$$

In order to predict the concentration behavior of NO_2, NO_3 and N_2O_5 in the stratosphere with some sort of computer model the rate constants e, B and A, the thermal dissociation rate constant, must be known as functions of temperature and pressure. The value of e over a range of temperatures has recently been measured by Graham, who also evaluated the equilibrium constant for N_2O_5 dissociation, $K_{eq} = A/B$. From this B can be inferred from A.

The values for A previously compiled for the use of atmospheric modelers[32] include a second order limiting low pressure expression for which the total gas concentration consisted of equal molar amounts of NO and N_2O_5. Accounting for the difference of 2.28^7 by which N_2 is a less effective collision partner than NO/N_2O_5, the suggested value and the present value (53) are in agreement. For use in atmospheric models,

though, the corrected form in N_2 should be used. Two first order expressions are also given, one at one atmosphere and one at the high pressure limit. Both are based on the estimated activation energy of Mills and Johnston.[6] The present value is larger than previously estimated and will lead to substantially smaller rate constants upon extrapolation to stratospheric temperatures.

Total gas concentrations in the stratosphere fall within the "fall-off" region of the thermal decomposition rate constant, so that neither the strictly second-order nor strictly first-order expressions are applicable. Data obtained in this region has been presented (Fig. 24) but for ease of computation an interpolation formula is necessary. The simplest formula connecting the high and low pressure limits is that of Lindemann

$$k = \frac{k_\infty k_o'[M]}{k_\infty + k_o'[M]} \tag{96}$$

This expression does not consider the actual distribution of reacting molecules over many energy levels above the critical energy and overestimates the value of the rate constant in the fall-off region. Equation (67) was introduced to account for the spread of reacting states and can be used as the interpolating function in form (67a). The use of a constant value for J, for example the value of 6.5 determined from a fit to the present data, is a first order approximation, since J varies slowly with both gas concentration and temperature. The data are however insufficiently detailed experimentally to determine the dependences.

Finally the inapplicability of the Arrhenius form for k_o' and k_∞

over wide ranges of temperature has been discussed. The next most simple form, in which the activation energy is considered temperature independent but a T^n factor is included in the preexponential terms, has been applied to k_o', the result given in Eq. (80). Figure 32 shows profiles of the rate constant A, calculated using standard temperature and gas density profiles, from Eq. (53) or (80), (61), and (67). Also shown is the extrapolated curve of Viggiano, et al.[11] The T^n form predicts values 10 to 20% smaller than the strict Arrhenius form throughout the stratosphere. This difference is within the other probable errors in extrapolation.

The qualitative time behavior of NO_2, NO_3 and N_2O_5 can be understood by considering the pertinent rate equations. Making the steady state assumption for $[NO_3]$, the rate expression for $[NO_2]$ is

$$-\frac{d[NO_2]}{dt} = 2\, e[NO_2][O_3]. \tag{97}$$

The ozone concentration is more than a thousand times larger than that of NO_2 and can be considered constant, so that NO_2 will decrease exponentially with a time constant of $(2e[O_3])^{-1}$, which is on the order of 16 hours.

Assuming again the $[NO_3]$ steady state, the integrated rate expression for $[N_2O_5]$ is

$$[N_2O_5]_t = [N_2O_5]_o + e[NO_2][O_3]t. \tag{98}$$

The N_2O_5 is depleted during the day by photolysis to a value $[N_2O_5]_o$ at sunset. NO_2 and O_3 are both present in larger concentrations and are

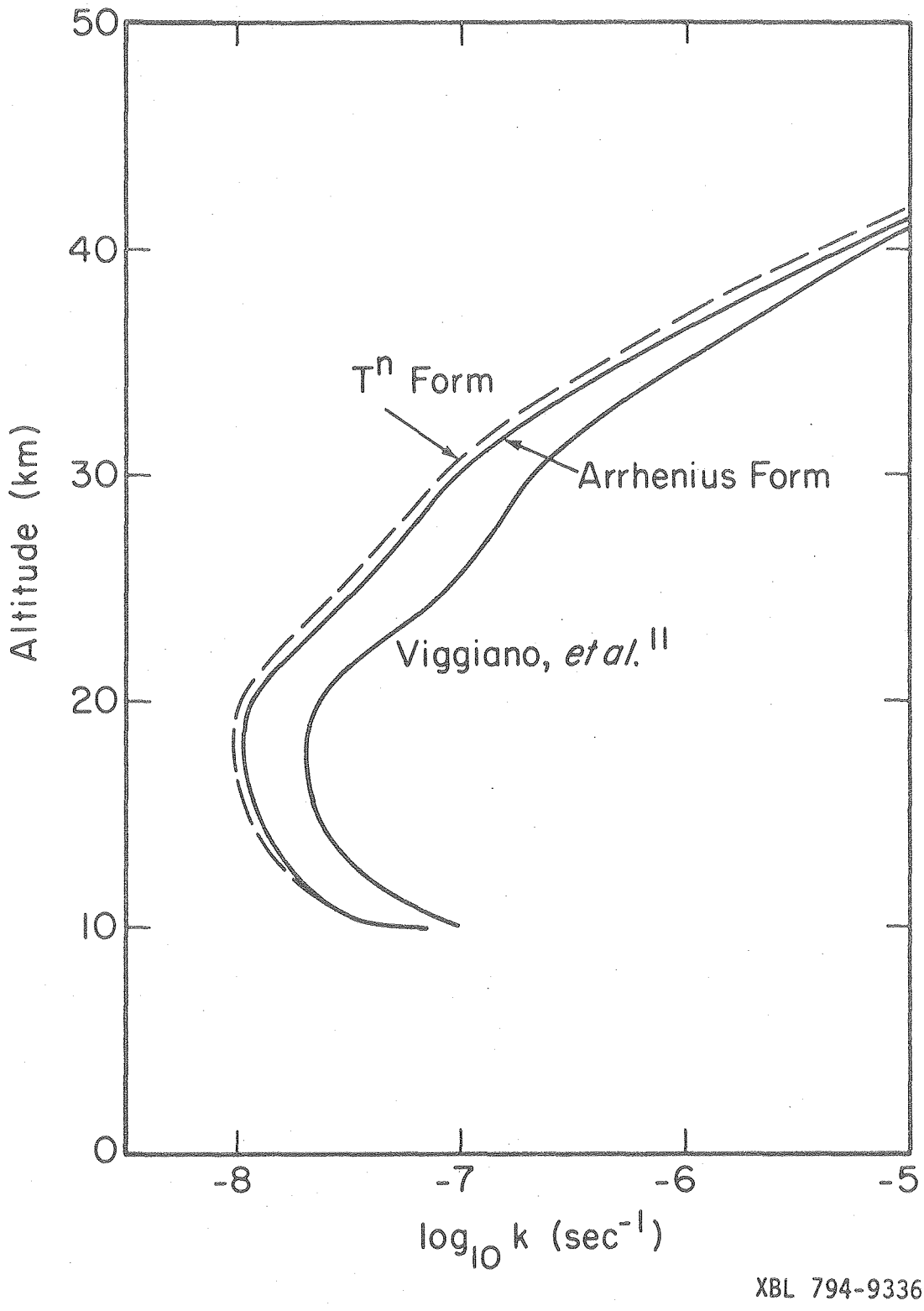

Figure 32. Thermal decomposition rate constants in the stratosphere.

constant to the first approximation. The N_2O_5 then builds up linearly during the night starting from its sunset value.

The NO_3 steady state concentration is given by

$$[NO_3]_{ss} = \frac{e[O_3]}{B[M]} + K_{eq}\frac{[N_2O_5]}{[NO_2]} \quad . \tag{99}$$

Shortly after sunset, when the ratio of N_2O_5 to NO_2 is small, the NO_3 abundance is controlled by the first term in (99). It is predicted to be a constant independent of the NO_2 concentration and inversely dependent on the value of B, the recombination rate of NO_2 and NO_3. The previous values of B, based on the previously estimated Arrhenius parameters for the thermal decomposition of N_2O_5, were much larger than those predicted by the present measurements, resulting in lower estimates of NO_3 stratospheric abundance. As the night progresses the second term in (99) becomes larger as NO_2 is converted to N_2O_5, and the steady state concentration of NO_3 grows. The time constant for approach to chemical steady state from the daytime NO_3 levels, depleted by photolytic decomposition, is related to $(B[NO_2][M])^{-1}$, so that smaller values of B slow down the production of N_2O_5 and increase the steady state NO_3 concentration as the NO_3 formed from the oxidation of NO_2 piles up. The time constant for the approach to equilibrium is short in the lower and middle stratosphere, less than an hour, validating the use of the steady state assumption in the discussion of NO_2 and N_2O_5 behaviors. In the upper stratosphere, above 40 km, $[NO_2]$ and [M] are both decreasing, so that the NO_3 builds up to a higher concentration more slowly.

B. NIGHTTIME STRATOSPHERE MODEL

A one-dimensional atmospheric model, which uses the Gear method to evaluate the coupled differential equations representing the rates of the various chemical reactions in the stratosphere, has been modified by a coworker, Susan Solomon, to include the additional NO_x chemistry involved with NO_3 and N_2O_5. The Gear method, with its variable integrating step size, is particularly suited to the fast time scale chemistry which takes place around discontinuities in the stratosphere, such as sunset. The model uses standard temperature, density and ozone profiles representative of the mid-latitude atmosphere in the spring or fall. Since the atmosphere is well mixed longitudinally, the "one dimension" in the model is altitude. Vertical mixing in the stratosphere is treated with a vertical eddy diffusion coefficient model.

The NO_2 distribution and the starting points for the NO_3 and N_2O_5 distributions are obtained by running the model in its standard mode, with a constant average illumination for many years of model time. The sunset distributions of the three species are obtained from several cycles of diurnal variation, effectively turning the sun on and off for twelve hour periods until the same distributions are produced at sequential sunsets.

Finally, the effects on the nocturnal distributions of NO_2, NO_3 and N_2O_5 of changes in the rate constants A and B were studied with single twelve hour nighttime simulations. Figure 33 shows the vertical profiles of the time constant of the NO_3/N_2O_5 chemistry and of $[NO_2]$ at 1800 hours (sunset). It is evident that in the region of the NO_2 maximum, around

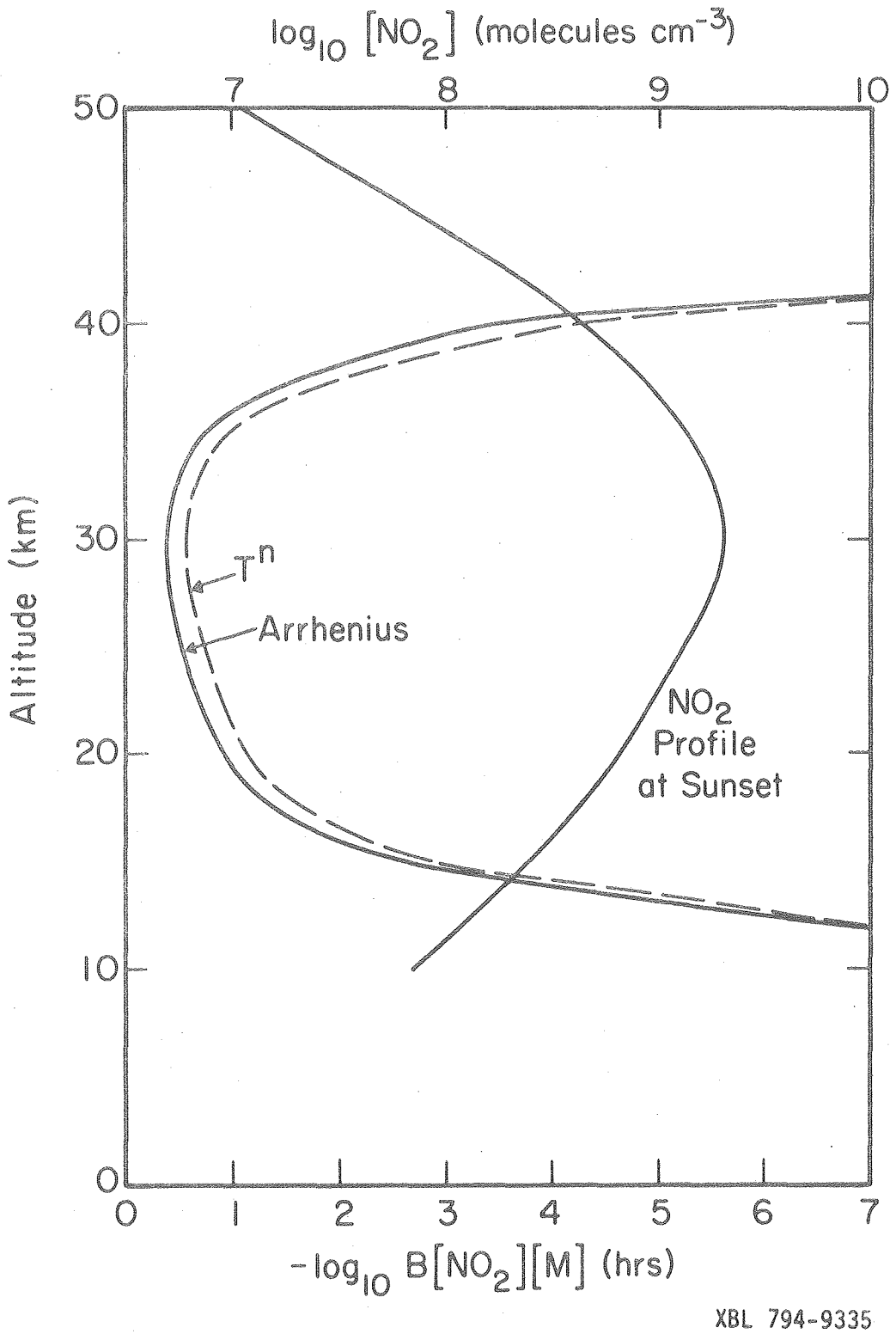

Figure 33. NO_3/N_2O_5 time constant and NO_2 vertical profile at sunset.

30 km, the chemistry is most rapid. The total column abundance of NO_2 above 15 km, shown in Fig. 34, decreases exponentially with a time constant longer than the twelve hours of darkness, as expected. The behavior is similar for both the Arrhenius extrapolations of A and the T^n form. The decreased total column in the second case is a result of increased early evening conversion to NO_3 and N_3O_5, shown in Fig. 35. This arises from the 20-30% smaller rate constant B predicted by this form.

Figure 35 also indicates the expected linear increase in the N_2O_5 total column abundance above 15 km. The NO_3 column exhibits a rapid buildup in the first hour after sunset from its photolytically depleted daytime value, followed by a gradual increase resulting from the buildup of N_2O_5. The concentration behavior as a function of time and altitude of both NO_3 and N_2O_5 is shown in detail in Fig. 36. N_2O_5 increases gradually at all altitudes. The risetime for NO_3 is directly related to the time constants shown in Fig. 33, being most rapid in the 25-30 km region. The gradual increase in the NO_3 total column during the night is mostly attributable to higher concentrations in the upper stratosphere, above the NO_2 maximum, where the higher temperature favors the product side of the N_2O_5 thermal dissociation equilibrium.

The calculation can to some extent be tested by constraints based upon observations of the stratosphere. The predicted N_2O_5 concentrations, about 3×10^7 molecules cm^{-3} at 25 km at sunset, are smaller than the upper limits on N_2O_5 concentration reported by King, et al.,[66] and by Ridley, et al.[67] Evans, et al.[68] report a predawn observation of the 8.1 μm absorption of N_2O_5 which shows a mixing ratio of 3 ppbV above 30 km, or about 1.2×10^9 molecules/cm^3 which is in excellent agreement with the

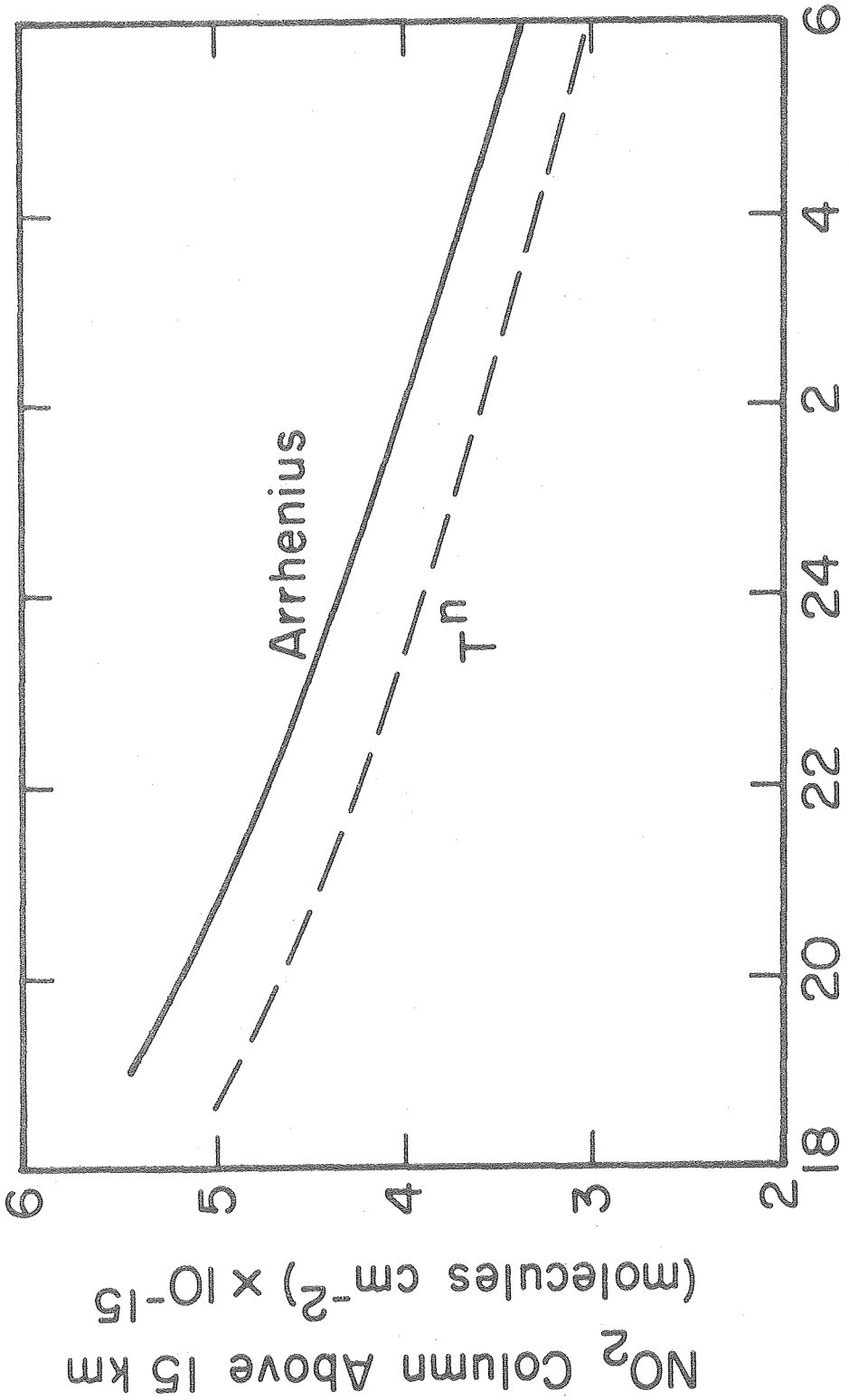

XBL 794-9311

Figure 34. Total column abundance of NO_2.

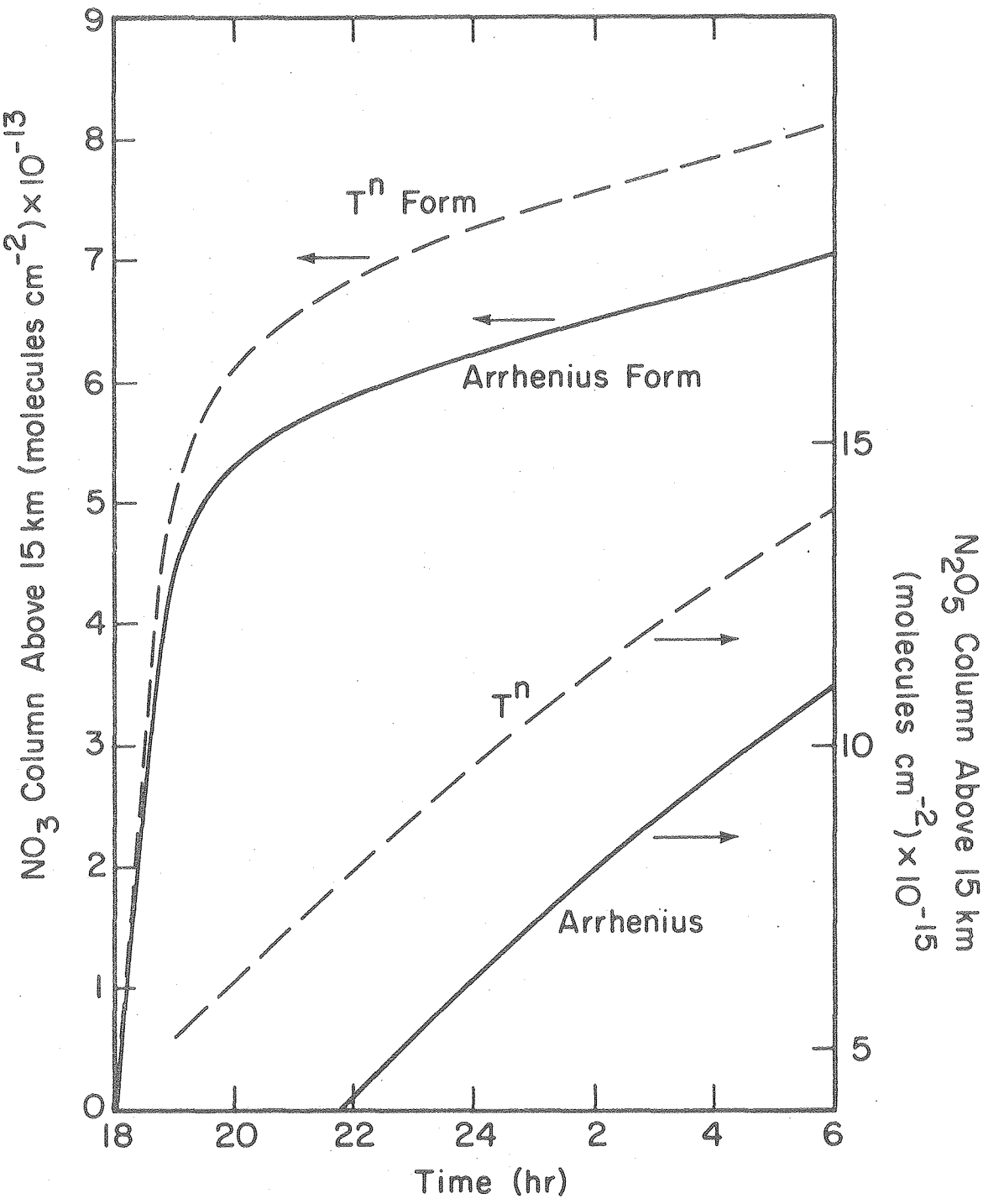

Figure 35. Total column abundances of NO_3 and N_2O_5.

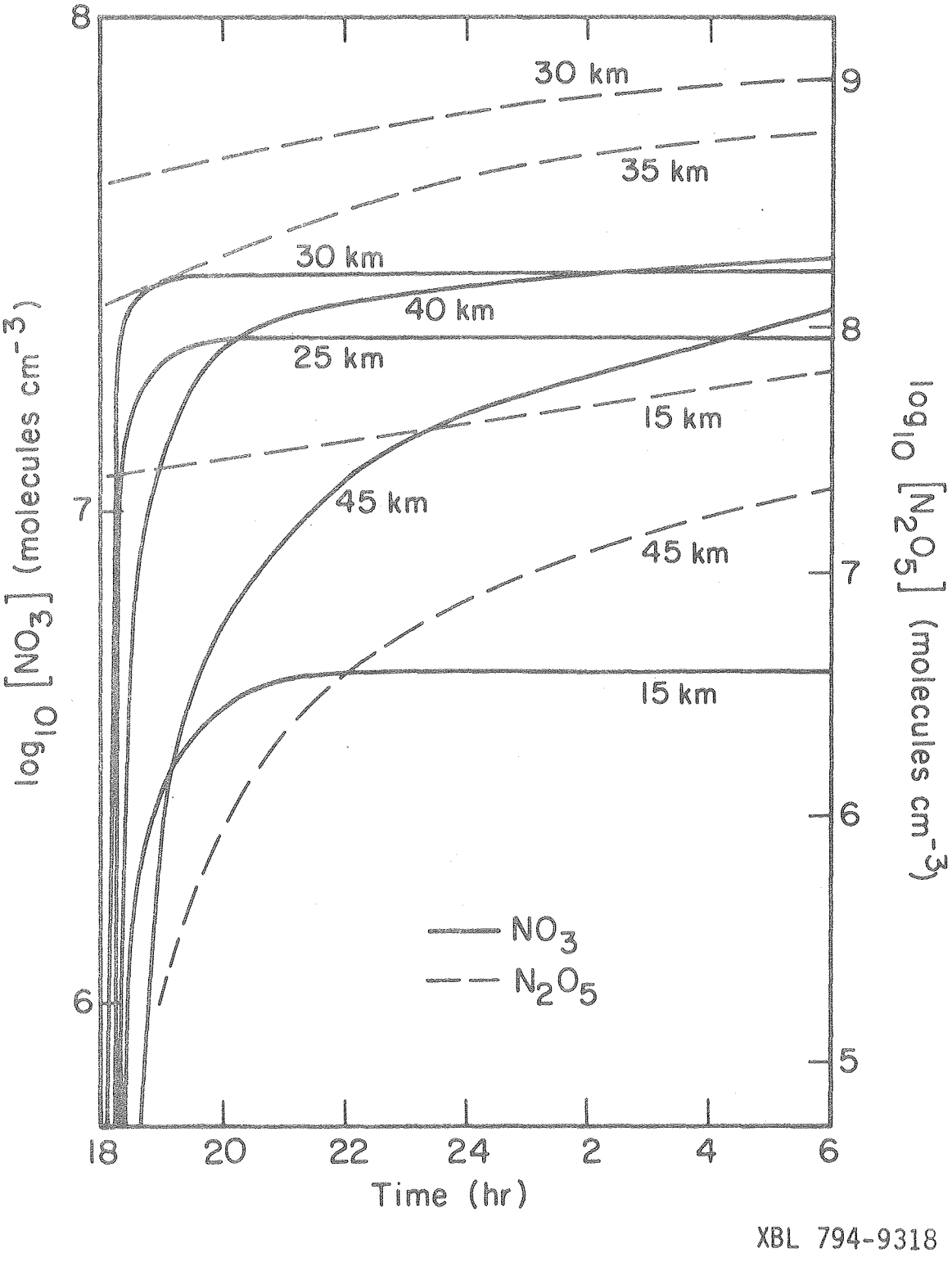

Figure 36. NO_3 and N_2O_5 concentration behavior.

model prediction of a concentration maximum at 30 km of 1.0×10^9 molecules/cm^3 before sunrise. Noxon[12] has employed the moon as a source for his visible absorption technique to monitor total column abundances of NO_2 and NO_3 during the night. Three observations of NO_3 were made over a three night span in April at mid-latitude. The three observations, one made 40 minutes after sunset and the other two toward the end of the night, all implied a total column abundance of $1.0 \pm 0.2 \times 10^{14}$ molecules cm^{-2}. If the three observations are considered typical of a single night, the NO_3 column increase from shortly after sunset to the end of the night is less than 30%, somewhat smaller than the model result of about 35%. In addition the total column abundance, which Noxon suggests is entirely in the stratosphere and centered at 40 km, is about 40% larger than model predictions. Agreement in the total column amount can be forced by further reduction of the foward and reverse rate constants in the N_2O_5 equilibrium, as Noxon showed, or by a reduction in temperature from the standard atmosphere values. The NO_2 total column, observed simultaneously, was about four times higher than normal during the NO_3 observations, which would contribute to a shortened initial risetime for NO_3, but the 35% increase in NO_3 column calculated by the model is fairly independent of the NO_2 column and would still fall outside Noxon's limit of 30% on the night time change in NO_3.

In view of the large experimental error in the NO_3 observation and the uncertainty in the actual ozone and temperature profiles pertinent to the time of the observation, the model cannot really be considered to be in disagreement with these preliminary stratospheric monitoring results. Despite further attempts, Noxon[69] has been unable to

repeat the identification of NO_3 in the night sky, with a lower detectable limit of around 1×10^{14} molecules cm^{-2}. This perhaps highlights the unusual nature of the stratosphere at the time of the observations and is in agreement with model predictions of a typical NO_3 column of $7\text{-}8 \times 10^{13}$ moleculues cm^{-2} at the end of the night.

C. N_2O_5 PHOTOCHEMISTRY IN THE STRATOSPHERE

N_2O_5 concentrations in the stratosphere are so low that the additional reactions which complicate laboratory scale photolyses are negligible. The previous suggestion to modelers was to use Murphy's quantum yield of 0.6 measured in low pressures of nitrogen, divided by two to account for the destruction of an additional N_2O_5 molecule by the oxygen atom produced in the laboratory experiment. The present work shows that the quantum yield is also sensitive to the N_2O_5 concentration, but at the stratospheric density of N_2O_5, the chances of a photoexcited N_2O_5 molecule colliding with a ground state N_2O_5 are nil. The quantum yield is controlled by foreign gas quenching, primarily by nitrogen. From the collision free photodecomposition constant and the estimate made for the nitrogen quenching constant in Sec. IV.B.2, the quantum yield for N_2O_5 photolysis can be calculated as a function of altitude. The result, Fig. 37, shows that the quantum yield is essentially one in the region of significant N_2O_5 concentration. The previous suggested value is indicated by the broken line.

Although the thermal decomposition and recombination rates control the night time behavior of NO_3 and N_2O_5, photodecomposition of both of these species is overwhelmingly important during the day. The work of

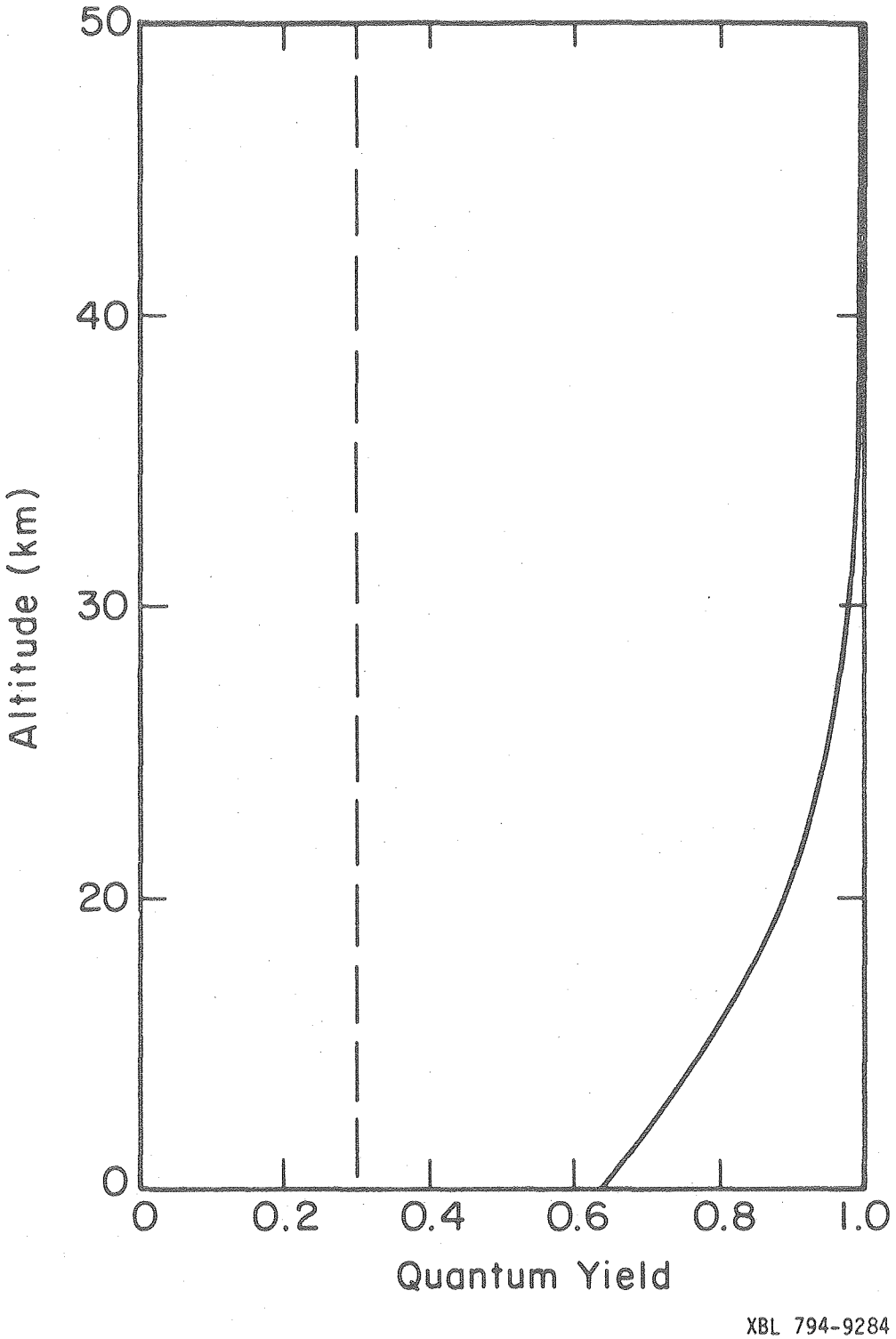

Figure 37. Photolytic quantum yield of N_2O_5 in the stratosphere.

Holmes and Daniels and of Murphy shows no indication of wavelength dependence of the quantum yield to 280 nm. If the quantum yields determined in the present work are assumed applicable throughout the continuous ultraviolet absorption of N_2O_5, "j" values, the wavelength integrated product of cross section, intensity and quantum yield, can be determined as a function of altitude from the incident solar intensity and the distributions of important UV absorbers, mostly O_2 and O_3. The stratospheric model has been used to generate the noontime mid-latitude spring/fall j values shown in Fig. 38. These first order photolytic constants are larger throughout the stratosphere than the first order thermal decomposition constants of Fig. 32.

A significant portion of the active absorption of light comes from the longer wavelengths, $\lambda > 300$ nm, for which the intensity is larger. Absorption cross section measurements are difficult in this region, because of the small cross section and overlapping absorptions of other species present in the laboratory experiments. The cross sections reported by Jones and Wulf have been used in the j value calculation for this region, but the results of Graham and of Daubendiek and Calvert indicate that the cross sections may be up to 40% larger at 300 nm.[37]

Ridley, et al[67] have observed the diurnal behavior of NO using a chemiluminescent detection techniques and have related its gradual growth during the day to the photolysis of N_2O_5. In doing so, they concluded that, using the cross sections of Jones and Wulf, a quantum yield much larger than 0.3 and perhaps larger than 1.0 was necessary to explain their observations. The present work shows that the larger quantum

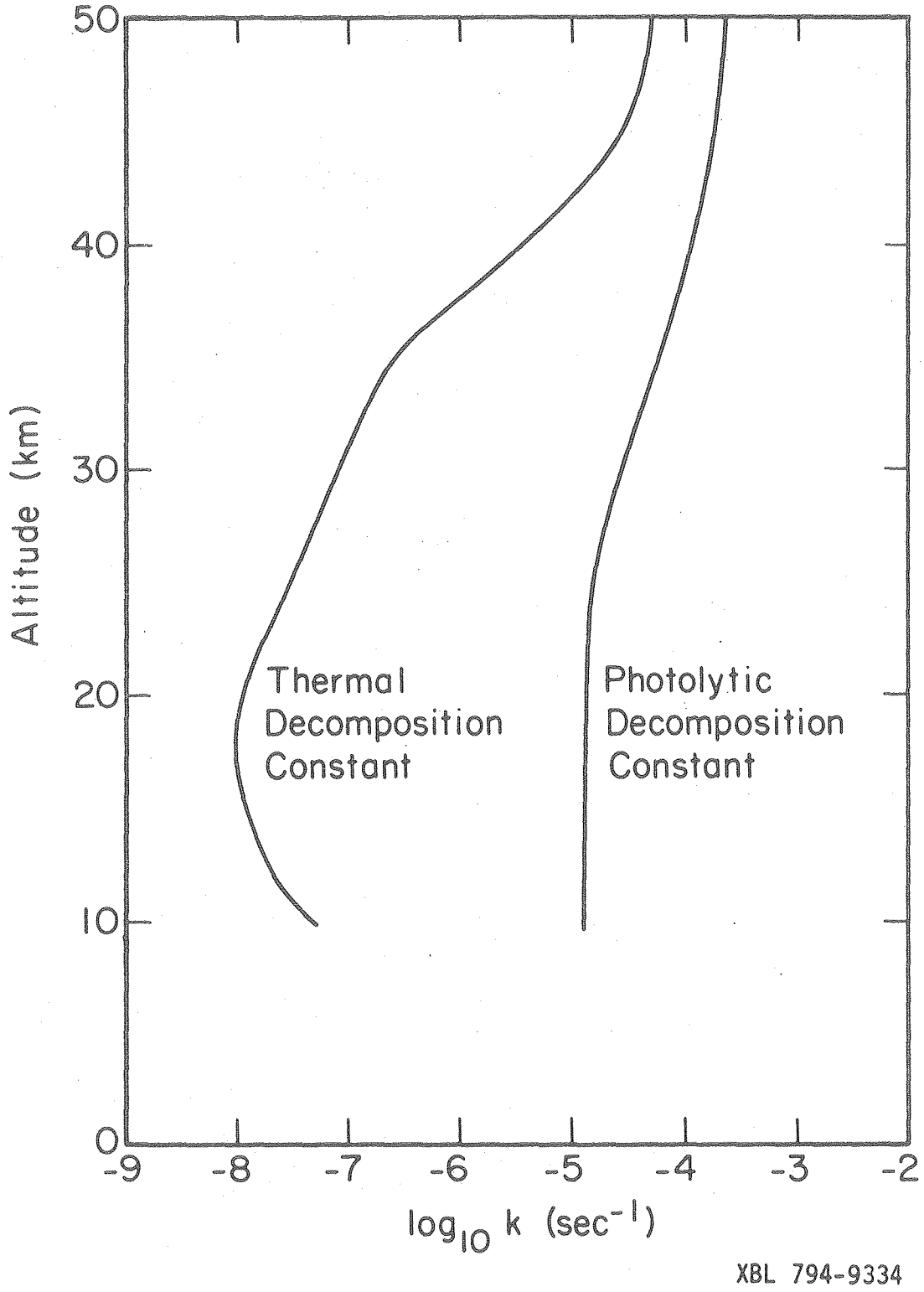

Figure 38. Photolytic and thermal decomposition rate constants in the stratosphere.

yield is expected under stratospheric conclusions. The remaining discrepancy is within the uncertainties of the cross sectional values.

APPENDIX A: MULTIPARAMETER NON-LINEAR LEAST SQUARES FITTING PROGRAM

The following FORTRAN program was used to fit the thermal dissociation data to the parameterized form prescribed in the subroutine FUNCTN. Given a starting point close to the minimum of the variance on the hypersurface of the fitting parameters, it seeks the minimum to within some error tolerance by incrementing the fitting parameters and numerically differentiating the variance. The program was run on PDP 11/10 computer.

```
FORTRAN IVV01C-03A                                    PAGE 001

0001          PROGRAM N205
0002          IMPLICIT DOUBLE PRECISION (A-H,O-Z)
0003          COMMON SIGMAA(10),CHISQR,FLAMDA
0004          COMMON/DIFF/ A(10),DELTAA(10),X(100),DERIV(10),T,NTERMS
0005          COMMON/CHI/ Y(100),SIGMAY(100),YFIT(100),NPTS,NFREE,
             CMODE,WEIGHT(100)
0006          COMMON/MATRIX/ARRAY(10,10)
0007          DIMENSION X1(100),Y1(100)
0008          CALL ASSIGN (1,'DX1:DCDAT.DAT',13,'OLD')
0009          CALL ASSIGN (9,'KB:')
0010          READ (1,100) NPTS
0011    100   FORMAT (I2)
0012          READ(1,101) (X1(I),Y1(I),I=1,NPTS)
0013    101   FORMAT(8E10.4)
0014          TYPE 200
0015    200   FORMAT (' INPUT START/STOP POINTS FOR FIT, NTERMS, MODE, T')
0016          READ (5,300) M9,N9,NTERMS,MODE,T
0017    300   FORMAT (4I2,F5.1)
0018          WRITE(5,301) M9,N9,NTERMS,MODE,T
0019    301   FORMAT(/,1X,4(I2,2X),F5.1)
0020          B1=9.44E-6*DEXP(-9660/T)
0021          TYPE 400
0022    400   FORMAT(' INPUT INITIAL PARAMETER GUESSES, THEN INCREMENT VALUES')
0023          READ (5,500) (A(J),J=1,NTERMS),(DELTAA(K),K=1,NTERMS)
0024    500   FORMAT (8E10.4)
0025          NPTS=N9-M9+1
0026          DO 1 I=1,NPTS
0027          WEIGHT(I)=(1./Y1(I+M9-1))
0028          SIGMAY(I)=1.0
0029          X(I)=X1(I+M9-1)
0030        1 Y(I)=Y1(I+M9-1)
0031          WRITE(5,900) (X1(I),Y1(I),I=M9,N9)
0032    900   FORMAT(1X,E10.4,3X,E10.4)
0033          NFREE=NPTS-NTERMS
0034          DO 2 I=1,NPTS
0035          YFIT(I)=FUNCTN(X,I,A,T)
0036        2 CONTINUE
0037          R=FCHISQ(5)
0038          WRITE (9,600) (I,I=1,NTERMS),NTERMS+1
0039    600   FORMAT (///,1X,7H CHISQR,2X,10(5X,2H A,I1,4X))
0040          WRITE (9,700) R,(A(J),J=1,NTERMS),B1
0041    700   FORMAT (//,11(E10.4,2X))
0042        3 FLAMDA=0.001
0043          CALL CURFIT
0044          WRITE (9,700) CHISQR,(A(J),J=1,NTERMS)
0045          WRITE (9,800) (SIGMAA(J),J=1,NTERMS)
0046    800   FORMAT (12X,10(E10.4,2X))
0047          DO 10 K=1,NTERMS
0048    10    IF (A(K).LE.DELTAA(K)) DELTAA(K)=DELTAA(K)/10.00
0050          IF ((R-CHISQR)/CHISQR)-1.E-3) 5,5,4
0051        4 R=CHISQR
0052          GO TO 3
0053        5 CONTINUE
0054          WRITE(9,850) T
FORTRAN IVV01C-03A
```

```
0055   850  FORMAT(/,16H TEMPERATURE(K)=,F5.1)
0056        WRITE(9,901) (X(I),Y(I),YFIT(I),I=1,NPTS)
0057   901  FORMAT(//,50(E10.4,3X,E10.4,3X,E10.4,/))
0058        END
```

FORTRAN IVV01C-03A

```
0001        FUNCTION FUNCTN(Q,L,V,E)
0002        IMPLICIT DOUBLE PRECISION (A-H,O-Z)
0003        DIMENSION Q(100),V(10)
0004        X1=Q(L)
0005        Z=4*V(1)*(V(2)*X1)*(5.5)
0006        IF (Z.LE.0) Z=0.
0008        Z=DSQRT((V(1)+V(2)*X1)**2+Z)
0009        FUNCTN=(-V(1)-V(2)*X1+Z)/(2*(5.5))
0010        RETURN
0011        END
```

```
FORTRAN IVV01C-03A                                    PAGE 001

      C     DOCUMENTATION ON PAGE 237 , BEVINGTON:DATA REDUCTION AND ERROR
      C     ANALYSIS FOR THE PHYSICAL SCIENCES
0001        SUBROUTINE CURFIT
0002        IMPLICIT DOUBLE PRECISION (A-H,O-Z)
0003        COMMON SIGMAA(10),CHISQR,FLAMDA
0004        COMMON/DIFF/ A(10),DELTAA(10),X(100),DERIV(10),I,NTERMS
0005        COMMON/CHI/ Y(100),SIGMAY(100),YFIT(100),NPTS,NFREE,
           CMODE,WEIGHT(100)
0006        COMMON/MATRIX/ARRAY(10,10)
0007        DIMENSION ALPHA(10,10),BETA(10),B(10)
0008  11    NFREE = NPTS - NTERMS
0009        IF (NFREE) 13,13,20
0010  13    CHISQR=0.
0011        GO TO 110
      C     EVALUATE WEIGHTS
0012  20    DO 30 I=1,NPTS
0013  21    IF (MODE) 22,27,29
0014  22    IF (Y(I)) 25,27,23
0015  23    WEIGHT(I)= 1./Y(I)
0016        GO TO 30
0017  25    WEIGHT(I) = 1. / (-Y(I))
0018        GO TO 30
0019  27    WEIGHT(I)=1.
0020        GO TO 30
0021  29    WEIGHT(I)=1./SIGMAY(I)**2
  22  30    CONTINUE
  23   61   DO 62 I=1,NPTS
0024        YFIT(I)=FUNCTN(X,I,A,T)
0025   62   CONTINUE
      C     EVALUATE ALPHA AND BETA MATRICES
0026  31    DO 34 J=1, NTERMS
0027        BETA(J)=0.
0028        DO 34 K=1,J
0029  34    ALPHA(J,K)=0.
0030  41    DO 50 I=1, NPTS
0031        CALL FDERIV(I)
0032        DO 46 J=1,NTERMS
0033        BETA(J)=BETA(J)+(WEIGHT(I)*(Y(I)-YFIT(I)))*DERIV(J)
0034        DO 46 K=1,J
0035  46    ALPHA(J,K)=ALPHA(J,K)+(WEIGHT(I)*DERIV(J)*DERIV(K)
0036  50    CONTINUE
0037  51    DO 53 J=1,NTERMS
0038        DO 53 K=1,J
0039  53    ALPHA(K,J)= ALPHA(J,K)
      C     EVALUATE CHI SQUARE AT STARTING POINT
0040  63    CHISQ1 = FCHISQ(S)
      C     INVERT MODIFIED CURVATURE MATRIX TO FIND NEW PARAMETERS
0041  71    DO 74 J=1, NTERMS
0042        DO 73 K=1, NTERMS
0043  73    ARRAY(J,K) = ALPHA(J,K)/DSQRT(ALPHA(J,J))/DSQRT(ALPHA(K,K))
0044  74    ARRAY(J,J)= 1.+ FLAMDA
   5  80    CALL MATINV(NTERMS,DET)
0046  81    DO 84 J=1, NTERMS
0047        B(J)= A(J)
FORTRAN IVV01C-03A
```

PAGE 002

```
0048          DO 84 K=1, NTERMS
0049          BJ=(BETA(K)/DSQRT(ALPHA(J,J)))*(ARRAY(J,K)/DSQRT(ALPHA(K,K)))
0050    84    B(J)=B(J)+BJ
      C       IF CHI SQUARE INCREASED, INCREASE FLAMDA AND TRY AGAIN
0051  91      DO 92 I=1, NPTS
0052          YFIT(I)=FUNCTN(X,I,B,T)
0053    92    CONTINUE
0054  93      CHISQR=FCHISQ(S)
0055          IF (CHISQ1-CHISQR) 95,101,101
0056  95      FLAMDA= 10.* FLAMDA
0057          GO TO 71
      C       EVALUATE PARAMETERS AND UNCERTAINTIES
0058  101     DO 103 J=1, NTERMS
0059          A(J)=B(J)
0060          SIGMAA(J)=DSQRT(DABS(ARRAY(J,J)/ALPHA(J,J)))
0061    103   CONTINUE
0062          FLAMDA= FLAMDA/10.
0063  110     RETURN
0064          END
```

FORTRAN IVV01C-03A PAGE 001

```
      C       DOCUMENTATION ON PAGE 194 OF BEVINGTON:"DATA REDUCTION AND ERROR
      C       ANALYSIS FOR THE PHYSICAL SCIENCES
0001          FUNCTION FCHISQ(S)
0002          IMPLICIT DOUBLE PRECISION (A-H,O-Z)
0003          COMMON/CHI/ Y(100),SIGMAY(100),YFIT(100),NPTS,NFREE,
             CMODE,WEIGHT(100)
0004    11    CHISQ = 0.D0
0005    12    IF (NFREE) 13,13,20
0006    13    FCHISQ=0.
0007          GO TO 40
      C
      C       ACCUMULATE CHI SQUARE
0008    20    DO 30 I=1,NPTS
0009    30    CHISQ = CHISQ + WEIGHT(I)*((Y(I)-YFIT(I)))**2
      C       DIVIDE BY THE NUMBER OF DEGREES OF FREEDOM
0010    31    FREE= NFREE
0011    32    FCHISQ  = CHISQ /FREE
0012    40    RETURN
0013          END
```

```
   TRAN 1VV01C-03A                                          PAGE 001

     C       SUBROUTINE FDERIV (NON ANALYTICAL)
0001         SUBROUTINE FDERIV(I)
0002         IMPLICIT DOUBLE PRECISION (A-H,O-Z)
0003         COMMON/DIFF/A(10),DELTAA(10),X(100),DERIV(10),T,NTERMS
0004     11  DO 18 J=1,NTERMS
0005         AJ=A(J)
0006         DELTA=DELTAA(J)
0007         A(J)=AJ+DELTA
0008         YFIT1=FUNCTN(X, 1, A, T)
0009         A (J)=AJ-DELTA
0010         DERIV(J)= (YFIT1-FUNCTN(X,I,A,T))/(2.*DELTA)
0011     18  A(J)=AJ
0012         RETURN
0013         END
```

```
FORTRAN IVV01C-03A                                    PAGE 001

      C     SUBROUTINE MATINV
      C
      C     PURPOSE: INVERT A SYMMETRIC MATRIX AND CALCULATE ITS DETERMINANT
      C     USAGE  : CALL MATINV( NORDER, DET)
      C     DESCRIPTION OF PARAMETERS:
      C     ARRAY - INPUT MATRIX WHICH IS REPLACED BY ITS INVERSE
      C     NORDER - DEGREE OF MATRIX
      C     DET  - DETERMINANT OF INPUT MATRIX
      C     NO SUBROUTINES OR FUNCTIONS REQUIRED
      C     DIMENSION STATEMENT VALID FOR NORDER UP TO 10
      C
0001        SUBROUTINE MATINV(NORDER, DET)
0002        IMPLICIT DOUBLE PRECISION (A-H,O-Z)
0003        COMMON/MATRIX/ARRAY(10,10)
0004        DIMENSION  IK(10), JK(10)
0005  10    DET=1.
0006  11    DO 100 K=1, NORDER
      C     FIND LARGEST ELEMENT ARRAY(I,J) IN MATRIX
0007        AMAX=0.
0008  21    DO 30 I=K, NORDER
0009        DO 30 J=K, NORDER
0010  23    IF(DABS(AMAX) - DABS(ARRAY(I,J))) 24, 24, 30
0011  24    AMAX=ARRAY(I,J)
0012        IK(K)=I
0013        JK(K)=J
0014  30    CONTINUE
      C     INTERCHANGE ROWS AND COLUMNS TO PUT AMAX IN ARRAY(K,K)
0015  31    IF (AMAX) 41, 32, 41
0016  32    DET=0.
0017        GO TO 140
0018  41    I=IK(K)
0019        IF (I-K) 21, 51, 43
0020  43    DO 50 J=1, NORDER
0021        SAVE=ARRAY(K,J)
0022        ARRAY(K,J)=ARRAY(I,J)
0023  50    ARRAY(I,J)=-SAVE
0024  51    J =JK(K)
0025        IF (J-K) 21, 61, 53
0026  53    DO 60 I=1, NORDER
0027        SAVE=ARRAY(I,K)
0028        ARRAY(I,K) = ARRAY(I,J)
0029  60    ARRAY(I,J) = -SAVE
      C
      C     ACCUMULATE ELEMENTS OF INVERSE MATRIX
0030  61    DO 70 I=1, NORDER
0031        IF (I-K) 63, 70, 63
0032  63    ARRAY(I,K) = -ARRAY(I,K)/AMAX
0033  70    CONTINUE
0034  71    DO 80 I=1, NORDER
0035        DO 80 J=I, NORDER
0036        IF (I-K) 74, 80, 74
0037  74    IF (J-K) 75, 80, 75
0038  75    ARRAY(I,J)=ARRAY(I,J)+ ARRAY(I,K)*ARRAY(K,J)
0039  80    CONTINUE
FORTRAN IVV01C-03A
```

```
0040   81     DO 90 J=1, NORDER
   1          IF (J-K) 83, 90, 83
0042   83     ARRAY(K,J) = ARRAY(K,J) /AMAX
0043   90     CONTINUE
0044          ARRAY(K,K) = 1.DO /AMAX
0045   100    DET = DET* (AMAX)
       C
       C      RESTORE ORDERING OF MATRIX
0046   101    DO 130 L=1, NORDER
0047          K=NORDER-L+1
0048          J=IK(K)
0049          IF (J-K) 111, 111, 105
0050   105    DO 110 I=1, NORDER
0051          SAVE = ARRAY(I,K)
0052          ARRAY(I,K)= -ARRAY(I,J)
0053   110    ARRAY(I,J) =SAVE
0054   111    I= JK(K)
0055          IF (I-K) 130, 130, 113
0056   113    DO 120 J=1, NORDER
0057          SAVE=ARRAY(K,J)
0058          ARRAY(I,J) = -ARRAY(I,J)
0059   120    ARRAY(I,J) = SAVE
0060   130    CONTINUE
0061   140    RETURN
0062          END
```

APPENDIX B: COMPLETE REACTION SET FOR PHOTOCHEMICAL MODELING

The following is a list of chemical reactions and rate constants used in modeling the photochemistry experiments. The units of the rate constants are $(cm^3/molecule)^x \cdot sec^{-1}$; where x = 0 for unimolecular reactions, x = 1 for bimolecular reactions and x = 2 for termolecular reaction. Activation energies are in K.

				$\sigma_{eff}(cm^2)$	ϕ
1.	$N_2O_5 + h\nu$	=	Products	2.8E-19	
2.	$N_2O_4 + h\nu$	=	$NO_2 + NO_2$	8.0E-19	0.2
3.	$NO_2 + h\nu$	=	$NO + O$	3.0E-20	1.0
4.	$O_3 + h\nu$	=	$O_2 + O$	2.0E-17	1.0
5.	$HNO_3 + h\nu$	=	$HO + NO_2$	1.94E-20	1.0
6.	$NO_3 + h\nu$	=	$NO_2 + O$	1.0E-20	1.0
				A	E_a
7.	$NO_2 + NO_3 + M$	=	$N_2O_5 + M$		
8.	$N_2O_5 + M$	=	$NO_2 + NO_3 + M$		
9.	$NO_2 + NO_2 + M$	=	$N_2O_4 + M$	4.70E-35	-860
10.	$N_2O_4 + M$	=	$NO_2 + NO_2 + M$	4.20E-7	5550
11.	$NO + NO_3$	=	$NO_2 + NO_2$	1.87E-11	---
12.	$NO_2 + NO_3$	=	$NO_2 + NO + O_2$	2.50E-14	1230
13.	$NO_3 + NO_3$	=	$NO_2 + NO_2 + O_2$	8.50E-13	2450
14.	$O + O_2 + M$	=	$O_3 + M$	1.10E-34	-510
15.	$O + NO_2 + M$	=	$NO_3 + M$	1.0E-31	---
16.	$O + NO_2$	=	$NO + O_2$	9.1E-12	---
17.	$O + NO_3$	=	$NO_2 + O_2$	1.0E-11	---
18.	$O_3 + NO$	=	$O_2 + NO_2$	9.0E-13	1200
19.	$O_3 + NO_2$	=	$O_2 + NO_3$	1.34E-13	2466
20.	$O_3 + O$	=	$O_2 + O_2$	1.90E-11	2300
21.	$HO + HNO_3$	=	$H_2O + NO_3$	1.30E-13	---
22.	$HO + NO_2 + M$	=	$HNO_3 + M$	3.6E-32	-1100
23.	$HO + O_3$	=	$HO_2 + O_2$	1.6E-12	1000

ACKNOWLEDGMENTS

I would like to take this opportunity to thank the many individuals who supported me in the course of this research. The guidance of Professor Harold S. Johnston supplied direction and impetus throughout this work. His wide-ranging interests provided me exposure to many aspects of atmospheric chemistry.

The assistance, encouragement and stimulating interaction with my classmate, John Girman, coworkers Richard Graham, and David Littlejohn and postdoctoral scientist Gary Whitten contributed greatly to the successful conclusion of this research. Additionally the supportive atmosphere provided by the research group is appreciated.

Gratitude is also due to the personnel of the Department of Chemistry and of Lawrence Berkeley Laboratory for excellent support and assistance.

I wish also to thank the U. S. Department of Energy for their funding of this research through the Materials and Molecular Research Division of Lawrence Berkeley Laboratory.

BIBLIOGRAPHY

1. P. A. Leighton, Photochemistry of Air Pollution, (Academic Press, NY, 1961), pp. 26-71.
2. H. S. Johnston, Science 173, 517 (1971).
3. F. Daniels and E. H. Johnston, J. Am. Chem. Soc. 43, 53 (1921).
4. W. F. Busse and F. Daniels, J. Am. Chem. Soc. 49, 1257 (1927).
5. J. H. Smith and F. Daniels, J. Am. Chem. Soc. 69, 1735 (1947).
6. R. L. Mills and H. S. Johnston, J. Am. Chem. Soc. 73, 938 (1951).
7. H. S. Johnston and R. L. Perrine, J. Am. Chec. 73, 4782 (1951).
8. H. S. Johnston, J. Am. Chem. Soc. 75, 1567 (1953).
9. D. J. Wilson and H. S. Johnston, J. Am. Chem. Soc. 75, 5763 (1953).
10. I. C. Hisatsune, B. Crawford and R. A. Ogg, Jr., J. Am. Chem. Soc. 79, 4648 (1957).
11. A. A. Viggiano, J. A. Davidson, D. L. Albritton, F. C. Fehsenfeld* and E. E. Ferguson, submitted to J. Chem. Phys. and *private communication (1979).
12. J. F. Noxon, R. B. Norton and W. R. Henderson, Geophys. Res. Lett. 5, 675 (1978).
13. H. S. Johnston and J. R. White, J. Chem. Phys. 22, 1969 (1954).
14. H. H. Holmes and F. Daniels, J. Am. Chem. Soc. 56, 630 (1934).
15. R. Murphy, Doctoral Thesis, University of California at Los Angeles, (University Microfilms, Ann Arbor, 1969).
16. L. R. Maxwell, V. M. Mosley and L. S. Demig, J. Chem. Phys. 2, 331 (1934).

17. G. L. Lewis and C. P. Smyth, J. Am. Chem. Soc. 61, 3067 (1939).

18. V. K. Kelkar, K. C. Bhalla and P. G. Khubchandani, J. Mol. Struc. 9, 383 (1971).

19. P. A. Akishin, L. V. Vilkov, E. Z. Zasorin, N. G. Rambini and V. P. Spiridonov, J. Phys. Soc. Japan 17, 18 (1961).

20. I. C. Hisatsune, J. Phys. Chem. 65, 2249 (1961).

21. I. C. Hisatsune, J. P. Devlin and Y. Wada, Spec. Acta 18, 1641 (1962).

22. R. A. Ogg, Jr., J. Chem. Phys. 15, 337 (1947).

23. E. D. Morris, Jr. and H. Niki, J. Phys. Chem. 77, 613 (1947).

24. G. E. Streit, J. S. Wells, F. C. Fehsenfeld and Carleton J. Howard, J. Chem. Phys. 70, 3439 (1979).

25. I. R. McKinnon, J. G. Mathieson and I. R. Wilson, J. Phys. Chem. 83, 779 (1979).

26. J. H. Hodges and E. F. Linhorst, Proc. Mat. Acad. Sci. 17, 28 (1931).

27. R. A. Graham and H. S. Johnston, J. Phys. Chem. 82, 254 (1978).

28. E. W. Kaiser and S. M. Japar, Chem. Phys. Lett. 54, 265 (1978).

29. T. T. Paukert, Doctoral Thesis, University of California at Berkeley, (November, 1969) UCRL-19109.

30. G. Z. Whitten, Rate Constant Evaluation Using a New Computer Modeling Scheme, presented at the ACS National Meeting, (Spring, 1974).

31. G. Z. Whitten and J. P. Meyer, CHEMK: A Computer Modeling Scheme for Chemical Kinetics, (Systems Applications, Inc., 1979).

32. R. F. Hampson, Jr. and D. Garvin, Reaction Rate and Photo-Chemical Data for Atmospheric Chemistry-1977, (NBS, U. S. Department of Commerce, May, 1978).

33. F. Magnotta, private communication.

34. G. Schott and N. Davidson, J. Am. Chem. Soc. 80, 1841 (1958).

35. F. H. Verhoek and F. Daniels, J. Am. Chem. Soc. 53, 1250 (1931).

36. A. B. Harker, Doctoral Thesis, University of California at Berkeley, (September, 1972) LBL-1114.

37. R. A. Graham, Doctoral Thesis, University of California at Berkeley, (November, 1975) LBL-4147.

38. E. Vassy, Ann. de Phys. 8, 679 I1937).

39. A. B. Harker and H. S. Johnston, J. Phys. Chem. 77, 1153 (1973).

40. R. B. Holt, C. K. McLane and O. Oldenburg, J. Chem. Phys. 16, 225, 638 (1948).

41. L. T. Molina, S. D. Schinke and M. J. Molina, Geophys. Res. Lett. 4, 580 (1977).

42. C. L. Lin, N. K. Rohatgi and W. B. DeMore, Geophys. Res. Lett. 5, 113 (1978).

43. REFERENCE DELETED.

44. F. A. Lindemann, Trans. Far. Soc. 17, 598 (1922).

45. C. N. Hinshelwood, The Kinetics of Chemical Change, (Oxford Univ. Press, Oxford, 1940).

46. H. S. Johnston, Gas Phase Reaction Rate Theory, (Ronald Press Co., NY, 1966) pp. 268-269.

47. H. S. Johnston, private communication.

48. P. J. Robinson and K. A. Holbrook, Unimolecular Reactions, (Wiley-Interscience, London, 1972) pp. 53-55.

49. H. S. Johnston, J. Chem. Phys. 20, 1103 (1952).

50. L. Kassel, J. Chem. Phys. 21, 1093 (1953).

51. E. Thiele and D. J. Wilson, J. Chem. Phys. 35, 1256 (1961).

52. R. A. Marcus, J. Chem. Phys. 20, 359 (1952).

53. G. M. Wieder and R. A. Marcus, J. Chem. Phys. 37, 1835 (1962).

54. S. W. Benson and D. M. Golden, Physical Chemistry: An Advanced Treatise Vol. 7, (Academic Press, NY, 1975).

55. G. P. Smith and D. M. Golden, Int. J. Chem. Kin. X, 489 (1978).

56. A. C. Baldwin and D. M. Golden, J. Phys. Chem. 82, 644 (1978).

57. A. C. Baldwin and D. M. Golden, private communication.

58. F. W. Schnieder and B. S. Rabinovitch, J. Am. Chem. Soc. 84, 4215 (1962).

59. R. E. Weston, Jr. and H. A. Schwartz, Chemical Kinetics (Prentice-Hall, NJ, 1972) p. 132.

60. R. A. Graham, A. M. Winer and J. N. Pitts, Jr., J. Chem. Phys. 68, 4505 (1978).

61. H. C. Urey, L. H. Dawsey and F. O. Rice, J. Am. Chem. Soc. 51, 3190 (1929).

62. E. J. Jones and O. R. Wulf, J. Chem. Phys. 5, 873 (1937).

63. R. L. Daubendiek and J. G. Calvert, Env. Lett. 8, 103 (1975).

64. I. Wilson, private communication.

65. W. G. Fately, H. A. Bent and B. Crawford, Jr., J. Chem. Phys. 31, 204 (1959).

66. P. King, I. R. McKinnon, J. G. Mathieson and I. R. Wilson, J. Atmos. Sci. 33, 1657 (1976).

67. B. A. Ridley, M. McFarland, J. T. Bruin, H. I. Schiff and J. C. McConnell, Can. J. Phys. 55, 212 (1977).

68. Evans, et al. Paper presented at World Meteorological Organization Meeting, Toronto, 1978.

69. J. F. Noxon, private communication.

TECHNICAL INFORMATION DEPARTMENT
LAWRENCE BERKELEY LABORATORY
UNIVERSITY OF CALIFORNIA
BERKELEY, CALIFORNIA 94720